Dynamics of fine structure in the atmosphere of solar active regions

by

Gregal Joan Maria Vissers

THESIS
for the degree of
PHILOSOPHIÆ DOCTOR

Institute of Theoretical Astrophysics
Faculty of Mathematics and Natural Sciences
University of Oslo

May 2013

Series of dissertations submitted to the
Faculty of Mathematics and Natural Sciences, University of Oslo
No. 1373

ISSN 1501-7710

Cover: Inger Sandved Anfinsen.
Printed in Norway: AIT Oslo AS.

Produced in co-operation with Akademika Publishing.
The thesis is produced by Akademika Publishing merely in connection with the thesis defence. Kindly direct all inquiries regarding the thesis to the copyright holder or the unit which grants the doctorate.

The beginning of knowledge is the discovery of something we do not understand.
— Frank Herbert

Abstract

This thesis presents an observational study of the dynamics of fine structure in the (mostly lower) atmosphere of solar active regions. The considered phenomena – Ellerman bombs, flocculent flows and coronal rain – are diverse, but ubiquitous in active regions and are testament to the need for high-resolution observations of the solar atmosphere. Employing data obtained with the CRisp Imaging SpectroPolarimeter (CRISP) at the Swedish 1-m Solar Telescope (SST), they are studied at a higher spatial, spectral and temporal resolution than ever before.

Multi-diagnostic analysis of Ellerman bombs provides evidence, both through their flame-like morphology in Hα 6563 Å and Ca II 8542 Å, and from underlying Fe I 6301 Å polarimetry, that they constitute a photospheric reconnection phenomenon between small-scale, but strong magnetic concentrations. Their fine structure displays dynamic changes on the timescale of seconds, enhancing their flaring character as they move along intergranular lanes. Simultaneous short-wavelength data from the Atmospheric Imaging Assembly on the Solar Dynamics Observatory reveal no consistent upper atmosphere response, but suggest that Ellerman bomb detection in 1700 Å may prove feasible in identifying small-scale reconnection in larger active regions and possibly even full-disc images.

High-cadence Hα CRISP data have also enabled the discovery of small elongated absorptions that propagate along curved trajectories, following the canopy of superpenumbral fibrils surrounding a small sunspot, in a seemingly footpoint-to-footpoint motion. Based on their morphology, dynamics and recurrence along similar paths, we have dubbed them "flocculent flows". Both their quantitative dynamics and their Doppler signature seem to argue for actual mass motion, rather than propagating waves, while their size is comparable to, but smaller than the morphologically similar coronal rain. We suggest they may be part of a siphon flow, where the condensations result from either recurring heating events or a thermal instability aggravated by wave interactions with the flow channels.

Finally, a study of coronal rain in Hα data aims at expanding the statistics on this phenomenon to cases that are only observed on-disc, at different viewing angles. Their on-disc characterisation is much more difficult and may partly explain the tendency we find for the condensations to move slower, be more elongated and colder than their off-limb counterparts. Nevertheless, their properties generally agree well with earlier studies, while being sufficiently different from those of flocculent flows for these morphologically similar phenomena to be distinguished.

Contents

Part I

Introduction

1

INTRODUCTION

It is difficult not to get captivated by impressive solar imagery such as in Fig. 1.1 or 1.2, in particular when one adds time evolution to the picture. Imaging the Sun at about 600.000 K, Fig. 1.2 highlights some of the large-scale but complex structures of the Sun's outermost atmosphere. By using different wavelength filters one can observe structures and dynamics that are at different temperatures. Given that the solar atmosphere has a pronounced temperature gradient, this generally translates into observing different "layers" of the solar atmosphere. From the solar surface outwards these are called the *photosphere*, the *chromosphere*, the *transition region* and the *corona*. The structuring into several layers with differing properties is reminiscent of the Earth's atmosphere, an analogy that works best in the lower solar atmosphere where gravity manages to stratify the atmosphere in close to plane-parallel layers. In the higher atmosphere this starts breaking down, as the density decreases drastically outwards and structuring by the magnetic field

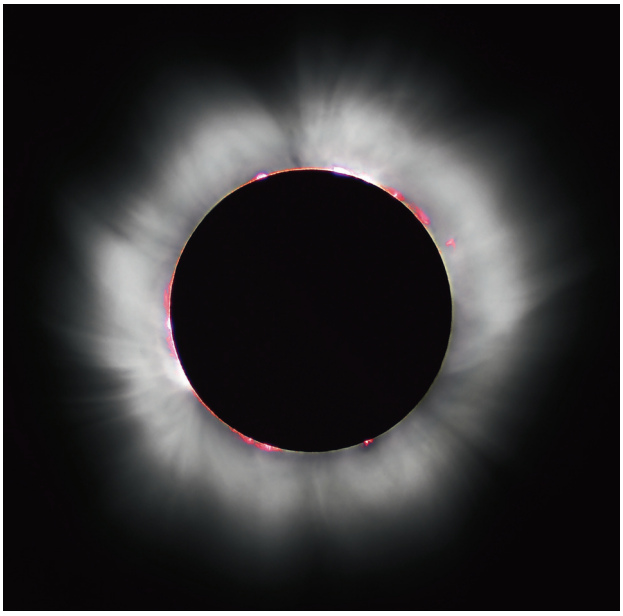

Figure 1.1 Solar eclipse of August 11, 1999 observed from northern France. The typical purple-reddish colour of the chromosphere stands out clearly against the backdrop of the ghostly white corona. Picture taken by and reproduced by permission of Luc Viatour/www.Lucnix.be.

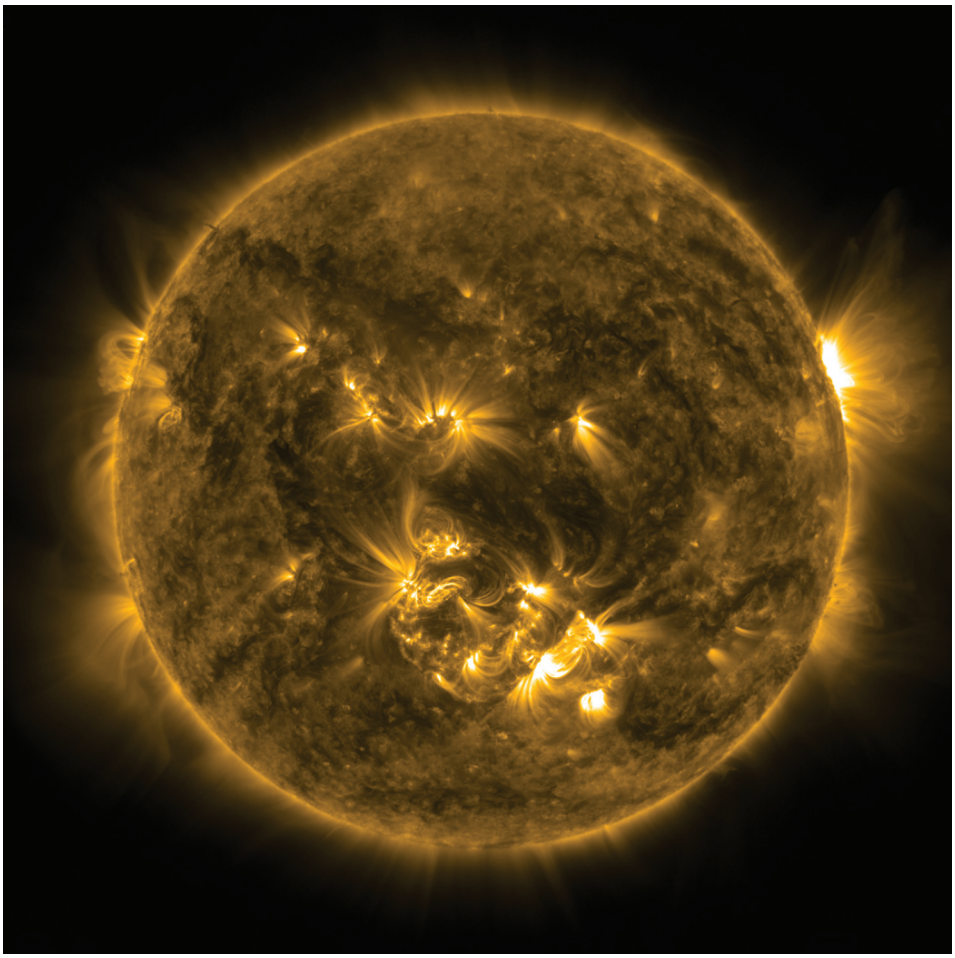

Figure 1.2 False colour full-disc image of the Sun as observed in the Fe IX 171 Å line (commonly used as diagnostic for plasma at a temperature of about 600.000 K) with the Atmospheric Imaging Assembly on board the Solar Dynamics Observatory on June 13, 2012. The image has been retrieved using JHelioviewer (Müller et al. 2009).

takes over.

The lowest layer, the photosphere, is the region from which the bulk of the light escapes in the visible part of the spectrum. It is a layer of about 500 km thick and an effective temperature of 5777 K, although temperatures range between 4500-6000 K. With an average density of 10^{-6}–10^{-7} g cm^{-3} its structures are generally gas-dominated (with the exception of sunspots and pores). The chromosphere above owes its name to the purple-red colour of this atmospheric layer during a total solar eclipse (see Fig. 1.1 for a recent example). It is a region where the temperature on average increases from the photospheric decline to a plateau at some 6000–7000 K. Simultaneously, the density decreases by several orders of magnitude from 10^{-7} g cm^{-3} to 10^{-14} g cm^{-3}, making it a transition

layer from the gas-dominated atmosphere below to the magnetic field dominated corona above.

The transition region and corona together make up the outer solar atmosphere. From the chromosphere upwards the temperature experiences a sharp increase over the course of only a few thousand kilometres. The *transition region* owes its name to representing that transition; it does not correspond to a layer at a particular altitude as the structures in the upper chromosphere and above are shaped primarily by the magnetic field and the dynamics of the gas, rather than by gravity. The corona is the hot (a few 10^6 K) and tenuous ($\sim 10^{-15}$ g cm^{-3}) most outer part of the solar atmosphere that has been named such because of its crown-like appearance during eclipses (cf. Fig. 1.1).

Although being a rather unremarkable star within our galaxy with respect to its general properties, its close proximity makes it invaluable for astrophysical research. Indeed, it constitutes an astrophysical laboratory, enabling the refinement of stellar evolution and atmosphere models, understanding of spectral line formation, and testing of magneto-hydrodynamic models. Over the past decade tremendous advances have been made in instrumentation that allow us nowadays to observe the Sun at an ever improving resolution, both spatially, spectrally and temporally. The wealth of information that can be extracted from these high-resolution observations has particularly increased since the inauguration of the renewed Swedish 1-m Solar Telescope (SST; Scharmer et al. 2003a) in 2001, first light for the Interferometric BIdimensional Spectrometer (IBIS; Cavallini 2006) at the Dunn Solar Telescope (DST) in 2003, the launch in 2006 of the JAXA/NASA solar space observatory *Hinode* (Kosugi et al. 2007), the installation of the CRisp Imaging SpectroPolarimeter (CRISP; Scharmer et al. 2008) at the SST in 2008 and the launch in 2010 of the Solar Dynamics Observatory (SDO) with its Atmospheric Imaging Assembly (AIA; Lemen et al. 2012). Although the latter has a coarser spatial resolution than either the SST, DST or *Hinode*, it boasts continuous full-disc coverage at short wavelengths (imaging the transition region and corona) with a cadence of one image every 12–24 s, depending on the wavelength.

In the remainder of this chapter, a more detailed description of the CRisp Imaging SpectroPolarimeter (which is the main instrument used for this thesis) is given first, in Section 1.1, before embarking on an observationally driven tour in Section 1.2 of (mostly) fine structure dynamics of the magnetised solar atmosphere. Section 1.3 is an extension of the appendix to Vissers et al. (2012, **Paper III**) and offers an up-to-date description of a data browsing and analysis tool, the CRIsp SPectral EXplorer (CRISPEX), that was developed in parallel to and used in all the research described in this thesis. Chapter 2 summarises the work on which this thesis is based, giving a short overview over the contents of four papers. Finally, Part II collects those papers in full.

1.1 The CRisp Imaging SpectroPolarimeter

In astrophysics, both ground-based and space-based telescopes are used to obtain observational data. As with all, the choice for one or the other is a trade-off between advantages and disadvantages, in this case in terms of, e.g., intrinsic data quality, accessibility, costs and telescope size. Space-based telescopes have the clear advantage of providing a view on the Universe that is unperturbed by the Earth's atmosphere, but their aperture and overall size are limited by the payload constraints of the rocket that carries the satellite into orbit. They are also generally much more expensive than ground-based telescope facilities and are typically more constrained in their data acquisition rate because of limited telemetry. Ground-based telescopes, on the other hand, are limited in size only by the available funding (apart from obvious location constraints) and are easier to upgrade, but they have to cope with a variable atmosphere degrading the data quality.

The atmosphere is far from uniform and the disturbing effects are more pronounced for day-time astronomy than they are for night-time observers, although the principle is the same. Local differences in atmospheric temperature translate into a locally different refractive index of the air. In turn, this results in the light path of adjacent rays not being the same and initially parallel wave-fronts end up being perturbed. The effect on the observations is visible as e.g., blurring, deformation and translation of the images and these effects are collectively referred to as *seeing*. Fortunately, existing in-situ mechanical solutions (i.e., so-called *adaptive optics*) and image post-processing software techniques allow minimisation of these degrading atmospheric effects.

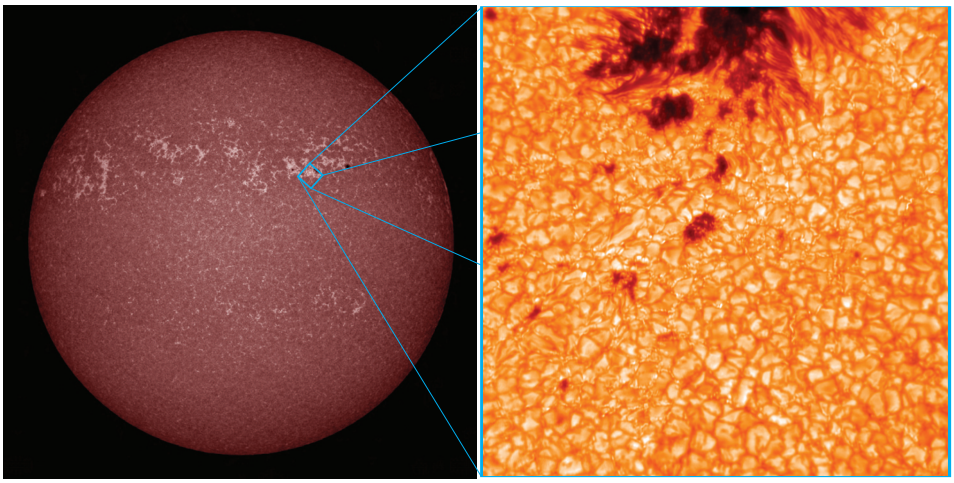

Figure 1.3 Field-of-view size comparison between SDO and SST. *Left*: Full-disc image of the Sun as seen in the UV-continuum at 1700 Å by SDO/AIA. *Right*: Continuum near Fe I 6302.5 Å as imaged by SST/CRISP. The SST field-of-view is marked by the blue box on the left-hand panel and covers about 51.″5 (37,000 km) squared. This CRISP data set and corresponding AIA sub-field-of-view data have been analysed in Vissers et al. (2013, **Paper II**).

The CRisp Imaging SpectroPolarimeter was installed in 2008 at the Swedish 1-m Solar Telescope located on the island of La Palma (Canary Islands, Spain), and is based on a dual Fabry-Pérot interferometer (FPI) system. CRISP observes in the red to near-infrared part of the spectrum and was originally designed for imaging spectropolarimetry, but has proven itself formidably in imaging spectroscopy as well, revealing much of the dynamical fine structure in the lower solar atmosphere that is discussed in Section 1.2.

The SST is a vacuum tower telescope equipped with a lens that has a clear aperture of slightly less than 1 m in diameter, making it the second largest refractor telescope in the world. Although the field-of-view of the SST is only "postage stamp"-sized in comparison to the full-disc images obtained with SDO (see Fig. 1.3), it offers the highest resolution imaging of the Sun from the ground to date, provided the weather conditions allow for good and stable seeing conditions. Regardless, corrections for atmospheric disturbances are necessary and applied both during the observations and in image post-processing. The former are achieved by means of a tip-tilt mirror and an adaptive-optics system (Scharmer et al. 2003b), driving actuators behind a deformable mirror at a frequency of 2 kHz to remove low-order seeing effects.

Remaining high-order distortions can be minimised during image post-processing. Several techniques exist, but Speckle interferometry (de Boer et al. 1992; von der Luehe 1993) and Multi-Frame Blind Deconvolution (MFBD; Schulz 1993; van Kampen & Paxman 1998; Löfdahl 2002) methods are most widely used in solar physics. Multi-Object Multi-Frame Blind Deconvolution (MOMFBD; van Noort et al. 2005), which is a extension of MFBD, is the technique currently employed for image post-processing of CRISP data. The "multi-object" part consists in using data of the same region as recorded through different filters for image restoration. For CRISP specifically, the wide-band data and the sequentially recorded narrow-band CRISP data act as multi-object images. Figure 1.4 shows the resulting image after applying respectively frame selection (i.e., selecting the best frame from a burst), MFBD (on the three best G-band exposures) and MOMFBD (on the full burst of 20 G-band and continuum exposures and including phase-diversity for both channels), and evidences the power of the latter. However, it should be noted that the difference in results

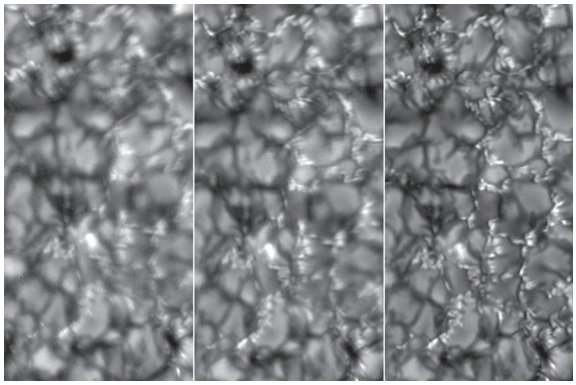

Figure 1.4 Application of different image post-processing techniques on an image obtained in the molecular G-band at the SST on May 9, 2004: frame selection (*left*), Multi-Frame Blind Deconvolution (*middle*) and Multi-Object Multi-Frame Blind Deconvolution (*right*). Image courtesy of Luc Rouppe van der Voort.

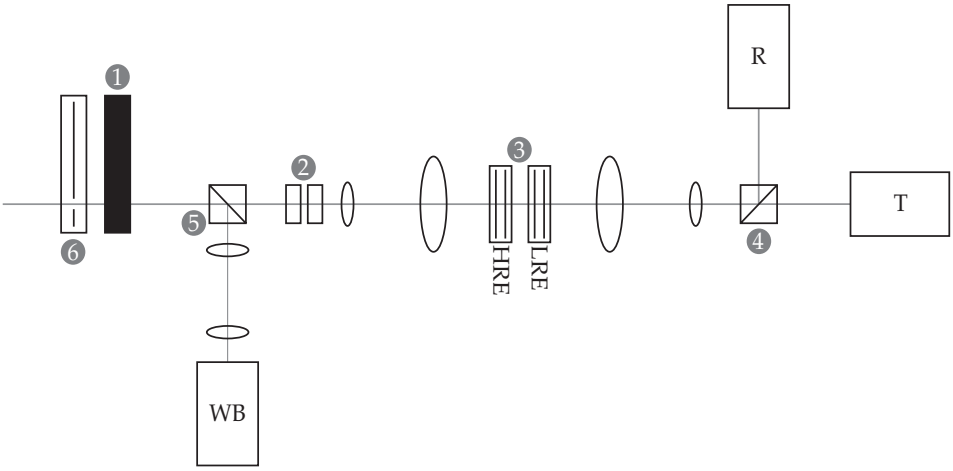

Figure 1.5 Schematic layout of the CRisp Imaging SpectroPolarimeter. The light path is indicated by the grey line and enters the setup from the left. Several optical elements are indicated: (1) a pre-filter wheel, (2) a set of liquid crystals, (3) a dual FPI with a high-resolution etalon (HRE) and a low-resolution etalon (LRE), (4) a polarising beam splitter, (5) a 10/90 beam splitter that branches off 10% of the light onto the wide-band camera, and (6) an optical chopper. The rectangular boxes represent the cameras: one wide-band camera (WB) and two narrow-band cameras, one imaging the transmitted beam (T) and one imaging the reflected beam (R).

between MFBD and MOMFBD becomes negligible when the number of exposures that are used in MFBD approaches those used in MOMFBD.

Figure 1.5 shows the schematic layout of CRISP's optical components: (1) a filter wheel with pre-filters for spectral passband selection (3–9 Å wide, depending on the central wavelength), (2) a set of liquid crystals that are modulated to obtain the four Stokes polarisation states (I, Q, U and V), (3) a tuneable dual FPI and (4) a polarising beam splitter that finally guides the light onto two orthogonally positioned cameras. An additional camera positioned after the filter wheel (but before the liquid crystals) provides wide-band imaging that is used during data post-processing, both as the multi-object channel for MOMFBD and as the alignment anchor for the exposures from the other two cameras. The light for this camera is branched off by a beam splitter (5) positioned between the pre-filter wheel and the liquid crystals. All three cameras are high-speed, low-noise Sarnov CAM1M100 CCD cameras with 1K×1K chips that run at a frame rate of 35 fps, with an exposure time of 17 ms. Synchronisation of the exposures is ensured by means of an optical chopper (6) placed in front of the filter wheel.

Selection of spectral passband is achieved by rotating the filter wheel, an adjustment that takes 250–600 ms depending on the filter wheel load and the filter positions between which it has to switch. The narrow-band wavelength selection is performed by the dual FPI. An FPI consists of two semi-reflective surfaces (together also referred to as an etalon) and employs constructive interference in order to select the desired wavelength. Only waves that fit an integer number

of wavelengths in the space between the surfaces are transmitted through the second semi-reflective surface (see e.g., Kitchin 2003). By tuning the distance between the surfaces, a different wavelength can be selected. In the case of CRISP, two etalons are used to obtain precise wavelength selection: a high spectral resolution, high reflectivity etalon (i.e., with a narrow transmission profile; HRE) and a low resolution, low reflectivity etalon (i.e., with a broader transmission profile; LRE). CRISP's dual FPI allows necessary etalon adjustments on a timescale of $\lesssim$50 ms.

Hence, combination of the SST and CRISP results in data with high spectral and temporal resolution, as well as high spatial resolution given the pixel scale of $0\farcs0592\,\mathrm{px}^{-1}$ ($0\farcs071\,\mathrm{px}^{-1}$ for data obtained prior to the 2009 observing season). The latter is well below the Rayleigh diffraction limit for all available pre-filters and allows observation of features as small as 100 km on the Sun during perfect seeing conditions.

1.2 Dynamics of the magnetised atmosphere

Solar observations throughout the centuries, but particularly in the last decades, have revealed a wide variety of dynamical features and phenomena present in the solar atmosphere. Necessarily, this section only covers a selection of those (mostly active region) dynamic phenomena and is meant to serve as background against which to consider the main topics of this thesis. Solar granulation and magnetic fields are discussed first, as they are at the core of much (if not all) of the dynamics that is covered in the rest of the thesis. Section 1.2.2 introduces sunspots and their dynamics in both the photosphere and chromosphere, including the inverse Evershed effect and chromospheric sunspot oscillations. Both are of relevance to *flocculent flows*, the topic of **Paper III**, as they share the superpenumbra as their occurrence location. Section 1.2.3 covers the spectral and morphological signature of *Ellerman bombs* and presents the current views on their driving mechanism and possible effects on the outer solar atmosphere; as such it provides the context for **Papers I** and **II**. Section 1.2.4 discusses dynamic fibrils and spicules, which are morphologically similar jet-like phenomena with different driving mechanisms. Similar to Ellerman bombs, spicules are likely caused by magnetic reconnection and both phenomena are (as all in **Papers I–IV**) testament to the need for high-resolution observations of the Sun. Finally, Section 1.2.5 concerns intermittent flows and waves, in particular blob-like chromosphere waves and so-called *coronal rain*. The latter provides the necessary context for **Paper IV**, while both are important when considering the morphologically similar flocculent flows discussed in **Paper III**.

Granulation

In order to set the stage for a discussion of the dynamics of the magnetised solar atmosphere, one must first consider the most predominant "feature" of the

photosphere: granulation. Its pattern of bright cells bounded by dark lanes could already be seen in Fig. 1.4, but is also clearly surrounding the sunspot in Fig. 1.6. The granulation pattern at the base of the photosphere is actually the top of the convection zone, showing overturning convection as hot plasma is pushed up by convective motions in the centre of granular cells and moves outwards before submerging again down the dark intergranular lanes. Quiet Sun granules typically last about 5–10 minutes and have sizes of approximately 1000 km (e.g., Bahng & Schwarzschild 1961; Bray et al. 1984; Spruit et al. 1990), while granules are smaller and longer-lived in more active regions. In turn, these granules are arranged in larger conglomerates – supergranules – that have average sizes between 10,000–30,000 km and lifetimes of up to a day (cf. Hart 1956, Leighton et al. 1962). The boundaries of supergranules typically coincide with so-called network in the photosphere (Muller 1983) and enhanced network (or plage) in the chromosphere (Leighton et al. 1962), consisting of smaller magnetic field concentrations that are called *magnetic bright points*.

Although not dominated by the magnetic field, the granular motions play an important role in sweeping emerging fields together into the aforementioned magnetic bright points and by causing braiding of the magnetic fields. These motions are also instrumental in generating waves that end up creating the irregular pattern of interfering wavefronts higher up in the lower chromosphere known as the *clapotisphere* (Rutten 1995) or *fluctosphere* (Wedemeyer-Böhm et al. 2009).

1.2.1 Magnetic fields

Magnetic fields and their reconfiguration are at the heart of much of the atmospheric features and dynamics both at large scales (e.g., sunspots, coronal loops, flares, coronal mass ejections) and small scales (e.g., pores, Ellerman bombs, jet-like phenomena, coronal rain). The Sun has an activity cycle that lasts roughly eleven years, coinciding with the reversal of its magnetic poles (i.e., one full reversal cycle lasting about 22 years, cf. Hale & Nicholson 1925). The magnetic fields are believed to originate in the *tachocline*, a term coined by Spiegel & Zahn (1992), in reference to the transition from the rigidly rotating radiative inner part to the differentially rotating convective outer part of the solar interior. The strong shear and turbulent convection at the tachocline are thought to play a vital role in the solar dynamo and the strengthening of magnetic fields (Ossendrijver 2003; Brandenburg & Subramanian 2005).

As shortly pointed out before, the distinction between the different atmospheric layers coincides also with a change in the interplay between the pressure from the magnetic field and the gas pressure. The photosphere is gas-dominated (except for sunspots and pores), while a transition between gas- and magnetic field domination is observed in the chromosphere. The structures in the corona, on the other hand, are dominated by the magnetic field. This change from gas to magnetic dominance can be described through the so-called plasma-β parameter

$$\beta = \frac{P_{\mathrm{g}}}{P_{\mathrm{B}}}, \tag{1.1}$$

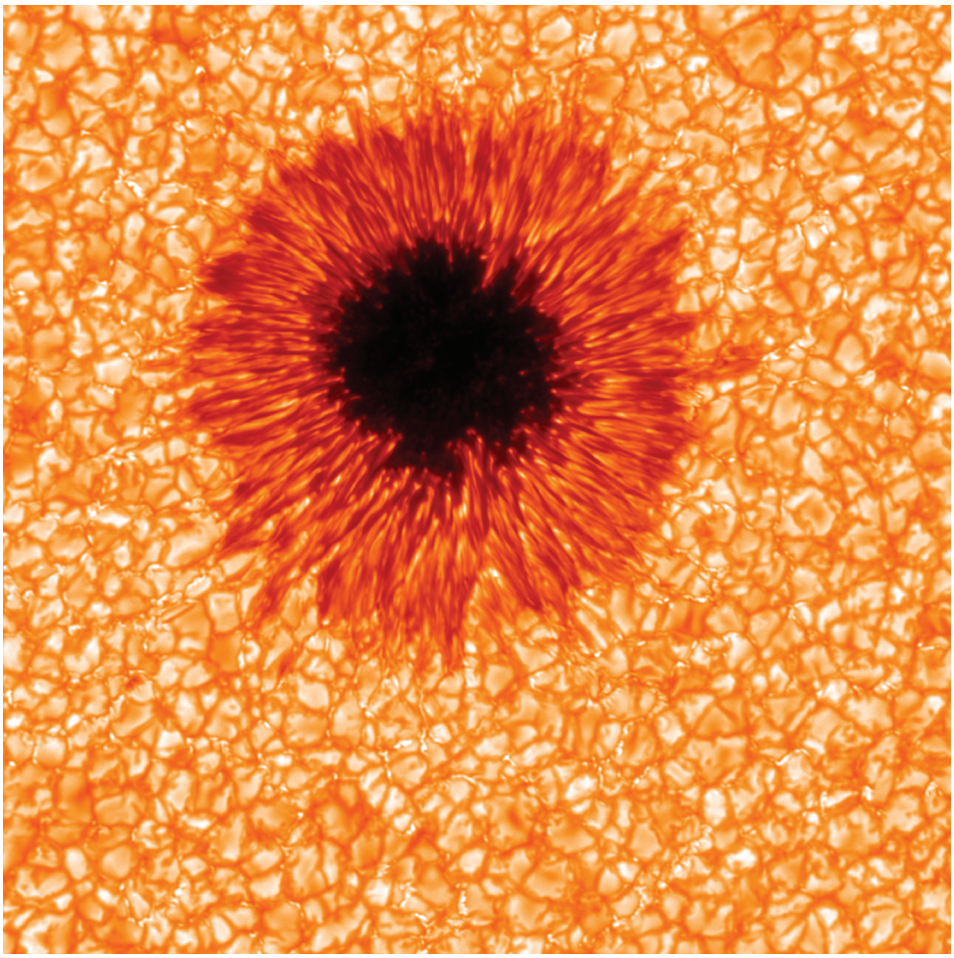

Figure 1.6 False colour wide band image sample in Fe I 6301 Å of a classical sunspot surrounded by granulation and some network (i.e., the bright points in the dark intergranular lanes). The displayed area is 57.″2 (corresponding to 41,500 km) squared and, with slightly over 9000 km, the diameter of the umbra is not much smaller than that of the Earth. The image was obtained on July 2, 2010 using SST/CRISP.

where P_g and $P_B = B^2/(2\mu_0)$ are the gas and magnetic pressure, respectively, with μ_0 the magnetic permeability in vacuum and B the magnetic field strength.

At the photospheric level ($\beta \gg 1$), the magnetic fields reveal themselves mainly as the earlier mentioned bright network and as sunspots and pores (see Fig. 1.4 and Fig. 1.6, respectively). The network in the quiet Sun consists of magnetic field concentrations of the order of 1–2 kG nested in intergranular lanes, to which they are advected by the (super)granular motions. They comprise single magnetic bright points, but also more complex structures such as "ribbons" or "flowers" (Berger et al. 2004; Rouppe van der Voort et al. 2005). Based on analytical work and numerical simulations (e.g., Spruit 1976; Spruit 1977; Carlsson

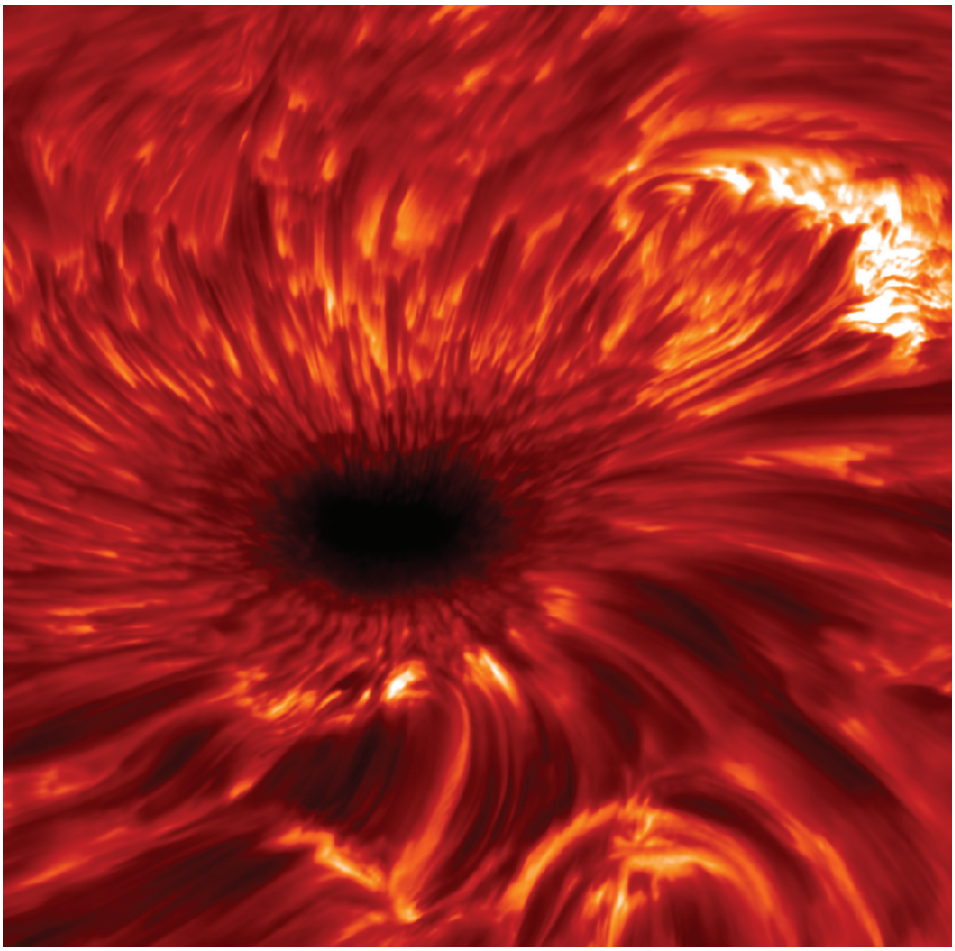

Figure 1.7 False colour image sample in Hα line centre of a classical sunspot exhibiting the characteristic fibrillar structures fanning out from the sunspot and connecting to surrounding network areas. The displayed area is about 54″ (39,000 km) squared. The image was obtained on June 28, 2010 using SST/CRISP and images the same sunspot as Fig. 1.6.

et al. 2004; Keller et al. 2004), it has been shown that these magnetic elements are bright because of the locally enhanced magnetic field, resulting in a lower gas density and opacity, consequently allowing to observe deeper-lying and hotter plasma. Stronger magnetic field concentrations generally show up as larger "dark holes" in the photospheric granulation pattern (i.e., pores and sunspots), as in those cases the magnetic field is strong enough to inhibit regular granulation (Cattaneo et al. 2003). Sunspots and their dynamics are discussed in more detail in Section 1.2.2.

Closer observations of the chromosphere, and especially those in the hydrogen Balmer α line at 6563 Å (Hα hereafter), show that it is characterised by a fibrillar structure spanning supergranular cells and fanning out from sunspots

to connect to surrounding network or plage, a morphology that is evident in Fig. 1.7. This morphology has long been thought to reflect the magnetic topology in the chromosphere, although recent studies (de la Cruz Rodríguez & Socas-Navarro 2011) would seem to suggest this is not always the case. In the particular case of the sunspot-connecting fibrils, these structures are referred to as the *superpenumbra*. The transition point in chromosphere between the gas-dominated atmosphere below and the magnetic field dominated corona above (i.e., $\beta \sim 1$) is typically referred to as the *canopy*, which is often used interchangeably to describe the thick fibril structures visible at Hα line centre.

The tenuous corona ($\beta \ll 1$) is dominated by large-scale loop structures that are filled with hot plasma (see Figs. 1.1 and 1.2). The high coronal temperatures were first implied by the identification of lines in coronal spectra corresponding to transitions between highly ionised states of iron (Edlén 1945). Grotrian (1934) had already observed these spectral lines in the early 1930's, but erroneously concluded them to be due to a newly observed element "coronium". With the realisation that the corona is at least a factor 200 hotter than the lower solar atmosphere arose the so-called "coronal heating problem", i.e., the question how it can have such high temperatures, while the underlying atmosphere is so much colder. Despite numerous efforts to find an explanation ever since, this long-standing issue in solar physics remains currently unanswered. Imaging of most coronal plasma and structures is not directly possible with a ground-based instrument like CRISP, as it requires observations in the (extreme) ultraviolet for which our atmosphere is opaque. However, not all plasma in the corona is hot: both *prominences* (clumps of dense material suspended in the corona against gravity by the magnetic fields; also called *filaments* when observed on-disc) and *coronal rain* (condensations that form near coronal loop apices and start sliding down under influence of gravity) can be observed with traditionally chromospheric lines like Hα and Ca II H, implying the plasma that constitutes these phenomena is at much lower temperatures than the ambient corona. Coronal rain is discussed in more detail in Section 1.2.5.

1.2.2 Sunspots

Pores and sunspots are the signatures of strong magnetic fields extruding from the solar interior into its atmosphere and are an integral component of active regions. Pores have typical sizes of one up to a few granules (i.e., a few thousand kilometres), but can in some cases have diameters as large as 7000 km (Thomas & Weiss 2008). However, the most prominent photospheric features are sunspots. They come in different sizes and configurations, and although the smallest may be only 3500 km across (Bray & Loughhead 1964), it is not uncommon for them to have diameters exceeding that of the Earth, even by an order of magnitude (Solanki 2003; Thomas & Weiss 2008). Typically, they appear in sunspot groups, consisting of two main sunspots of opposite polarity, accompanied by a number of smaller pores.

In its basic form, a sunspot consists of a dark, pore-like umbra surrounded by

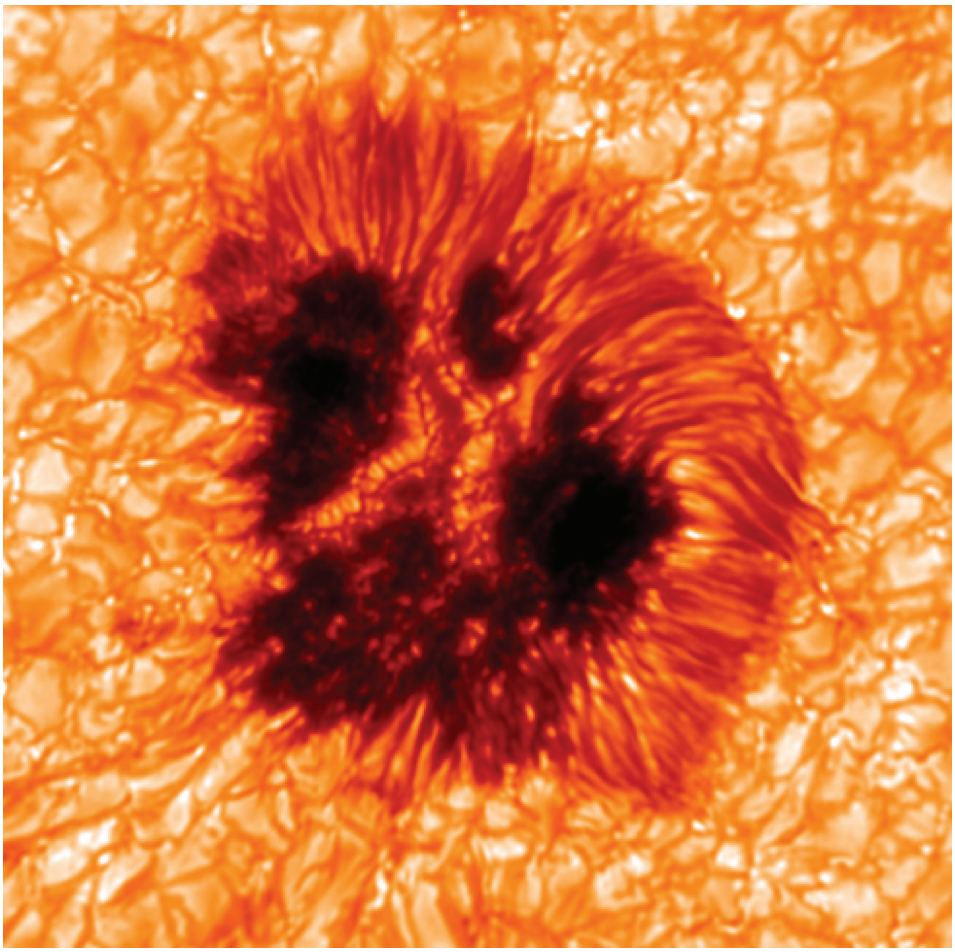

Figure 1.8 False colour sample of an irregularly shaped sunspot where the umbra is traversed by several light bridges. The displayed area is about 29″ (21,000 km) squared. The image was observed in the blue wing of Fe I 6301 Å with SST/CRISP on July 4, 2009. The corresponding data set was analysed by Rouppe van der Voort et al. (2010).

a brighter penumbra consisting of filamentary structures aligned roughly radially from the sunspot's centre (i.e., one could consider sunspots to be pores with a penumbra and, conversely, pores to be sunspots without penumbrae). Depending on the magnetic field configuration and the evolutionary stage the sunspot is in, the penumbra may be more or less axisymmetric and the umbra may be traversed by one or more light bridges. Also, trailing sunspots are usually less symmetrically shaped and stable than leading sunspots (Thomas & Weiss 2008). Figure 1.8 shows an example of such an irregular sunspot, with multiple light bridges and a penumbra only on side, in contrast to the sunspot in Fig. 1.6.

Although the umbra appears dark in most solar images, it does contain dynamic substructure in the form of so-called umbral dots that become visible with

proper scaling of the images (e.g., they are only sparsely visible in both Figs. 1.6 and 1.8). They have typical sizes of up to 200 km (Beckers & Schröter 1968; Sobotka & Hanslmeier 2005) and average temperatures ranging between 4600–5500 K (Sobotka & Hanslmeier 2005; Kitai et al. 2007). From simulations, Schüssler & Vögler (2006) predicted that umbral dots may have a "coffee bean"-like morphology, showing up as slightly elongated bright spots traversed by a central dark lane, which was later corroborated in an observational study by Ortiz et al. (2010). Combined with their velocity properties this morphology can be explained as convective plumes overshooting into the dark umbra.

Given observations of high enough spatial resolution, substantial substructure can be found in penumbral filaments as well. Most notable are the penumbral grains (Muller 1973a; Muller 1973b) of which the bright penumbra filaments appear to consist and the dark cores of those filaments, which were discovered shortly after commissioning of the SST (Scharmer et al. 2002). The penumbral grains generally migrate inwards in the inner penumbra (and sometimes even detach to become umbral dots, Muller 1973a) and outwards in the outer penumbra (Sobotka et al. 1999; Sobotka & Sütterlin 2001).

The (inverse) Evershed effect

Based on Doppler measurements, John Evershed (1909a) found that the general dynamics of the photospheric penumbra is one of a radial outflow, which was later named after him. The phenomenon has been studied extensively ever since and the velocities are typically observed to increase from a few km s^{-1} near the umbra-penumbra boundary up to about 10 km s^{-1} at the outer penumbral edge, although temporal variations in the outflow velocity have also been reported (e.g., Shine et al. 1990; Rimmele 1994; Shine et al. 1994; Rouppe van der Voort 2003). In a subsequent paper, Evershed (1909b) also suggested that a similar, but inversely directed flow might exist higher up in the chromosphere. It was not until St. John (1913) that the presence of this inverse Evershed flow was indeed confirmed. Generally, Doppler maps of the superpenumbra show plumes with a Doppler signal implying in- and downward directed flows of approximately 10 km s^{-1}, although St. John (1913) measured much lower average velocities of about 3 km s^{-1}. The latter is comparable to studies by Haugen (1969), Bones & Maltby (1978), Alissandrakis et al. (1988), and Dere et al. (1990), while both measurements of single absorbing elements in the Hα spectra (e.g., Haugen 1969) and filtergram studies (e.g., Beckers 1962; Maltby 1975) have yielded higher velocities of up to 50 km s^{-1}. The inverse Evershed effect has also been observed in the transition region, at typical line-of-sight velocities of 15 km s^{-1} (e.g., Kjeldseth-Moe et al. 1993; Dere et al. 1990; Teriaca et al. 2008) up to 20–30 km s^{-1} (Alissandrakis et al. 1988), but it has not been as extensively studied as in the chromosphere.

For the driving mechanism behind the photospheric Evershed effect mainly three models have been debated in the past: the *siphon flow model*, the *rising flux tube model* and the *"gappy penumbra" model*.

The siphon flow model was first proposed in the context of the Evershed effect by Meyer & Schmidt (1968) and adopted by many other authors as its explanation (cf. e.g., Alissandrakis et al. 1988; Thomas 1988; Dere et al. 1990; Montesinos & Thomas 1997), in some cases also extending it to the inverse Evershed effect. A siphon flow results from a magnetic and gas pressure imbalance between the footpoints of a magnetic flux tube. As the gas and magnetic pressure must be balanced in- and outside the flux tube, the difference in magnetic pressure will cause an opposite difference in gas pressure, resulting in a flow from the high (low) to the low (high) gas (magnetic) pressure footpoint. Figure 1.9 shows a schematic view of this principle.

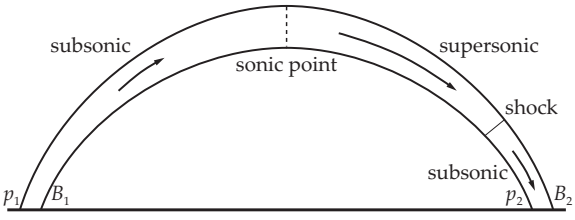

Figure 1.9 Cartoon showing the principle behind a siphon flow in a flux tube. With gas pressure p and magnetic pressure B in balance, if $B_1 < B_2$ then necessarily $p_1 > p_2$ and plasma will start flowing from footpoint 1 to footpoint 2. Depending on the internal loop structure, the flow solution may be subsonic throughout, go from subsonic to supersonic and to subsonic again (through a shock) or be supersonic throughout (although the latter is physically unrealistic in the situations considered here). The location of the sonic point and the shock are equally dependent on the loop structure; their positions in the above cartoon are merely illustrative. After similar cartoons in Meyer & Schmidt (1968) and Thomas (1988).

The second model builds on the rise and expansion of flux tubes from the deep, sub-photospheric penumbra. Schlichenmaier et al. (1998a,b) proposed this model in which single heated flux tubes rise through buoyancy, but are prevented from doing so further once above the photosphere due to its increased density (as a result of radiative losses) and a more stable background stratification. The upflow at the penumbral footpoint continues as a radial outflow above the photosphere, thus constituting the Evershed flow. In essence, this scenario is equivalent to the siphon flow model, however, no strong magnetic field concentrations at the outer penumbral edge are necessary to drive the flow in the rising flux tube model. Several authors (e.g., Hirzberger & Kneer 2001; Borrero et al. 2005; Rimmele & Marino 2006; Jurčák & Sobotka 2007)have found at least partial correspondence between their observational results and the model by Schlichenmaier and co-workers.

The "gappy penumbra" model model relies on thermal convective motions to drive an outward flow in the penumbra. The idea that thermal convection could produce the penumbral fibrils was first advanced by Spruit & Scharmer (2006), inspired by the discovery of dark-cored penumbral fibrils by Scharmer et al. (2002). Spruit & Scharmer (2006) proposed a mechanism where heating occurs through field-free convection taking place just below the photospheric surface in radially aligned field-free gaps. Even though the existence of an Evershed flow is not required in this "gappy penumbra" model *per se*, the scenario does allow for its presence. Realistic magnetohydrodynamic (MHD) simulations of sunspot struc-

ture (albeit not of a full sunspot) by both Heinemann et al. (2007) and Rempel et al. (2009b), as well as simulations of a full sunspot embedded in granulation (Rempel et al. 2009a; Rempel 2011) have confirmed the basic ideas of Spruit & Scharmer (2006) and provide further support for the convective nature of the photospheric Evershed effect. Nordlund & Scharmer (2010) and Scharmer et al. (2011) argue that, as it allows for the presence of outward flows as a natural result of the sub-photospheric convection – without the need to invoke the more idealistic setup required by the siphon flow and rising flux tube models – the convective driving mechanism provides the most elegant and plausible solution.

For the inverse Evershed effect, several driving mechanisms have been suggested before, but the siphon flow model currently offers the most widely accepted explanation (e.g., Haugen 1969; Maltby 1975; Alissandrakis et al. 1988; Dere et al. 1990; Boerner & Kneer 1992; Kjeldseth-Moe et al. 1993; Montesinos & Thomas 1997), and the most recent studies on the photospheric and chromospheric Evershed flows would thus suggest both are driven by a different mechanism. However, as the advanced 3D MHD models that allow simulation of a full sunspot currently only reach up to the photospheric level, considerable advancement in the understanding of the inverse Evershed effect can be expected once the simulation of full active regions throughout all atmospheric layers becomes computationally feasible.

Sunspot oscillations

Both the umbra and superpenumbra have been found to oscillate when observed in chromospheric lines (e.g., Hα or Ca II 8542 Å), which is not surprising given that the solar atmosphere is permeated with waves. Solar oscillations were first observed by Leighton et al. (1962), who found a predominant mode with a period of 5 min. In the photosphere it is these oscillations that have the largest amplitude, while 3-minute oscillations are generally more prevalent in the chromosphere above (Stix 2002).

So-called umbral flashes were discovered in the chromosphere by Beckers & Tallant (1969), while shortly after running penumbral waves were reported independently by Zirin & Stein (1972) and Giovanelli (1972). Despite their naming, the latter occur in the superpenumbra rather than the penumbra of sunspots. Zirin & Stein (1972) also suggested umbral flashes and running penumbral waves could be related. Several recent studies (e.g., Alissandrakis et al. 1998; Tsiropoula et al. 2000; Christopoulou et al. 2001; Rouppe van der Voort et al. 2003) seem to confirm this picture, although there appears to be a debate as to whether umbral flashes trigger running penumbral waves (Christopoulou et al. 2001) or whether both phenomena are rather the manifestation of the same oscillatory phenomenon (Alissandrakis et al. 1998; Tsiropoula et al. 2000; Rouppe van der Voort et al. 2003).

Beckers & Tallant (1969) reported typical umbral flash propagation speeds of 40 km s^{-1} and Wittmann (1969) measured speeds of up to 70 km s^{-1}, while much smaller proper motion, of the order of 10–15 km s^{-1} (occasionally exceeding 20 km s^{-1}), was found by e.g., Rouppe van der Voort et al. (2003). Running

penumbral waves, on the other hand, have typical proper motion of less than 20 km s^{-1}, e.g., Zirin & Stein (1972) reported 10 km s^{-1}, Alissandrakis et al. (1992) found an average of 15 km s^{-1}, Christopoulou et al. (2001) measured 6–18 km s^{-1} and Rouppe van der Voort et al. (2003) reported propagation speeds of 4-7 km s^{-1}.

1.2.3 Ellerman bombs

Discovery and spectral signatures

In 1917 Ferdinand Ellerman discovered what he termed "solar hydrogen bombs" (eventually renamed Ellerman bombs by other authors) in spectra of the Hα, Hβ and Hγ lines. He observed several cases of "a very brilliant and very narrow band extending four or five angstroms on either side of the [Hα] line, but not crossing it", lasting for a few minutes. Figure 1.10 shows in the top panels two sample spectra from his paper (Ellerman 1917) where these bright bands are visible. Although the brightenings do not cross the central line, in some cases the latter appears narrowed (e.g., the Ellerman bomb in the top right panel). Because of their general spectral appearance, Severny (1956) suggested the term "moustaches" to denote Ellerman bombs and Bray & Loughhead (1974) proposed this as a better terminology. Nonetheless, both terms have survived in the extensive literature that has been published since, possibly because "moustache" is not as much descriptive of the Ellerman bomb morphology as it is of its spectrum.

On average Ellerman (1917) found the width of the brightenings to be about 8 Å, but in some rare cases they extended out to 15 Å on either side of the Hα line. Similar results were obtained by Severny (1956), Bruzek (1972) and Kitai (1983), who reported brightenings of 30 Å, 10 Å and 15–20 Å wide, respectively. Apart from their broad emission wings, Ellerman bombs have often been reported to display an asymmetric spectral profile (cf. Severny 1968; Engvold & Maltby 1968; Koval & Severny 1970; Bruzek 1972; Kitai 1983; Fang et al. 2006; Socas-Navarro et al. 2006; Pariat et al. 2007; Hashimoto et al. 2010). The most common is a blue-asymmetry, i.e., where the blue wing is brighter than the red wing, but opposite asymmetries have also been observed. Either may be explained by the presence of overlying, flow-carrying fibrils that cause spectral asymmetries due to Dopplershifts (cf. Bruzek 1972; Kitai 1983; Dara et al. 1997; Rutten et al. 2013).

Visibility and morphology

Although Hα is the main diagnostic for studying Ellerman bombs, they have also been observed in other spectral lines, such as Ca II 8542 Å (e.g., Fang et al. 2006; Socas-Navarro et al. 2006; Pariat et al. 2007), Ca II H (e.g., Matsumoto et al. 2008a; Hashimoto et al. 2010; Herlender & Berlicki 2011), and in the 1600 Å UV-continuum (e.g., Qiu et al. 2000; Georgoulis et al. 2002; Pariat et al. 2007; Berlicki et al. 2010; Herlender & Berlicki 2011). For a long time, Ellerman bombs have been observed in imaging as round, to slightly elongated bright structures of about 1″–2″ across (although sizes of up to 5″ have also been reported in some studies) surrounding sunspots and in active regions in general (see the bottom panel

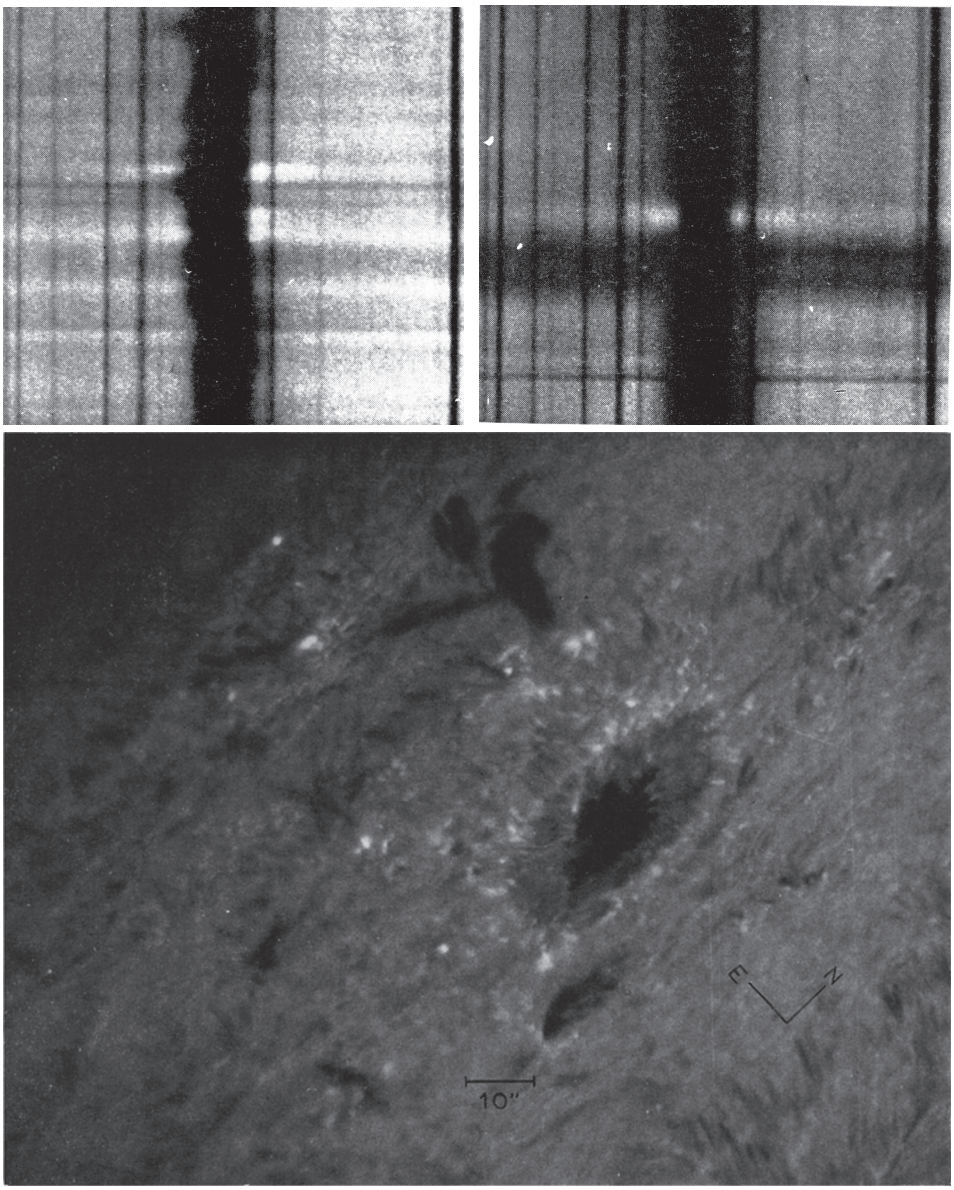

Figure 1.10 Spectral and filtergram signature of Ellerman bombs in older observations. *Top panels*: Hα spectra of Ellerman bombs from the discovery paper by Ellerman (1917). The displayed spectral range is roughly 15 Å. Reproduced by permission of the AAS. *Bottom panel*: Active region with multiple sunspots showing examples of "moustaches" (bright points) at close to 1″ resolution at H$\alpha+\frac{7}{8}$ Å. Reprint of Fig. 1 from Roy & Leparskas (1973), with kind permission from Springer Science and Business Media.

of Fig. 1.10 and, e.g., Bruzek 1972; Kurokawa et al. 1982; Nindos & Zirin 1998; Georgoulis et al. 2002). Their proper motions are of the order of 0.5–1.5 km s^{-1} (Georgoulis et al. 2002; Watanabe et al. 2011, **Paper I**; Nelson et al. 2013), similar

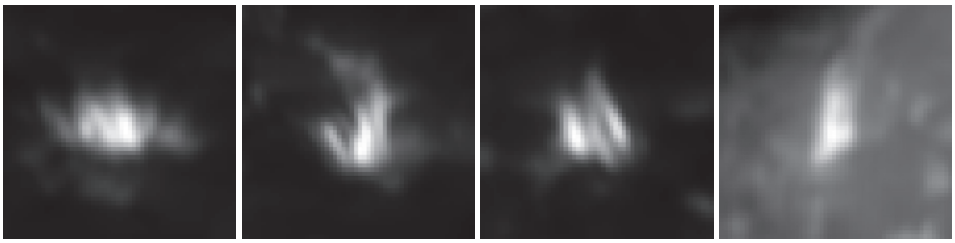

Figure 1.11 Close-up examples of Ellerman bombs as observed in Hα with SST/CRISP on June 28, 2010 (*first three panels*) and May 7, 2011 (*last panel*). Each panel is 3.″3 (roughly 2400 km) squared. The length of the substructures is typically about 1″, while the widths are of the order of 0.″2–0.″3.

to that of (inter)network bright points (e.g., Sheeley 1969; Harvey & Harvey 1973; Muller & Mena 1987; de Wijn et al. 2008).

With the advent of high-resolution observations using telescopes such as *Hinode* or the SST, substantial substructure within Ellerman bombs has been uncovered in more recent studies. For instance, Hashimoto et al. (2010) found average substructure sizes of about 0.″2 in width and 0.″6 in length, in analysing Ca II H data from *Hinode*. Similar sizes were also observed for Ellerman bombs in Hα data obtained with CRISP as analysed by Watanabe et al. (2011, **Paper I**). In the limb-ward view of those data, the Ellerman bombs showed clear flaming, jet-like morphology and dynamical changes in the substructure on the time scale of mere seconds, both reminiscent of so-called *chromospheric anemone jets* (Shibata et al. 2007; Morita et al. 2010; Nishizuka et al. 2011). Figure 1.11 shows examples of fine structure in Ellerman bombs as observed with CRISP at the SST.

Driving mechanism and energetics

The Ellerman bomb driving mechanism is generally accepted to be magnetic reconnection (e.g., Georgoulis et al. 2002; Pariat et al. 2004; Watanabe et al. 2008; Matsumoto et al. 2008b; Hashimoto et al. 2010), in which the energy stored in the magnetic field is released as the field reconfigures, for instance through Sweet-Parker reconnection (Parker 1957; Sweet 1958). The actual field configuration producing Ellerman bombs remains a matter of debate, in part because of observations indicating Ellerman bombs occur both in bipolar and unipolar regions. Several models have been proposed for Ellerman bombs occurring, for instance, as a result of emerging flux reconnecting with existing fields (Watanabe et al. 2008; Hashimoto et al. 2010; Morita et al. 2010), unipolar shearing fields (Georgoulis et al. 2002; Watanabe et al. 2008) and reconnection in resistive, undulatory ("sea-serpent") flux emergence (e.g., Georgoulis et al. 2002; Pariat et al. 2004; Matsumoto et al. 2008a). The latter configuration has also been studied numerically by Nozawa et al. (1992), Yokoyama & Shibata (1995), Litvinenko (1999), Isobe et al. (2007), and Archontis & Hood (2009). Figure 1.12 shows idealised cartoons of these reconnection scenarios.

Estimates of Ellerman bomb energy releases puts them in the *nanoflare* (Parker

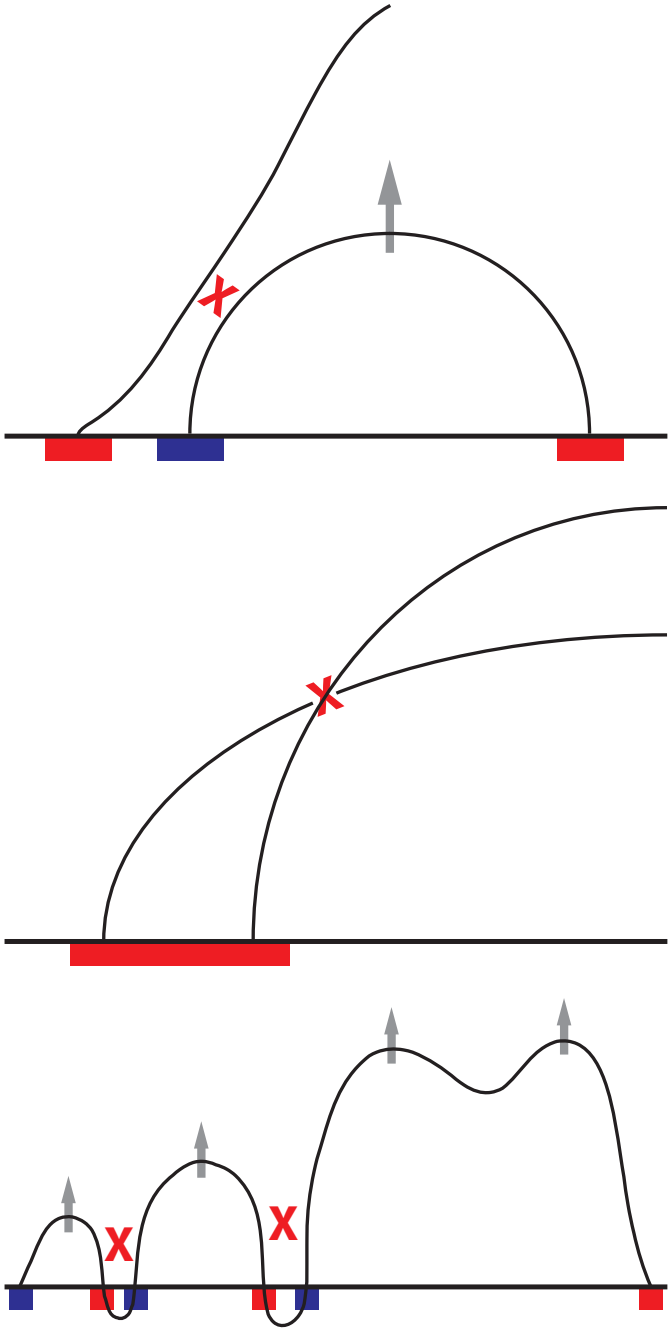

Figure 1.12 Cartoons of three different reconnection scenarios resulting in Ellerman bombs: reconnection between emerging bipolar flux and existing (near-)vertical fields (*top*), shearing reconnection between unipolar fields (*middle*) and reconnection between opposite walls of undulatory ("sea-serpent") emerging flux (*bottom*). The thick horizontal line represent the photospheric surface, the curved lines correspond to field lines, while opposite polarities are indicated with red and blue and reconnection sites are indicated by the red crosses. After similar cartoons in, e.g., Georgoulis et al. (2002), Pariat et al. (2004), Matsumoto et al. (2008a), Watanabe et al. (2008), Hashimoto et al. (2010) and Morita et al. (2010).

1988; Parnell & Jupp 2000) ballpark of 10^{24}–10^{27} erg. Most studies report typical energies of about 10^{26}–10^{28} erg (e.g., Georgoulis et al. 2002; Fang et al. 2006; Morita et al. 2010), but Nelson et al. (2013) recently calculated Ellerman bomb energies on the lower nanoflare end (10^{22}–10^{25} erg).

Upper atmosphere response

Multi-diagnostic analysis of Ellerman bombs has given rise to reports co-relating Ellerman bombs in the lower atmosphere with brightenings or surges in the upper atmosphere. For instance, Roy (1973), Roy & Leparskas (1973), Shibata et al. (1982), Matsumoto et al. (2008b) and Guglielmino et al. (2010) reported on Ellerman bomb-related surges, while Shimizu et al. (2002) found a possible connection between Ellerman bombs and microflares. Schmieder et al. (2004), on the other hand, found only one case of an X-ray brightening coinciding with a bright Ellerman bomb and brightening in TRACE 171 Å amongst hundreds of Ellerman bombs and concluded that most Ellerman bombs do not have a visible effect on the upper atmosphere. Rutten et al. 2013 suggest that much of the apparent coincidence between Ellerman bombs and upper atmosphere signal can be attributed to either the low resolution of the data or to misidentification of Ellerman bombs in the first place. Similarly, in work included in this thesis, Vissers et al. (2013, **Paper II**) find no perceivable effects on the higher atmosphere as a result of Ellerman bombs in the photosphere below.

1.2.4 Dynamic fibrils and spicules

Another class of dynamic solar features that displays jet-like morphology comprises on-disc dynamic fibrils (e.g., Hansteen et al. 2006; De Pontieu et al. 2007a) and mottles (e.g., Beckers 1968; Tsiropoula et al. 1994; Suematsu et al. 1995), off-limb spicules (e.g., Beckers 1968; Sterling 2000) and so-called rapid blueshifted excursions (Langangen et al. 2008b; Rouppe van der Voort et al. 2009). Figure 1.13 shows examples of the ubiquity of these features in high-resolution imaging at two different viewing angles. These phenomena are similar in morphology and dynamics, and part of them probably share a similar (if not the same) driving mechanism.

Dynamic fibrils are active region phenomena that shoot up at typical velocities of 10–30 km s^{-1}, decelerate to zero velocity and then fall back again (usually to the same spatial point) under the influence of gravity and are likely shock-driven (Suematsu 1990; Hansteen et al. 2006; De Pontieu et al. 2004; De Pontieu et al. 2007a; Heggland et al. 2007). According to Beckers (1968) their typical lifetimes are 3–15 min and they reach average heights of 5000–9000 km. More recent studies, like for instance De Pontieu et al. (2007a), seem to agree on the part of lifetimes (De Pontieu et al. reported lifetimes between 2–11 min, with a 5 min average), but find much shorter dynamic fibril lengths (400–5200 km, 1250 km on average). Spectroscopically, their up and down motion translates to a blueshift of the line core and subsequent movement of that core back through line centre to

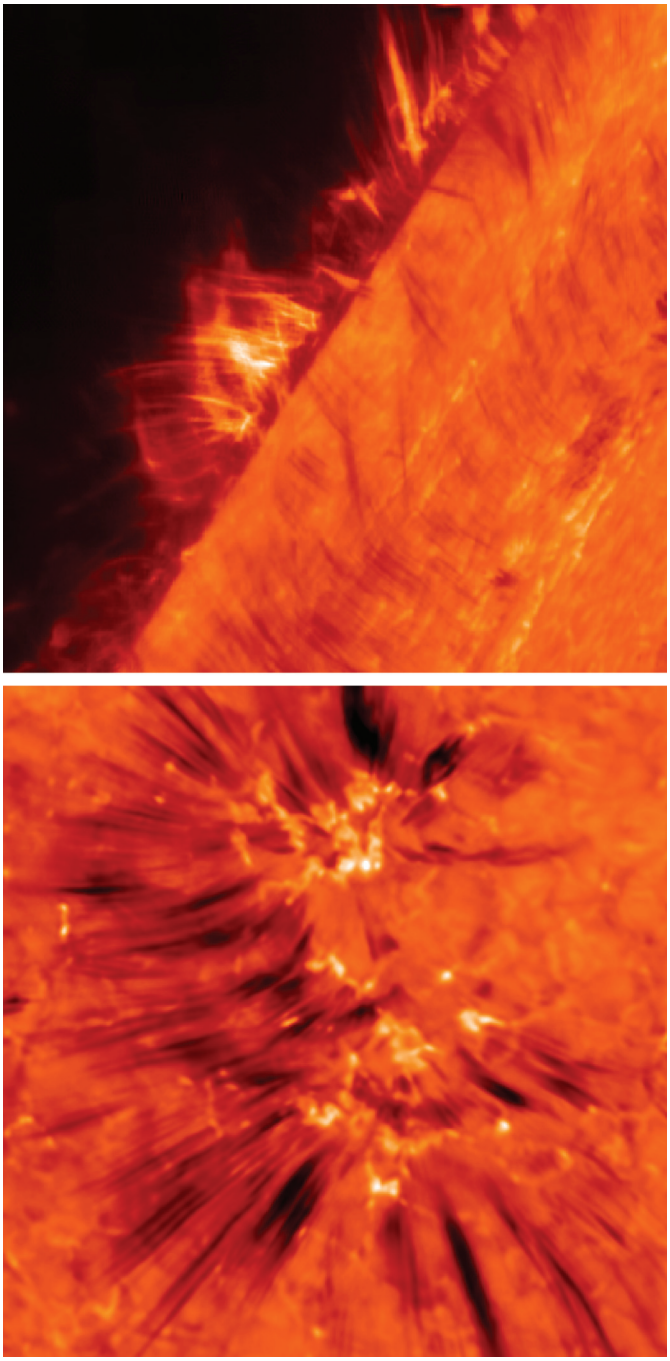

Figure 1.13 Examples of spicules and rapid blueshifted excursions as observed with SST/CRISP in the wings of Hα. *Top*: Spicules observed as a superposition of (mostly straight) bright, grass-like structures at the limb in the red wing (at a Doppler shift of $+37\,\mathrm{km\,s^{-1}}$) on May 10, 2009. The image covers about 30″ (21,500 km) squared. *Bottom*: RBEs observed as slender dark streaks emanating from the bright network in the photosphere in the blue wing (at $-35\,\mathrm{km\,s^{-1}}$) on June 27, 2010. The image covers about 24″ (17,500 km) squared. The corresponding data set was recently analysed by Sekse et al. (2012).

the red wing Langangen et al. (2008a, 2008c). Because of their morphological and dynamical properties, Hansteen et al. (2006) and De Pontieu et al. (2007a) suggested that dynamic fibrils could be related to spicules, a phenomenon that has been observed for almost 140 years in the quiet Sun at the limb (cf. Beckers 1968; Sterling 2000). On the other hand, Rouppe van der Voort et al. (2007) provided observational evidence that some quiet Sun mottles being driven by magnetoacoustic shocks. Given their dynamical and morphological properties, this would suggest they constitute a similar phenomenon, only located in regions of different magnetic activity.

Around the same time, De Pontieu et al. (2007b) proposed a classification into two types of spicules, based on *Hinode*/SOT observations. While a Type I spicule displays up and down motion, very much like dynamic fibrils and mottles, a Type II spicule is characterised by only upward motion, lacking the subsequent downfall. Recent studies suggest that this is caused by the spicule plasma being heated out of the passband in which it is initially observed (De Pontieu et al. 2011; Sekse et al. 2013a). Pereira et al. (2012) report on an extensive study of spicules in different regions and find a clear distinction between two classes of spicules. From their analysis, Type I spicules have relatively long lifetimes (150–400 s) and low velocities (15–40 km s^{-1}), while Type II spicules live shorter (50–150 s) but move much faster (30–110 km s^{-1}).

Langangen et al. (2008b) observed on-disc features in Ca II 8542 Å IBIS data that show a spectral equivalent behaviour to these Type II spicules, namely a widened line profile in the blue wing of the spectral line, without any subsequent signature in the red wing. Based on their spectroscopic properties, Langangen et al. (2008b) called these features rapid blueshifted excursions (RBEs) and suggested a relation to Type II spicules. Actual evidence for RBEs being the on-disc counterparts of Type II spicules was first presented by Rouppe van der Voort et al. (2009), who also reported lifetimes ranging between 10–120 s (peaking around 40 s), projected velocities of up to 120 km s^{-1} and transverse velocities of up to 20 km s^{-1}(average around 8 km s^{-1}). Recently, Sekse et al. (2012, 2013a, 2013b) have expanded considerably on the available RBE statistics by analysing CRISP Hα and Ca II 8542 Å observations, providing further evidence for the spicule Type II-RBE connection. They report RBE lengths between 1000–6000 km (averaging at some 3000 km), lifetimes between 5–120 s (with an average of about 20–30 s), longitudinal velocities of up to 125 km s^{-1} and transverse velocities of up to 55 km s^{-1} (although the majority has transverse velocities around 10 km s^{-1}).

1.2.5 Intermittent flows and waves

Observations in chromospheric lines also reveal a number of intermittent, transient phenomena that have a (sometimes bright) blob-like morphology and fast dynamics. They are typically observed to follow similar paths as outlined by the fibrillar canopy observed in Hα. These could be waves, using the magnetic field canopy as waveguides and the blob-like morphology then being a signature

of plasma compression by the wave fronts. Alternatively, they could represent actual mass flows, in which the blobs would correspond to condensations propagating under the influence of some external force (gravity, Lorentz force or gas pressure). However, distinguishing these two scenarios is not always straightforward. In the following, a few of these phenomena are discussed in some more detail.

Chromosphere waves

Recently, Sánchez-Andrade Nuño et al. (2008) reported on chromospheric magneto-acoustic waves that manifest themselves as (trains of) propagating blobs in Hα observations taken with the "Göttingen" Fabry-Pérot spectrometer at the German Vacuum Tower Telescope on Tenerife (Canary Islands). These dark blobs have average sizes of 360×725 km and typical phase speeds of a few up to 30–40 km s^{-1}, generally also displaying transverse oscillations as they propagate. Wedemeyer-Böhm (2010) analysed Ca II 8542 Å CRISP data and observed bright blob-like features propagating at projected velocities below 10 km s^{-1} along neighbouring fibrils in the chromospheric canopy, which were explained as the manifestation of a wavefront expanding below the canopy.

A phenomenon with somewhat similar morphology but much faster propagation speeds was recently studied by Lin et al. (2012), who expanded on earlier analysis of SOUP data by van Noort & Rouppe van der Voort (2006) by also considering CRISP Hα imaging spectroscopy. They describe *dynamic bright blobs* that are visible at and close to Hα line centre (Doppler velocities of up to $\pm$5–10 km s^{-1}). They have lifetimes of 1–2 min, propagate at velocities of 45–110 km s^{-1} as measured in the plane of the sky (in some cases also displaying transverse motions) and have typical sizes of 400–1200 km. The authors concluded that these blobs are a manifestation of magneto-hydrodynamic fast-mode wave pulses.

Coronal rain

Coronal rain is a phenomenon observed in active region coronal loops and consists of condensations that slide down along the legs of those loops under the influence of gravity. Although technically a coronal phenomenon, coronal rain has also been observed in chromospheric lines, in some cases even down to the photospheric level. As pointed out before, this would imply the constituting plasma is at chromospheric temperatures, much lower than the surrounding corona. The phenomenon has been known since the seventies from observations in Hα (Kawaguchi 1970; Leroy 1972) and in the extreme ultraviolet (Foukal 1976; Foukal 1978). It has mostly been treated as relatively rare (Schrijver 2001), but the past decade has seen many advances in this area, both in terms of observations and numerical simulations.

Typical coronal rain velocities range from 10–20 km s^{-1} up to 150–200 km s^{-1} (e.g., Schrijver 2001; Müller et al. 2005; de Groof et al. 2005; O'Shea et al. 2007;

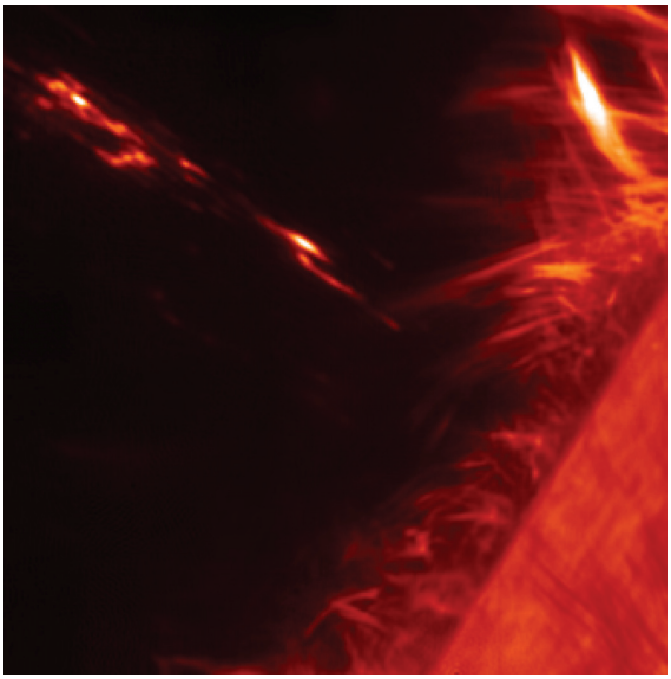

Figure 1.14 Examples of coronal rain condensations as bright, off-limb blobs in CRISP Hα data obtained on May 10, 2009 (same data set as depicted in the top panel of Fig. 1.13). The field-of-view covers about 30″ (21,500 km) squared. The coronal rain in these data was studied by Antolin & Rouppe van der Voort (2012).

Antolin & Rouppe van der Voort 2012; Antolin et al. 2012, **Paper IV**) and its individual condensations measure approximately 300 km in width and 750–900 km in length, as recently shown for both off-limb and on-disc cases by Antolin & Rouppe van der Voort (2012) and Antolin et al. (2012, **Paper IV**), respectively. The latter two studies have also provided estimates of coronal rain temperatures, suggesting these are typically slightly higher for off-limb cases than for on-disc cases, but between 5000–10,000 K on average in either case. Figure 1.14 shows examples of coronal rain at the limb in SST/CRISP observations in Hα.

Coronal rain blobs are generally accepted to constitute mass motion rather than waves (e.g., de Groof et al. 2005), with the condensations forming as a result of runaway cooling at (or close to) the loop apex. The process responsible for this is "catastrophic cooling" and was first advanced to explain coronal rain by Schrijver (2001). The idea behind it is that thermal non-equilibrium of the loop leads to a local condensation of plasma higher up in the loop and in turn, the condensation enhances the radiative losses, leading to further growth of the condensation and thus starting a runaway cooling process. Once the condensation has gained enough mass that it can no longer be sustained against gravity, it starts sliding down along the loop leg and becomes observable as coronal rain. This cooling-heating cycle and consequent formation of condensations has been well-reproduced in numerical simulations (e.g., Müller et al. 2003, 2004, 2005; Antolin et al. 2010).

In addition, studies by Aschwanden et al. (2001) and Aschwanden (2001) have shown that a majority of the coronal loops seems to be out of hydrostatic equilib-

rium, with footpoint-concentrated heating as a preferential solution to the steady-state loop models. As footpoint heating can ensure injection of mass into the coronal loop through chromospheric evaporation, this mechanism can provide dense enough loops for the thermal instability to play an essential role in driving the formation of coronal rain condensations.

1.3 Data visualisation and analysis

As instrumentation and computational resources have advanced over the past decades, it has become increasingly easy to obtain, produce and store large quantities of data. With new instruments entering the scene, new observing possibilities arise that allow for different or multiple data dimensions and the final data products have generally become more complex than before. In the particular case of the CRisp Imaging SpectroPolarimeter at the Swedish 1-m Solar Telescope, data are stored in multidimensional data cubes, easily exceeding 10 GB in size for typical cases. Although existing visualisation tools for 3-dimensional data can be (and in the past have been) forced to cope with this data structure, their ease of use and efficiency are limited when dealing with higher dimension data cubes, hence the need for a specialised visualisation and analysis tool.

The main requirements for a software tool is that it should (1) be able to cope with typical CRISP data, formatted in data cubes of three to five dimensions; (2) allow visualisation of data sets resulting from typical observing programmes, i.e., including multiple diagnostics; and (3) enable quick access to (practically) any cut through the data cube. Additionally, the tool should provide some basic in-programme analysis functionality that supports the data exploration process, and preferably allow visualisation of data of any origin (e.g., imaging data from other telescopes or synthetic data from 3D MHD simulations).

The CRIsp SPectral EXplorer (CRISPEX) is what materialised out of these needs and the remainder of this section offers an update of the appendix to **Paper III**, where CRISPEX was first introduced. As such, it provides an overview of the functionality and capabilities of the current release version of CRISPEX (version 1.6.3 at the time of writing), as well as an outlook on extensions and modifications that could (and in some cases, are to) be implemented in the foreseeable future.

1.3.1 The CRIsp SPectral EXplorer

CRISPEX is a widget-based tool programmed in the Interactive Data Language (IDL) aimed at providing visualisation and basic analysis functionality for essentially 5-dimensional data cubes. These five dimensions comprise the two horizontal spatial axes (i.e., x and y), time, wavelength and the Stokes parameter. Given its original purpose, CRISPEX is ideally suited for visualisation of imaging spectropolarimetry, but it can in principle handle any data provided these are formatted as described further below. CRISPEX has been most extensively used

with CRISP data (e.g., Rouppe van der Voort et al. 2009; Wedemeyer-Böhm & Rouppe van der Voort 2009; Antolin et al. 2010; Rouppe van der Voort et al. 2010; Wedemeyer-Böhm et al. 2012; Antolin & Rouppe van der Voort 2012; Lin et al. 2012; De Pontieu et al. 2012; Sekse et al. 2012, 2013a, 2013b; de la Cruz Rodríguez et al. 2013; and, most importantly, all four papers on which this thesis is based), but indeed also with DST/IBIS data (e.g., Schad et al. 2013), *Hinode* Solar Optical Telescope (SOT) data (e.g., Antolin & Verwichte 2011), SDO/AIA data (e.g., Wedemeyer-Böhm et al. 2012; **Paper II**) and synthetic data produced by the 3D MHD code *Bifrost*.

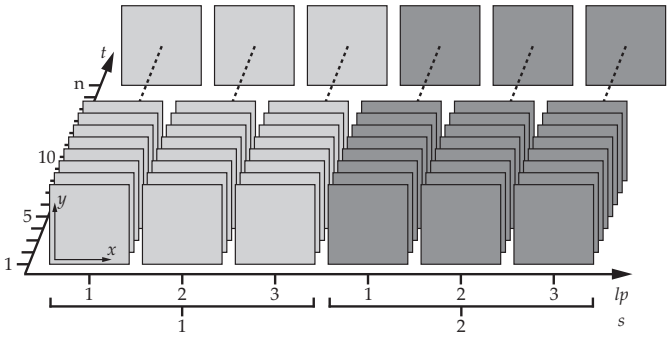

Figure 1.15 Schematic representation of data ordering in the third dimension of a spectrotemporal Stokes cube. The third dimension has been folded open into a wavelength axis *lp* and a temporal axis *t*. The data are ordered sequentially by Stokes parameter *s* with the images at each wavelength position for the first time step first, before going to the next time step.

In order for the functionality of CRISPEX to behave as expected the cubes need to be formatted in a particular way. The data dimensions may vary anywhere from three (e.g., a single spectral line scan with no temporal component or a time series of intensity images) up to five (e.g., a time series with full Stokes and spectral line information), but in practice the data are formatted as 3-dimensional cubes with higher dimensions "folded" linearly into the third dimension. In turn, the higher dimensions remain accessible through index subscription. Images are stacked according to wavelength first, Stokes parameter second and time third. Figure 1.15 shows a schematic representation of this data ordering for e.g., a time series of exposures in two Stokes parameters *s* covering three wavelength positions *lp*. One could consider the presence of Stokes information as an extension of the wavelength axis.

The programmatic structure of CRISPEX is currently such that the main programme sets up all variables necessary for data access and display, while a large number of subroutines (346 in CRISPEX v1.6.3) handle the different tasks that need to be performed. These tasks have been broken down to the point that the functionality of the subroutines can be re-used relatively efficiently, although at this point CRISPEX is neither fully object oriented nor modular. This is mainly because both the original procedure that CRISPEX is based on (a rewrite by Øystein Langangen for IBIS and CRISP data of yet older procedures), and the two visualisation tools for 3D cubes that served as inspiration for much of CRISPEX's structure and some of its initial functionality, XIMOVIE (developed by Øivind Wikstøl) and XSlice (developed by Alfred de Wijn), did not have such structure.

Functionality

The first two requirements outlined at the beginning of this section were the capability of processing typical CRISP data, as well as visualising data sets resulting from typical observing programmes. The first is handled intrinsically, as the initial version of CRISPEX was written with that particular purpose in mind. Although in that first version it was only capable of handling spectrotemporal cubes (i.e., time series of line profile scans), CRISPEX can now also process full Stokes data cubes (e.g., the example from Fig. 1.15). The second requirement is covered by several functionality features, but mainly through the option of displaying two data cubes (a main and a reference cube) side by side. The reference cube is currently constrained to having the same spatial dimensions as the main cube, but may have a different number of wavelength positions and time steps, i.e., it can either consist of a single spectral scan, a time series of images or a full spectrotemporal cube.

The third requirement concerned functionality to quickly access (practically) any cut through the data cube. Considering the original data product CRISPEX was written to handle (i.e., imaging spectropolarimetry) the main visualisations are:

1. the intensity image at any time step t and wavelength lp;
2. the spectrum as function of time at any combination of positional coordinates x and y;
3. the spectral profile at any combination of coordinates x and y, and time step t.

Figure 1.16 shows an example of the default windows loaded when CRISPEX is supplied with a spectrotemporal cube, where these visualisations are numbered accordingly. Adjustment of the displays to a particular combination of dimensional parameters (x,y,t,lp,s) can be achieved through sliders, selection buttons and cursor movement.

Part of the quick access to the data is a result of reading the data in to associate variables, which for most CRISP data is a bare necessity since the typical CRISP data cube is likely to exceed the available random access memory. An additional advantage is that one avoids the need to read in a full cube or keep that amount of data in memory throughout the session. However, this quick access comes at a penalty if all functionality is to be used. The dimensions of the image cube are ordered such that the intensity image can be easily retrieved, while other visualisations (like, e.g., the spectrum as function of time) would require building up an array by jumping through the data cube. For these other (mainly spectral) visualisations to be equally quick a second, spectral cube needs to be supplied which contains the same data, only ordered differently.

CRISPEX's in-built analysis functionality includes display of intensity as function of time (either at a specific position (x,y) or along an arbitrary spatial path through the data), the spectrum along a line with arbitrary length and angle centred on any coordinates (x,y) and a spatial measurement tool. The first, the space-

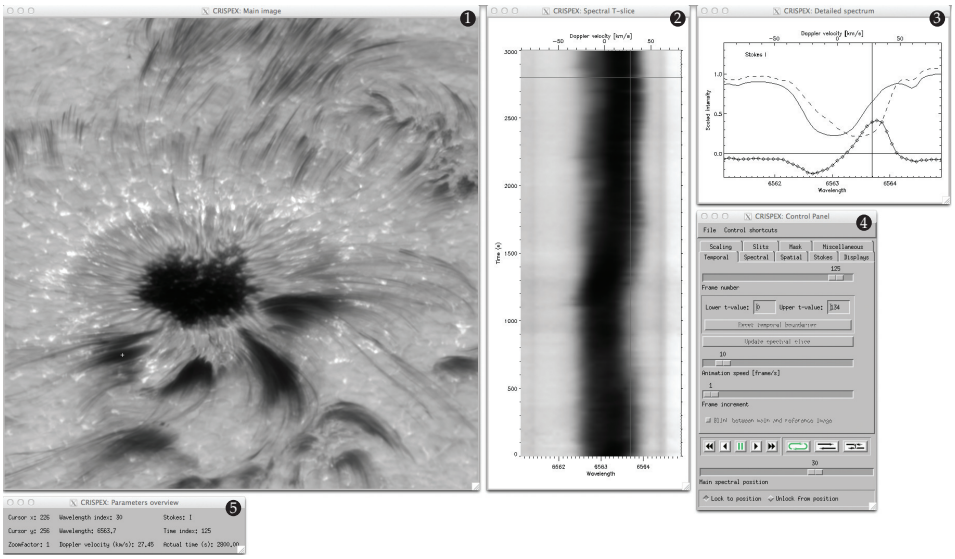

Figure 1.16 Default windows opened by CRISPEX upon loading a spectrotemporal data cube. Clockwise from top left: (1) main image, (2) spectrum versus time diagram, (3) detailed spectrum at (x,y,t), (4) control panel, and (5) parameters overview window.

time diagram visualisation, is the most developed analysis functionality. Definition of the path along which to extract the space-time diagram can be done either manually or from, for instance, a detection file. The space-time diagrams can subsequently be saved for both the main and reference cube, as well as restored in a later session. The spectrum along a line simulates a spectral slit with adjustable slit length and orientation and displays the instantaneous spectrum along that cut. Lastly, the spatial measurement tool allows determining the distance (in arc seconds and kilometres) between two cursor-defined points using the given pixel size of the data.

Other functionality includes Doppler image display (for spectral data, where the Doppler image is constructed on-the-fly from red and blue wing images), overlay of mask contours (supplied through a "mask cube" that may consist of a single 2-dimensional array or a time series of masks) and export functionality to save the image and/or spectral displays (either as MPEG movie, or JPEG or PNG image file).

1.3.2 Future opportunities

Since its initial release in 2009, CRISPEX has proven to be an effective visualisation tool for CRISP data that has been extensively used at the Institute of Theoretical Astrophysics in Oslo, but also elsewhere and for data from different sources. Nevertheless (or perhaps particularly because of such extensive use), there are some clear areas where the code could be further improved or extended.

Current development is primarily aimed at preparing CRISPEX for data from

the Interface Region Imaging Spectrograph (IRIS), which entails the largest overhaul since the original release version. This requires both data compatibility changes that allow CRISPEX to properly process the IRIS data cubes (which will adhere to the Flexible Image Transport System (FITS) standard), and extending its functionality to the slightly different data structure of those data. Necessarily, this will also require a makeover of the graphical user interface (GUI) to accommodate the new functionality, an opportunity that could be used to redo the GUI altogether to further streamline the user experience.

Further analysis and display functionality that could be implemented covers the extension of all functionality that is currently available for the main cube to the reference cube, e.g., allowing Stokes data cubes as reference data and enabling Doppler image display for the reference cube. Also, the current spectral slit functionality could be expanded to allow for curved paths instead of a straight line.

Other improvements that suggest themselves include proper modularisation, further condensation of common tasks in an effort to move towards a truly object-oriented code and enabling user-defined extensions or plug-ins. As pointed out before, CRISPEX v1.6.3 consists of a large number of subroutines that allow relatively efficient re-use of their functionality. However, they currently reside in a monolithic file of over 12,000 lines, which leaves clear room for improvement from a code maintenance point of view. A natural extension of the modularisation of CRISPEX would be to enable user-written plug-ins that could operate besides the core functionality. On one hand this would circumvent the problem of implementing and maintaining every single feature request (which is likely to increase to prohibitively time-consuming numbers with CRISPEX becoming the visualisation tool of choice for IRIS data), but more importantly, it would also offer customisation options to the user, making CRISPEX applicable to a wider variety of data and uses.

2

DYNAMICS OF FINE STRUCTURE IN THE ATMOSPHERE OF SOLAR ACTIVE REGIONS

This thesis presents a study of high-resolution observations of dynamics of fine structure in active regions. It is based on four papers, covering different phenomena that occur at different heights in the solar atmosphere: Ellerman bombs, flocculent flows and coronal rain. Although the phenomena are distinct, they share active regions as their predominant occurrence location, as well as the need for observations at high spatial, temporal and spectral resolution in order to be properly resolved and analysed. The combination of the CRisp Imaging SpectroPolarimeter and the Swedish 1-m Solar Telescope has allowed just that, thereby contributing tremendously to the research of such fine structure dynamics in the (primarily) lower solar atmosphere. In **Papers I**, **III** and **IV** only CRISP data were considered, while data obtained with the Atmospheric Imaging Assembly on the Solar Dynamics Observatory have also been analysed in **Paper II**. The four papers on which this thesis is based are:

I **Ellerman Bombs at High Resolution. I. Morphological Evidence for Photospheric Reconnection**
H. Watanabe, G. Vissers, R. Kitai, L. Rouppe van der Voort, and R. Rutten
The Astrophysical Journal 716 (2010), 154–166

II **Ellerman Bombs at High Resolution. II. Triggering, Visibility, and Effect on the Upper Atmosphere**
G. Vissers, L. Rouppe van der Voort, and R. Rutten
Submitted to The Astrophysical Journal (2013)

III **Flocculent flows in the Chromospheric Canopy of a Sunspot**
G. Vissers and L. Rouppe van der Voort
The Astrophysical Journal 750 (2012), 22

IV **On-disc coronal rain**
P. Antolin, G. Vissers, and L. Rouppe van der Voort
Solar Physics 280 (2012), 457–474

Following the plethora of photospheric and chromospheric dynamic phenomena discussed in the previous chapter, the next sections provide a summary of these papers. Section 2.1 covers **Papers I** and **II**, while Section 2.2 is concerned with **Papers III** and **IV**.

2.1 Ellerman bombs

2.1.1 Morphological evidence for photospheric reconnection

Paper I, Watanabe et al. (2011), offers a morphological and statistical study of Ellerman bombs in high-resolution imaging spectroscopy of Hα obtained on June 11, 2008 with SST/CRISP, covering a small sunspot with a rudimentary penumbra. Similar to the *Hinode*/SOT Ca II H data presented by Hashimoto et al. (2010), these data show that Ellerman bombs have substantial substructure down to the resolution limit of the telescope, but also that this substructure changes on the timescale of 1 s. The goal of this study is then to explain this morphology as well as gather statistics on the substructure sizes and dynamics.

Morphologically we establish the key properties of the observed Ellerman bombs to be that they (1) are rooted in the intergranular lanes and are visible only in the wings of Hα, but not close to or at line centre, (2) have upward, "jet"-like protrusions, (3) display small-scale inverted-Y morphology in some cases, (4) migrate along the network, while flaring repetitively, and (5) have fast variations in their fine structure during the flaring. The first property suggests the phenomenon is photospheric, as no signal is observed at higher, chromospheric altitudes sampled by the Hα line, while the second and third are indicative of a reconnection process similar to that of the chromospheric anemone jets (Shibata et al. 2007) introduced in Section 1.2.3. The last two properties, in turn, would point at repetitive reconnection as the magnetic field is pushed around by the moat flow and reorders itself on short timescales.

In total we identified 17 Ellerman bombs, their lifetimes ranging between 260–1302 s (566 s on average), baseline widths (i.e., at the network level) between 280–900 km (471 km on average) and jet extents of 540–1230 km (855 km on average). The jet extension speeds range between 3–20 km s^{-1} (8 km s^{-1} on average), which is comparable to those of chromospheric anemone jets reported by Shibata et al. (2007). Also, the lower end of our Ellerman bomb lifetimes overlaps with the lifetimes found for the anemone jets in a sunspot moat studied by Morita et al. (2010). The average Ellerman bomb proper motion along the network is 0.67 km s^{-1}, comparable to that of bright points in the sunspot moat (0.59–0.88 km s^{-1} from measuring 619 network bright points in the same study), which supports the idea that the repetitive flaring described before is a result of the field lines being swept around by the intergranular motions.

Evidence for bi-directional jets, a typical signature of reconnection in chromospheric anemone jets, was also found in some of the Ellerman bombs we studied, which agrees with similar reports by Matsumoto et al. (2008b) of bidirec-

tional motions in *Hinode* Ca II H observations of Ellerman bombs. Finally, two Ellerman bombs also appeared to set off a nearby surge in the chromosphere above, with Doppler shifts of up to 40 km s^{-1}. Such surge-triggering behaviour has been reported before (e.g., Roy 1973; Shibata et al. 1982; Matsumoto et al. 2008b; Guglielmino et al. 2010), but seems not to be a general property of Ellerman bombs, which indeed our results would seem to confirm.

Although the morphology and dynamics of the Ellerman bombs studied in **Paper I** are suggestive of repetitive reconnection, this cannot be conclusively demonstrated based solely on morphology. The question remains whether reconnection is indeed ongoing and in what particular magnetic field configuration that may occur. In order to further investigate that, simultaneous spectropolarimetric information is required, which was not available for the data studied in **Paper I**.

2.1.2 Triggering, visibility, and effect on the upper atmosphere

In **Paper II**, Vissers et al. (2013), we build on the work from **Paper I**, where we concluded that the morphology and dynamics of Ellerman bombs are reminiscent of reconnection events. The goals of **Paper II** are twofold: (1) study the Ellerman bomb(-related) signature in other diagnostics, covering the photosphere to the corona, and (2) determine the relation to the underlying magnetic field. To that end, we studied two SST/CRISP data sets, obtained on June 28, 2010 and May 7, 2011, respectively. The first data set contains imaging spectroscopy in both Hα and Ca II 8542 Å, while the other consists of Hα sampling in addition to Fe I 6301 Å Stokes information. For both data sets we also analysed simultaneous SDO/AIA data in the 1700 Å UV-continuum, He II 304 Å, Fe IX 171 Å, and Fe XIV 211 Å. Although multi-diagnostic analyses of Ellerman bombs have been performed before (e.g., Qiu et al. 2000; Georgoulis et al. 2002; Fang et al. 2006; Socas-Navarro et al. 2006; Pariat et al. 2007; Matsumoto et al. 2008a; Hashimoto et al. 2010; Berlicki et al. 2010; Herlender & Berlicki 2011), the study described in **Paper II** considers data with higher resolution (both spatially, spectrally and temporally, and in particular the simultaneous combination of those three) than previously available.

We define an automated detection algorithm that recovers most of the Ellerman bombs identified by eye, while minimising the number of false positives. The basic constraints are: Ellerman bomb-kernel brightness at least 155% above average (but allowing for adjacent pixels if at least 140% above average), minimum size of five pixels (0.″2–0.″3), minimum lifetime of $\sim$50 s (and allowing for detections to skip up to $\sim$50 s to compensate for variable seeing). Applying these constraints to the Hα data resulted in detection of 79 and 61 Ellerman bombs in the first and second data set, respectively, while 24 Ellerman bombs were detected in the Ca III images. The numbers from Hα detections are much smaller than either the prediction based on the birthrate reported by Zachariadis et al. (1987) or the results recently obtained by Nelson et al. (2013), but the brightness threshold we employ is also much more strict than that used by Nelson et al. (2013) or

suggested by Georgoulis et al. (2002).

Morphologically, the Ellerman bombs observed in Hα are the same as those observed in **Paper I**: they protrude from the network (occasionally with inverted-Y morphology) and display changes in their fine structure during their lifetime. Also, in most cases they migrate along the network with proper motions similar to that of the moat flow. Their morphology in Ca II 8542 Å is similar for some, but the majority does not show a good spatial overlap with the brightenings in Hα. In part this may be attributed to overlying, Dopplershifted fibrils that obscure part of the Ellerman bombs in Ca II 8542 Å (cf. suggestions in Bruzek 1972, Kitai 1983, Dara et al. 1997, **Paper I**, and Rutten et al. 2013) and this could well explain the prevalence we find for asymmetric Ca II 8542 Å profiles compared to the Hα profiles of the Ellerman bombs we studied. On the other hand, the Hα and Ca II 8542 Å brightenings seem to correspond better when the proper motion of the Ellerman bomb is smaller or when it propagates roughly along the line-of-sight, whereas the overlap is worse when the Ellerman bomb moves at a larger angle to the line-of-sight.

As discussed in Section 1.2.3, magnetic reconnection is the generally accepted driving mechanism behind Ellerman bombs. On morphological grounds, the results from both **Papers I** and **II** would argue for a field configuration as the one suggested for the chromospheric anemone jets, i.e., one leg of an emerging bipole reconnecting with existing field lines. Comparison of the Ellerman bomb locations with the underlying magnetic field as derived from the Fe I 6301 Å Stokes-V maps of the second data set, confirms earlier reports that Ellerman bombs preferentially occur on magnetic inversion lines (cf. e.g., Fang et al. 2006; Pariat et al. 2007; Matsumoto et al. 2008a; Hashimoto et al. 2010) and in agreement with Hashimoto et al. (2010) we also find that one of the polarity patches decreases in intensity, sometimes shrinking to the point that it completely disappears. Simultaneous photospheric surface flow maps indicate that opposite polarity patches are generally driven towards each other, with the flows typically being strongest just prior to the Ellerman bomb eruption.

We confirm earlier reports of Ellerman bomb-visibility in the UV-continua at 1600 Å and 1700 Å, but find that 1600 Å is more prone to contamination from transition region phenomena. Also, even at the higher temporal cadence, still only part of the Ellerman bombs in Hα seem to have counterpart signal in 1700 Å, which agrees with previous studies of possible Ellerman bomb signal in 1600 Å by Qiu et al. (2000) and Georgoulis et al. (2002), but not with the results reported by Berlicki et al. (2010). Nevertheless, we suggest that with stricter constraints (minimum brightness of 8-σ above average and an upper lifetime of 5 min to exclude regular network) 1700 Å might still be used for Ellerman bomb detection, keeping in mind that one may be missing a considerable fraction of the Ellerman bombs that actually go off. Finally, despite numerous reports on the usually sparsely observed Ellerman bomb-related surges in or brightening effects on the upper atmosphere (e.g., Roy 1973; Roy & Leparskas 1973; Shibata et al. 1982; Shimizu et al. 2002; Schmieder et al. 2004; Matsumoto et al. 2008b; Guglielmino et al. 2010; **Paper I**), we find no perceivable signal in the co-aligned He II 304 Å, Fe IX 171 Å

or Fe XIV 211 Å AIA data we analysed.

2.2 Flocculent flows and coronal rain

2.2.1 Flocculent flows in the chromospheric canopy of a sunspot

In **Paper III**, Vissers & Rouppe van der Voort (2012), we analyse the same SST/CRISP data set as in **Paper I**, but investigate an altogether different phenomenon. The field of view contains a small sunspot with a rudimentary penumbra that is connected to the surrounding network patches through superpenumbral fibrils, which are known to host the inverse Evershed effect (Evershed 1909b; see also Section 1.2.2). Spectroscopic measurements of this in- and downflow towards the sunspot have typically yielded values of about 5–10 km s^{-1}, which we confirm from our data. However, in our analysis of Hα wing images we also find high-speed flows located in the superpenumbra, with generally the same sign as the inverse Evershed flow, but they are neither uniform nor continuous; rather, they are intermittent, for which we have termed them "flocculent" [1].

We perform a statistical study of these flocculent flows, extensively employing the CRIsp SPectral EXplorer (see Sect. 1.3) to determine the typical velocities, accelerations, sizes and lifetimes. We find that the discrete, dark "blobs" of which the flocculent flows are composed are small in size (they have an average length and width of 627$\pm$44 km and 304$\pm$30 km, respectively) and typically attain supersonic velocities (ranging between 7.2–82.4 km s^{-1}, but with an average of 36.5$\pm$5.9 km s^{-1}). Their lifetimes are of the order of minutes, ranging between 12–183 s and 67.7$\pm$8.8 s on average, but these are necessarily lower limits as the individual blobs cannot be traced from photospheric footpoint to footpoint.

In addition to sharing some of the properties of the inverse Evershed effect (i.e., both the propagation direction and occurrence location), these statistical properties are reminiscent of a number of transient phenomena observed in the chromosphere and corona that have shortly been discussed before, in Section 1.2.5. Most notably, the flocculent flows resemble coronal rain in morphology, both qualitatively and to a large extent quantitatively, coronal rain having average dimensions of 300 km by 750-900 km (Antolin & Rouppe van der Voort 2012; Antolin et al. 2012, **Paper IV**, see also the next section). Their velocity distributions also overlap, but coronal rain is generally found to propagate at higher absolute velocities. On the other hand, flocculent flows have much faster proper motions than the average velocity derived for the inverse Evershed effect. Even though wave phenomena with a similar morphology have been observed in the chromosphere before (e.g., Sánchez-Andrade Nuño et al. 2008; Wedemeyer-Böhm 2010; Lin et al. 2012), the flocculent flow velocities are also too high to be explained

[1] The adjective *flocculent* refers to the appearance of the flow observed and should not be confused with the already in-use nouns *flocculi* or *flocculae* (terms first coined by Hale & Ellerman 1903). Those refer to the bright plage (Bogod & Gelfreikh 1980) or network as observed in older, lower-resolution data, predominantly in the Ca II H & K lines. They have alternatively been referred to as "bright mottles" (Macris 1962) or "coarse mottles" (Fang et al. 1984).

by acoustic waves, while being too slow to constitute Alfvén waves (i.e., a wave where the magnetic field provides the restoring force).

Considering that flocculent flows appear to constitute footpoint-to-footpoint flows that are supersonic for most of their visible lifetimes, we suggest they probably arise as part of an already present siphon flow in loops that connect the network to the sunspot and other network. The condensations themselves would then result from, e.g., recurring heating events (in analogy to an event recently described from numerical simulations by Zacharias et al. (2011a, 2011b), where cool plasma is ejected from the transition region into the corona) or wave interactions pushing the fibrils out of thermal equilibrium, with the siphon flows subsequently carrying the condensations in a footpoint-to-footpoint motion.

2.2.2 On-disc coronal rain

Paper IV, Antolin et al. (2012), describes a phenomenon that is morphologically similar to flocculent flows, but has its origin in the upper atmosphere: coronal rain (see also Section 1.2.5 for a short introduction on the topic). In all studies prior to the one presented in **Paper IV** only cases of off-limb coronal rain have been analysed and high-resolution reports on the phenomenon are altogether sparse. We therefore expand on the existing studies by analysing coronal rain that is exclusively observed on-disc and perform a statistical study of the phenomenon in five Hα data sets obtained with SST/CRISP (including the ones previously analysed in **Papers I** and **III**) at different viewing angles, ranging between $\mu = 0.25 - 0.67$.

In line with the analyses performed on flocculent flows in **Paper III** and on coronal rain in Antolin & Rouppe van der Voort (2012), we manually trace the coronal rain condensations and extract space-time diagrams along those trajectories using CRISPEX, subsequently determining their dynamics, quantitative morphology and temperatures. We find that in general their properties agree well with those of off-limb cases, although the on-disc condensations have a tendency to move slightly slower, be more elongated and colder. Their total velocities range between 30–120 km s^{-1}(on average 60.7 km s^{-1}) and while with an average of 320 km their widths are comparable to the earlier study by Antolin & Rouppe van der Voort (2012), their average lengths are markedly larger by 140 km, averaging on 880 km. The on-disc coronal rain temperatures are estimated from the width of a Gaussian fit to the background-subtracted spectral profile of the coronal rain blobs, resulting in an average temperature of 7.8×10^3 K (about 2000 K colder than the average for off-limb cases).

However, characterisation of coronal rain is much more complicated on-disc than off-limb. Indeed, the final sample of coronal rain blobs observed in five data sets is only 12% of that observed in only one data set by Antolin & Rouppe van der Voort (2012). This may in part be due to intrinsic differences between the observed active regions, but it is more likely linked to the small sizes and faintness of the blobs, which makes them harder to detect against the bright on-disc background as compared to off-limb observations. Additional effects from the limited spectral window and a relatively long cadence for a majority of the

data sets (i.e., the coronal rain blobs might be moving too fast to be detected) may also contribute to the difference in sample sizes. Also, as hotter coronal rain condensations would be brighter than the colder ones (and thus fainter against the background), this may also explain a selection bias for colder coronal rain events.

Nevertheless, the statistical properties of the observed condensations generally agree well with what has been reported before by Antolin & Rouppe van der Voort (2012). At the same time, they can be sufficiently distinguished from morphologically similar phenomena such as flocculent flows in **Paper III** or the dynamic bright blobs described by Lin et al. (2012). We therefore conclude that coronal rain – which has previously only been observed off-limb – is likely to find its on-disc counterpart in the features we report on in **Paper IV**.

PUBLICATIONS NOT INCLUDED IN THIS THESIS

Refereed publications

- **On-disc Counterparts of Type II Spicules in the Ca II 854.2 nm and Halpha lines**
  L. Rouppe van der Voort, J. Leenaarts, B. De Pontieu, M. Carlsson, and G. Vissers
  The Astrophysical Journal, Volume 705, pp. 272-284 (2009)

- **Coronal Rain as a Marker for Coronal Heating Mechanisms**
  P. Antolin, K. Shibata, and G. Vissers
  The Astrophysical Journal, Volume 716, pp. 154-166 (2010)

Conference proceedings

- **Implications for coronal heating from coronal rain**
  P. Antolin, K. Shibata, M. Carlsson, L. Rouppe van der Voort, G. Vissers, and V. Hansteen
  ASP Conference Series, Volume 454, p. 171 (2012)

- **A sharp look at coronal rain with *Hinode*/SOT and SST/CRISP**
  P. Antolin, M. Carlsson, L. Rouppe van der Voort, E. Verwichte, and G. Vissers
  ASP Conference Series, Volume 455, p. 253 (2012)

- **Ellerman bombs: fallacies, fads, usage**
  R. Rutten, G. Vissers, L. Rouppe van der Voort, P. Sütterlin, and N. Vitas
  Journal of Physics: Conference Series, Volume 440, 012007 (2013)

BIBLIOGRAPHY

Alissandrakis, C. E., Dialetis, D., Mein, P., Schmieder, B., & Simon, G. 1988, A&A, 201, 339

Alissandrakis, C. E., Georgakilas, A. A., & Dialetis, D. 1992, Sol. Phys., 138, 93

Alissandrakis, C. E., Tsiropoula, G., & Mein, P. 1998, in ASP Conf. Ser. 155: Three-Dimensional Structure of Solar Active Regions, ed. C. E. Alissandrakis & B. Schmieder, 49–+

Antolin, P. & Rouppe van der Voort, L. 2012, ApJ, 745, 152

Antolin, P., Shibata, K., & Vissers, G. 2010, ApJ, 716, 154

Antolin, P. & Verwichte, E. 2011, ApJ, 736, 121

Antolin, P., Vissers, G., & Rouppe van der Voort, L. 2012, Sol. Phys., 280, 457

Archontis, V. & Hood, A. W. 2009, A&A, 508, 1469

Aschwanden, M. J. 2001, ApJ, 559, L171

Aschwanden, M. J., Schrijver, C. J., & Alexander, D. 2001, ApJ, 550, 1036

Bahng, J. & Schwarzschild, M. 1961, ApJ, 134, 312

Beckers, J. M. 1962, Australian Journal of Physics, 15, 327

Beckers, J. M. 1968, Sol. Phys., 3, 367

Beckers, J. M. & Schröter, E. H. 1968, Sol. Phys., 4, 303

Beckers, J. M. & Tallant, P. E. 1969, Sol. Phys., 7, 351

Berger, T. E., Rouppe van der Voort, L. H. M., Löfdahl, M. G., et al. 2004, A&A, 428, 613

Berlicki, A., Heinzel, P., & Avrett, E. H. 2010, Mem. Soc. Astron. Italiana, 81, 646

Boerner, P. & Kneer, F. 1992, A&A, 259, 307

Bogod, V. M. & Gelfreikh, G. B. 1980, Sol. Phys., 67, 29

Bones, J. & Maltby, P. 1978, Sol. Phys., 57, 65

Borrero, J. M., Lagg, A., Solanki, S. K., & Collados, M. 2005, A&A, 436, 333

Brandenburg, A. & Subramanian, K. 2005, Phys. Rep., 417, 1

Bray, R. J. & Loughhead, R. E. 1964, Sunspots

Bray, R. J. & Loughhead, R. E. 1974, The solar chromosphere, ed. Bray, R. J. & Loughhead, R. E.

Bray, R. J., Loughhead, R. E., & Durrant, C. J. 1984, The solar granulation (2nd edition)

Bruzek, A. 1972, Sol. Phys., 26, 94

Carlsson, M., Stein, R. F., Nordlund, Å., & Scharmer, G. B. 2004, ApJ, 610, L137

Cattaneo, F., Emonet, T., & Weiss, N. 2003, ApJ, 588, 1183

Cavallini, F. 2006, Sol. Phys., 236, 415

Christopoulou, E. B., Georgakilas, A. A., & Koutchmy, S. 2001, A&A, 375, 617
Dara, H. C., Alissandrakis, C. E., Zachariadis, T. G., & Georgakilas, A. A. 1997, A&A, 322, 653
de Boer, C. R., Kneer, F., & Nesis, A. 1992, A&A, 257, L4
de Groof, A., Bastiaensen, C., Müller, D. A. N., Berghmans, D., & Poedts, S. 2005, A&A, 443, 319
de la Cruz Rodríguez, J., De Pontieu, B., Carlsson, M., & Rouppe van der Voort, L. H. M. 2013, ApJ, 764, L11
de la Cruz Rodríguez, J. & Socas-Navarro, H. 2011, A&A, 527, L8
De Pontieu, B., Carlsson, M., Rouppe van der Voort, L. H. M., et al. 2012, ApJ, 752, L12
De Pontieu, B., Erdélyi, R., & James, S. P. 2004, Nat, 430, 536
De Pontieu, B., Hansteen, V. H., Rouppe van der Voort, L., van Noort, M., & Carlsson, M. 2007a, ApJ, 655, 624
De Pontieu, B., McIntosh, S., Hansteen, V. H., et al. 2007b, PASJ, 59, 655
De Pontieu, B., McIntosh, S. W., Carlsson, M., et al. 2011, Science, 331, 55
de Wijn, A. G., Lites, B. W., Berger, T. E., et al. 2008, ApJ, 684, 1469
Dere, K. P., Schmieder, B., & Alissandrakis, C. E. 1990, A&A, 233, 207
Edlén, B. 1945, MNRAS, 105, 323
Ellerman, F. 1917, ApJ, 46, 298
Engvold, O. & Maltby, P. 1968, in Mass Motions in Solar Flares and Related Phenomena, ed. Y. Oehman, 109
Evershed, J. 1909a, MNRAS, 69, 454
Evershed, J. 1909b, The Observatory, 32, 291
Fang, C., Mouradian, Z., Banos, G., Dumont, S., & Pecker, J. C. 1984, Sol. Phys., 91, 61
Fang, C., Tang, Y. H., Xu, Z., Ding, M. D., & Chen, P. F. 2006, ApJ, 643, 1325
Foukal, P. 1978, ApJ, 223, 1046
Foukal, P. V. 1976, ApJ, 210, 575
Georgoulis, M. K., Rust, D. M., Bernasconi, P. N., & Schmieder, B. 2002, ApJ, 575, 506
Giovanelli, R. G. 1972, Sol. Phys., 27, 71
Grotrian, W. 1934, Zeitschrift für Astrophysik, 8, 124
Guglielmino, S. L., Bellot Rubio, L. R., Zuccarello, F., et al. 2010, ApJ, 724, 1083
Hale, G. E. & Ellerman, F. 1903, Publications of the Yerkes Observatory, 3, 1
Hale, G. E. & Nicholson, S. B. 1925, ApJ, 62, 270
Hansteen, V. H., De Pontieu, B., Rouppe van der Voort, L., van Noort, M., & Carlsson, M. 2006, ApJ, 647, L73
Hart, A. B. 1956, MNRAS, 116, 38
Harvey, K. & Harvey, J. 1973, Sol. Phys., 28, 61
Hashimoto, Y., Kitai, R., Ichimoto, K., et al. 2010, PASJ, 62, 879
Haugen, E. 1969, Sol. Phys., 9, 88
Heggland, L., De Pontieu, B., & Hansteen, V. H. 2007, ApJ, 666, 1277
Heinemann, T., Nordlund, Å., Scharmer, G. B., & Spruit, H. C. 2007, ApJ, 669, 1390

Herlender, M. & Berlicki, A. 2011, Central European Astrophysical Bulletin, 35, 181
Hirzberger, J. & Kneer, F. 2001, A&A, 378, 1078
Isobe, H., Tripathi, D., & Archontis, V. 2007, ApJ, 657, L53
Jurčák, J. & Sobotka, M. 2007, Sol. Phys., 241, 223
Kawaguchi, I. 1970, PASJ, 22, 405
Keller, C. U., Schüssler, M., Vögler, A., & Zakharov, V. 2004, ApJ, 607, L59
Kitai, R. 1983, Sol. Phys., 87, 135
Kitai, R., Watanabe, H., Nakamura, T., et al. 2007, PASJ, 59, 585
Kitchin, C. R. 2003, Astrophysical techniques
Kjeldseth-Moe, O., Brynildsen, N., Brekke, P., Maltby, P., & Brueckner, G. E. 1993, Sol. Phys., 145, 257
Kosugi, T., Matsuzaki, K., Sakao, T., et al. 2007, Sol. Phys., 243, 3
Koval, A. N. & Severny, A. B. 1970, Sol. Phys., 11, 276
Kurokawa, H., Kawaguchi, I., Funakoshi, Y., & Nakai, Y. 1982, Sol. Phys., 79, 77
Langangen, Ø., Carlsson, M., Rouppe van der Voort, L., Hansteen, V., & De Pontieu, B. 2008a, ApJ, 673, 1194
Langangen, Ø., De Pontieu, B., Carlsson, M., et al. 2008b, ApJ, 679, L167
Langangen, Ø., Rouppe van der Voort, L., & Lin, Y. 2008c, ApJ, 673, 1201
Leighton, R. B., Noyes, R. W., & Simon, G. W. 1962, ApJ, 135, 474
Lemen, J. R., Title, A. M., Akin, D. J., et al. 2012, Sol. Phys., 275, 17
Leroy, J.-L. 1972, Sol. Phys., 25, 413
Lin, Y., Engvold, O., & Rouppe van der Voort, L. H. M. 2012, ApJ, 747, 129
Litvinenko, Y. E. 1999, ApJ, 515, 435
Löfdahl, M. G. 2002, in Society of Photo-Optical Instrumentation Engineers (SPIE) Conference Series, Vol. 4792, Society of Photo-Optical Instrumentation Engineers (SPIE) Conference Series, ed. P. J. Bones, M. A. Fiddy, & R. P. Millane, 146–155
Macris, C. J. 1962, Mem. Soc. Astron. Italiana, 33, 85
Maltby, P. 1975, Sol. Phys., 43, 91
Matsumoto, T., Kitai, R., Shibata, K., et al. 2008a, PASJ, 60, 577
Matsumoto, T., Kitai, R., Shibata, K., et al. 2008b, PASJ, 60, 95
Meyer, F. & Schmidt, H. U. 1968, Mitteilungen der Astronomischen Gesellschaft Hamburg, 25, 194
Montesinos, B. & Thomas, J. H. 1997, Nat, 390, 485
Morita, S., Shibata, K., Ueno, S., et al. 2010, PASJ, 62, 901
Müller, D., Dimitoglou, G., Caplins, B., et al. 2009, ArXiv e-prints
Müller, D. A. N., De Groof, A., Hansteen, V. H., & Peter, H. 2005, A&A, 436, 1067
Müller, D. A. N., Hansteen, V. H., & Peter, H. 2003, A&A, 411, 605
Müller, D. A. N., Peter, H., & Hansteen, V. H. 2004, A&A, 424, 289
Muller, R. 1973a, Sol. Phys., 29, 55
Muller, R. 1973b, Sol. Phys., 32, 409
Muller, R. 1983, Sol. Phys., 85, 113
Muller, R. & Mena, B. 1987, Sol. Phys., 112, 295
Nelson, C. J., Doyle, J. G., Erdélyi, R., et al. 2013, Sol. Phys., 21

Nindos, A. & Zirin, H. 1998, Sol. Phys., 182, 381
Nishizuka, N., Nakamura, T., Kawate, T., Singh, K. A. P., & Shibata, K. 2011, ApJ, 731, 43
Nordlund, Å. & Scharmer, G. B. 2010, in Magnetic Coupling between the Interior and Atmosphere of the Sun, ed. S. S. Hasan & R. J. Rutten, 243–254
Nozawa, S., Shibata, K., Matsumoto, R., et al. 1992, ApJS, 78, 267
Ortiz, A., Bellot Rubio, L. R., & Rouppe van der Voort, L. 2010, ApJ, 713, 1282
O'Shea, E., Banerjee, D., & Doyle, J. G. 2007, A&A, 475, L25
Ossendrijver, M. 2003, A&AR, 11, 287
Pariat, E., Aulanier, G., Schmieder, B., et al. 2004, ApJ, 614, 1099
Pariat, E., Schmieder, B., Berlicki, A., et al. 2007, A&A, 473, 279
Parker, E. N. 1957, J. Geophys. Res., 62, 509
Parker, E. N. 1988, ApJ, 330, 474
Parnell, C. E. & Jupp, P. E. 2000, ApJ, 529, 554
Pereira, T. M. D., De Pontieu, B., & Carlsson, M. 2012, ApJ, 759, 18
Qiu, J., Ding, M. D., Wang, H., Denker, C., & Goode, P. R. 2000, ApJ, 544, L157
Rempel, M. 2011, ApJ, 729, 5
Rempel, M., Schüssler, M., Cameron, R. H., & Knölker, M. 2009a, Science, 325, 171
Rempel, M., Schüssler, M., & Knölker, M. 2009b, ApJ, 691, 640
Rimmele, T. & Marino, J. 2006, ApJ, 646, 593
Rimmele, T. R. 1994, A&A, 290, 972
Rouppe van der Voort, L., Bellot Rubio, L. R., & Ortiz, A. 2010, ApJ, 718, L78
Rouppe van der Voort, L., Leenaarts, J., de Pontieu, B., Carlsson, M., & Vissers, G. 2009, ApJ, 705, 272
Rouppe van der Voort, L. H. M. 2003, A&A, 397, 757
Rouppe van der Voort, L. H. M., De Pontieu, B., Hansteen, V. H., Carlsson, M., & van Noort, M. 2007, ApJ, 660, L169
Rouppe van der Voort, L. H. M., Hansteen, V. H., Carlsson, M., et al. 2005, A&A, 435, 327
Rouppe van der Voort, L. H. M., Rutten, R. J., Sütterlin, P., Sloover, P. J., & Krijger, J. M. 2003, A&A, 403, 277
Roy, J. R. 1973, Sol. Phys., 28, 95
Roy, J.-R. & Leparskas, H. 1973, Sol. Phys., 30, 449
Rutten, R. J. 1995, in ESA Special Publication, Vol. 376, Helioseismology, 151
Rutten, R. J., Vissers, G. J. M., Rouppe van der Voort, L. H. M., Sütterlin, P., & Vitas, N. 2013, Journal of Physics Conference Series, 440, 012007
Sánchez-Andrade Nuño, B., Bello González, N., Blanco Rodríguez, J., Kneer, F., & Puschmann, K. G. 2008, A&A, 486, 577
Schad, T. A., Penn, M. J., & Lin, H. 2013, ApJ, 768, 111
Scharmer, G. B., Bjelksjo, K., Korhonen, T. K., Lindberg, B., & Petterson, B. 2003a, in Presented at the Society of Photo-Optical Instrumentation Engineers (SPIE) Conference, Vol. 4853, Society of Photo-Optical Instrumentation Engineers (SPIE) Conference Series, ed. S. L. Keil & S. V. Avakyan, 341–350
Scharmer, G. B., Dettori, P. M., Lofdahl, M. G., & Shand, M. 2003b, in Society of

Photo-Optical Instrumentation Engineers (SPIE) Conference Series, Vol. 4853, Society of Photo-Optical Instrumentation Engineers (SPIE) Conference Series, ed. S. L. Keil & S. V. Avakyan, 370–380
Scharmer, G. B., Gudiksen, B. V., Kiselman, D., Löfdahl, M. G., & Rouppe van der Voort, L. H. M. 2002, Nat, 420, 151
Scharmer, G. B., Henriques, V. M. J., Kiselman, D., & de la Cruz Rodríguez, J. 2011, Science, 333, 316
Scharmer, G. B., Narayan, G., Hillberg, T., et al. 2008, ApJ, 689, L69
Schlichenmaier, R., Jahn, K., & Schmidt, H. U. 1998a, ApJ, 493, L121+
Schlichenmaier, R., Jahn, K., & Schmidt, H. U. 1998b, A&A, 337, 897
Schmieder, B., Rust, D. M., Georgoulis, M. K., Démoulin, P., & Bernasconi, P. N. 2004, ApJ, 601, 530
Schrijver, C. J. 2001, Sol. Phys., 198, 325
Schulz, T. J. 1993, Journal of the Optical Society of America A, 10, 1064
Schüssler, M. & Vögler, A. 2006, ApJ, 641, L73
Sekse, D. H., Rouppe van der Voort, L., & De Pontieu, B. 2012, ApJ, 752, 108
Sekse, D. H., Rouppe van der Voort, L., & De Pontieu, B. 2013a, ApJ, 764, 164
Sekse, D. H., Rouppe van der Voort, L., De Pontieu, B., & Scullion, E. 2013b, ApJ, 769, 44
Severny, A. B. 1956, The Observatory, 76, 241
Severny, A. B. 1968, in Mass Motions in Solar Flares and Related Phenomena, ed. Y. Oehman, 71
Sheeley, Jr., N. R. 1969, Sol. Phys., 9, 347
Shibata, K., Nakamura, T., Matsumoto, T., et al. 2007, Science, 318, 1591
Shibata, K., Nishikawa, T., Kitai, R., & Suematsu, Y. 1982, Sol. Phys., 77, 121
Shimizu, T., Shine, R. A., Title, A. M., Tarbell, T. D., & Frank, Z. 2002, ApJ, 574, 1074
Shine, R., Smith, K., Tarbell, T., Title, A., & Scharmer, G. 1990, in Bulletin of the American Astronomical Society, Vol. 22, Bulletin of the American Astronomical Society, 878
Shine, R. A., Title, A. M., Tarbell, T. D., et al. 1994, ApJ, 430, 413
Sobotka, M., Brandt, P. N., & Simon, G. W. 1999, A&A, 348, 621
Sobotka, M. & Hanslmeier, A. 2005, A&A, 442, 323
Sobotka, M. & Sütterlin, P. 2001, A&A, 380, 714
Socas-Navarro, H., Martínez Pillet, V., Elmore, D., et al. 2006, Sol. Phys., 235, 75
Solanki, S. K. 2003, A&AR, 11, 153
Spiegel, E. A. & Zahn, J.-P. 1992, A&A, 265, 106
Spruit, H. C. 1976, Sol. Phys., 50, 269
Spruit, H. C. 1977, Sol. Phys., 55, 3
Spruit, H. C., Nordlund, A., & Title, A. M. 1990, ARA&A, 28, 263
Spruit, H. C. & Scharmer, G. B. 2006, A&A, 447, 343
St. John, C. E. 1913, ApJ, 37, 322
Sterling, A. C. 2000, Sol. Phys., 196, 79
Stix, M. 2002, The sun: an introduction
Suematsu, Y. 1990, in Lecture Notes in Physics, Berlin Springer Verlag, Vol. 367,

Progress of Seismology of the Sun and Stars, ed. Y. Osaki & H. Shibahashi, 211
Suematsu, Y., Wang, H., & Zirin, H. 1995, ApJ, 450, 411
Sweet, P. A. 1958, in IAU Symposium, Vol. 6, Electromagnetic Phenomena in Cosmical Physics, ed. B. Lehnert, 123
Teriaca, L., Curdt, W., & Solanki, S. K. 2008, A&A, 491, L5
Thomas, J. H. 1988, ApJ, 333, 407
Thomas, J. H. & Weiss, N. O. 2008, Sunspots and Starspots (Cambridge University Press)
Tsiropoula, G., Alissandrakis, C. E., & Mein, P. 2000, A&A, 355, 375
Tsiropoula, G., Alissandrakis, C. E., & Schmieder, B. 1994, A&A, 290, 285
van Kampen, W. C. & Paxman, R. G. 1998, in Society of Photo-Optical Instrumentation Engineers (SPIE) Conference Series, Vol. 3433, Society of Photo-Optical Instrumentation Engineers (SPIE) Conference Series, ed. L. R. Bissonnette, 296–307
van Noort, M., Rouppe van der Voort, L., & Löfdahl, M. G. 2005, Sol. Phys., 228, 191
van Noort, M. J. & Rouppe van der Voort, L. H. M. 2006, ApJ, 648, L67
Vissers, G. & Rouppe van der Voort, L. 2012, ApJ, 750, 22
von der Luehe, O. 1993, A&A, 268, 374
Watanabe, H., Kitai, R., Okamoto, K., et al. 2008, ApJ, 684, 736
Watanabe, H., Vissers, G., Kitai, R., Rouppe van der Voort, L., & Rutten, R. J. 2011, ApJ, 736, 71
Wedemeyer-Böhm, S. 2010, Mem. Soc. Astron. Italiana, 81, 693
Wedemeyer-Böhm, S., Lagg, A., & Nordlund, Å. 2009, Coupling from the Photosphere to the Chromosphere and the Corona, ed. M. J. Thompson, A. Balogh, J. L. Culhane, Å. Nordlund, S. K. Solanki, & J.-P. Zahn, 317
Wedemeyer-Böhm, S. & Rouppe van der Voort, L. 2009, A&A, 507, L9
Wedemeyer-Böhm, S., Scullion, E., Steiner, O., et al. 2012, Nat, 486, 505
Wittmann, A. 1969, Sol. Phys., 7, 366
Yokoyama, T. & Shibata, K. 1995, Nat, 375, 42
Zachariadis, T. G., Alissandrakis, C. E., & Banos, G. 1987, Sol. Phys., 108, 227
Zacharias, P., Peter, H., & Bingert, S. 2011a, A&A, 532, A112+
Zacharias, P., Peter, H., & Bingert, S. 2011b, A&A, 531, A97
Zirin, H. & Stein, A. 1972, ApJ, 178, L85+

Acknowledgements

First and foremost, I would like to thank my supervisor, Luc Rouppe van der Voort, for his guidance and encouragement along the road that has culminated in this thesis. I am very grateful for the opportunities I have had to go observing with the SST at La Palma and the experience(s) I gained in the process, in particular learning the intricacies of ground-based solar observations. I would also like to extend my gratitude to Mats Carlsson, for offering me the USO-SP Marie-Curie Traineeship which brought me to Norway initially and suggesting a PhD to follow up on that afterwards. Of course, I would likely not be where I am now had it not been for Rob Rutten, who introduced me to the realm of solar physics and suggested I come to Oslo in the first place, and Huib Henrichs, who fed my fascination with astrophysics from a younger age. I am deeply grateful to you both. I would also like to thank Patrick Antolin for many fruitful discussions and collaborations; I am sure there are many more yet to come!

Over the past four and half years, I have enjoyed the vibrant and inspiring environment (both academically and socially) at the Institute of Theoretical Astrophysics, in particular thanks to Kosovare Olluri, Thomas Golding, Bhavna Rathore, Viggo Hansteen, Jorrit Leenaarts, Boris Gudiksen, Sven Wedemeyer, Ada Ortiz, Sandro Scodeller, Amir Hammami and of course Nuno Guerreiro (I could hardly forget the most eventful journey to a conference ever). Room 106 has seen many come and go, but has always been a great place to work in, so a big thanks to all past and present office mates. A special thanks goes to Dan Sekse, Torben Leifsen, Eamon Scullion, Håkon Skogsrud, Jaime de la Cruz Rodríguez and Hiroko Watanabe for several memorable observing trips to La Palma, as well as to Pit Sütterlin for great support during observations.

Furthermore, I am grateful to all those that kept me sane outside the confines of the institute, while adjusting to the Scandinavian winters. I want to thank Thomas Strømme and Kristine Konsmo in particular for all the cooking experiments, movie and gaming nights, skiing trips and dinner parties. Equally, I am grateful to Thomas and Hilde Nyløkken, Lars Myking, Brigt Ove Vaage, Kenneth Henriksen and of course all the others over at *Frie Duellister* for many unforgettable moments, both on the mat and outside.

I would like to thank my parents, Reinoud and Dolors, and my sister Saskia for their support and encouragement, even though it had to be from afar. Last, but not least, I would like to thank my girlfriend, my dear Suzanne, for supporting me throughout, especially in the last few stressful months up to thesis submission, and for helping me make the decisions I deep down knew I should.

Part II

Publications

I

Ellerman Bombs at High Resolution. I.
Morphological Evidence for Photospheric Reconnection
H. Watanabe, G. Vissers, R. Kitai, L. Rouppe van der Voort and R. Rutten
The Astrophysical Journal, Volume 736, 71 (2011)

The Astrophysical Journal, 736:71 (12pp), 2011 July 20 doi:10.1088/0004-637X/736/1/71

ELLERMAN BOMBS AT HIGH RESOLUTION. I. MORPHOLOGICAL EVIDENCE FOR PHOTOSPHERIC RECONNECTION

Hiroko Watanabe[1], Gregal Vissers[2], Reizaburo Kitai[1], Luc Rouppe van der Voort[2], and Robert J. Rutten[2,3]
[1] Kwasan and Hida Observatories, Kyoto University, Yamashina-ku, Kyoto 607-8417, Japan; watanabe@kwasan.kyoto-u.ac.jp
[2] Institute of Theoretical Astrophysics, University of Oslo, P.O. Box 1029 Blindern, N-0315 Oslo, Norway
[3] Sterrekundig Instituut, Utrecht University, Postbus 80000, NL-3508 TA, Utrecht, The Netherlands
Received 2011 February 1; accepted 2011 May 2; published 2011 July 6

ABSTRACT

High-resolution imaging-spectroscopy movies of solar active region NOAA 10998 obtained with the Crisp Imaging Spectropolarimeter at the Swedish 1-m Solar Telescope show very bright, rapidly flickering, flame-like features that appear intermittently in the wings of the Balmer Hα line in a region with moat flows and likely some flux emergence. They show up at regular Hα blue-wing bright points that outline the magnetic network, but flare upward with much larger brightness and distinct "jet" morphology seen from aside in the limbward view of these movies. We classify these features as Ellerman bombs and present a morphological study of their appearance at the unprecedented spatial, temporal, and spectral resolution of these observations. The bombs appear along the magnetic network with footpoint extents up to 900 km. They show apparent travel away from the spot along the pre-existing network at speeds of about 1 km s^{-1}. The bombs flare repetitively with much rapid variation at timescales of seconds only, in the form of upward jet-shaped brightness features. These reach heights of 600–1200 km and tend to show blueshifts; some show bi-directional Doppler signature and some seem accompanied with an Hα surge. They are not seen in the core of Hα due to shielding by overlying chromospheric fibrils. The network where they originate has normal properties. The morphology of these jets strongly supports deep-seated photospheric reconnection of emergent or moat-driven magnetic flux with pre-existing strong vertical network fields as the mechanism underlying the Ellerman bomb phenomenon.

Key words: Sun: activity – Sun: atmosphere – Sun: magnetic topology

Online-only material: animations

1. INTRODUCTION

Ellerman bombs are prominent, sudden, short-lived brightness enhancements of the outer wings of strong optical lines, in particular the Balmer Hα line at $\lambda = 6563$ Å, that occur in solar active regions. In his discovery paper, Ellerman (1917, p. 298) described them as "a very brilliant and very narrow band extending four or five angstroms on either side of the [Hα] line, but not crossing it," fading after a few minutes. He named them "solar hydrogen bombs"; nowadays, they are named after him. They occur exclusively in emerging flux regions, are very bright, and have a characteristic elongated shape at sufficient angular resolution.

The fairly extensive literature on Ellerman bombs is reviewed in a parallel paper (R. J. Rutten et al. 2011, in preparation, henceforth Paper I) which also addresses the issue that not all bright features in the wings of Hα are necessarily Ellerman bombs (or "moustaches," another name often taken for the same phenomenon). Small photospheric concentrations of strong magnetic field of the type that constitute network and plage can also produce strikingly bright points in the wings of Hα, the blue wing in particular (Leenaarts et al. 2006a, 2006b). We refer to Paper I for this issue and for a wider overview of the Ellerman bomb literature. The older literature was summarized well in the introduction of Georgoulis et al. (2002). A recent review of small-scale photospheric magnetic fields is given by de Wijn et al. (2009).

Selected recent Ellerman bomb studies of particular relevance here, in addition to the comprehensive study of Georgoulis et al. (2002), are those by Pariat et al. (2004, 2007), Isobe et al. (2007), Watanabe et al. (2008), Matsumoto et al. (2008), Hashimoto et al. (2010), Morita et al. (2010), and Guglielmino et al. (2010). These studies provide evidence that the Ellerman bomb phenomenon occurs at sites of and is due to magnetic reconnection, and characteristically has elongated shapes reminiscent of the "chromospheric anemone jets" of Shibata et al. (2007). The present paper strengthens this case on the basis of Hα observations that are far superior in quality to any in the literature, and establishes that Ellerman bombs of the type seen here are rooted in the deep photosphere. In the remainder of this introduction, we show and discuss a few illustrative examples, and then report more comprehensive measurements in the main body of the paper.

Our observations, described in detail in Section 2, were obtained with the Crisp Imaging Spectropolarimeter (CRISP) at the Swedish 1-m Solar Telescope (SST) on La Palma. The target was an active region with a spot and extended plage where flux was still emerging, seen limbward at viewing angle $\mu = 0.67$. A 37 minute sequence of high-resolution images sampling 23 wavelengths covering Hα was taken at a temporal cadence of 6.2 s between consecutive Hα profile scans.

The observations can be inspected as animations in the online edition of the journal. They show a few dozen eruptive features that are very bright in the Hα wings and appear as rapidly varying extended flames or jets, jutting out from photospheric network, pointing away from disk center. These are clearly Ellerman bombs, seen at unprecedented spatial and temporal resolution. The limbward viewing helps to display their upward extent and fast variations as seen from the side. It also diminishes the network bright point contrast so that the bombs stand out more clearly (cf. Paper I). Figures 1–3 discussed below show cutout snapshots that serve as

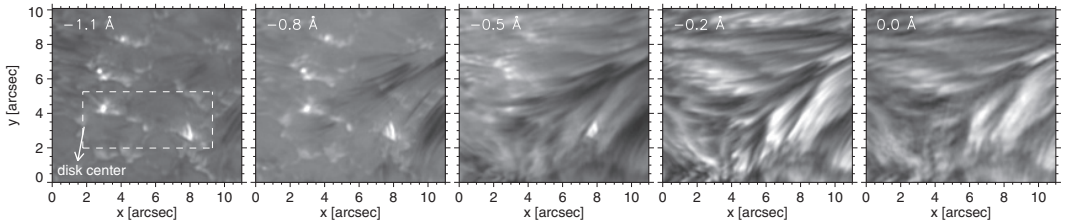

Figure 1. Sample of Ellerman bombs in the small subfield of the CRISP profile scan taken at 08:01 UT outlined in the upper left panel of Figure 4. Clockwise rotation over 120° from (X, Y) was applied to obtain local (x, y) coordinates with the limbward (vertical) direction nearly upward; the direction to disk center is shown in the first panel. The spot lies to the left; nearby plage lies to the right. The five images sample Hα at $\Delta\lambda = -1.1, -0.8, -0.5, -0.2,$ and 0.0 Å from line center. Each panel is gray scaled separately. The dashed white frame in the first panel outlines the yet smaller subfield used in Figure 2. An animation of −1.1, −0.5, and 0.0 Å is available in the online edition of the journal. Full field-of-view animations of −1.1 and 0.0 Å are also available.

(Animations [A, B, C] of this figure is available in the online journal.)

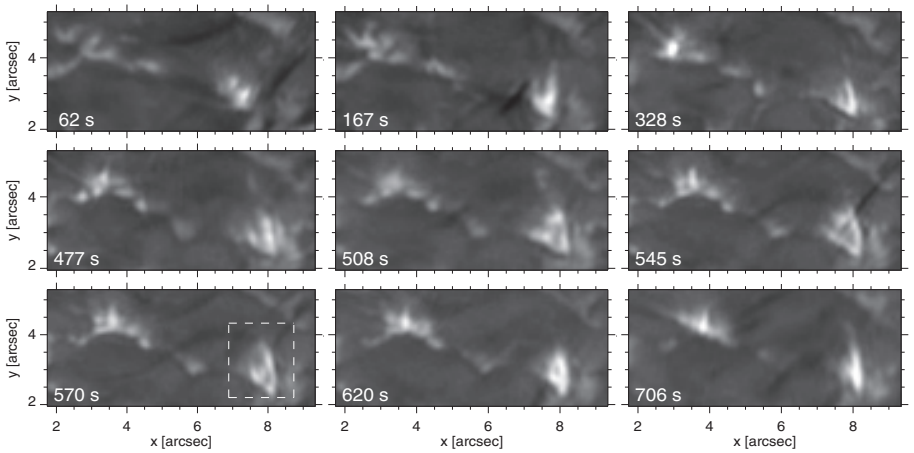

Figure 2. Ellerman bomb evolution in a selection of CRISP image cutouts at $\Delta\lambda = -1.1$ Å from Hα line center. The small subfield shown here is outlined in Figure 1 and contains the most prominent Ellerman bomb (EB-1) at $(x, y) = (8, 3)$. The elapsed time from 07:55 UT is specified in each panel and increases in unequal steps along rows. The $t = 328$ s panel corresponds to the samples in Figures 1, 4, and 5. The dashed white frame specifies the EB-1 cutout shown at 2 s cadence in Figure 3.

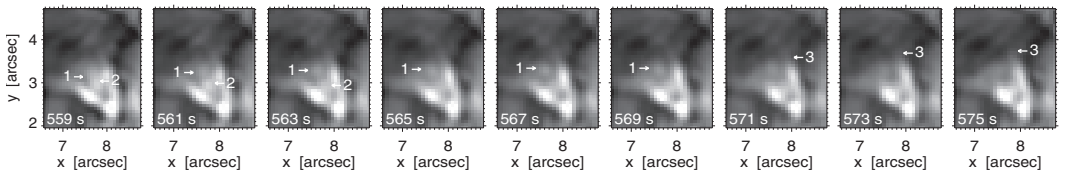

Figure 3. Rapid variations in Ellerman bomb EB-1 in simultaneously taken wide-band images at 2 s cadence. The subfield contains only EB-1. It is outlined in the seventh panel of Figure 2 which is straddled by the brief sequence shown here. The elapsed time specified in the lower left corner of each panel corresponds to that in Figure 2. Upward motion of brightness features is marked comoving arrow 1, downward motion with arrow 2, and extension of an elongated jet structure with arrow 3.

(An animation of this figure is available in the online journal.)

a quick-look emulation of viewing the Ellerman bombs in these animations, but we strongly recommend that the reader inspect the animations.

Ellerman bomb visibility. Figure 1, which samples the deep photosphere, demonstrates, for a small subfield, why Ellerman bombs appear only in the outer wings of Hα, apart from rare Doppler-shifted fibrils (Leenaarts et al. 2006b; Paper I). Closer to line center, they are fully shielded from view by the overlying opaque Hα chromosphere made up of dark fibrils. Note that each panel is gray scaled separately for best contrast; in intensity units, the brightest features at line center are much darker than the Ellerman bombs in the wings, so these do not poke through the fibril canopy even though they extend to heights normally considered chromospheric. Comparing the line-wing and line-center animations in the online material confirms that the line-center fibril evolution is unrelated to the Ellerman bomb activity underneath, except the few Ellerman bombs that are accompanied by an Hα surge.

Ellerman bomb evolution. Figure 2 samples the time evolution of the yet smaller subfield specified in Figure 1. The largest Ellerman bomb is designated EB-1 henceforth. It migrates to the right, along the network away from the spot,

with consecutive flaring-up of adjacent threads that reach a large extent with apparently near-vertical orientation. At some instances, for example at $t = 328$ s, the bright threads have thicker bright feet suggesting small-scale "inverted-Y" (or "Tour d'Eiffel") morphology. The Ellerman bomb site at $(x, y) = (3.5, 4.5)$ shows a similar sequence of smaller thread-like brightenings migrating to the right along the network.

Figure 3 samples even faster variations of EB-1 in frames taken simultaneously with the CRISP sequence but at much higher cadence, with another camera registering Hα with a 4.9 Å wide passband. In order to enhance the contrast of interesting features in the still images, an unsharp masking method similar to the procedure described by Hashimoto et al. (2010), but using a Gaussian filter width of 0.5 arcsec, was employed. The figure demonstrates that small-scale brightness features within EB-1 change and move on timescales of seconds. The apparent speeds are measured in Section 4 and are supersonic.

Ellerman bomb properties. Viewing the animations establishes a number of key properties of the Ellerman bombs in these data as follows.

1. These Ellerman bombs are all rooted in intergranular lanes in the deep photosphere.
2. They all have upward protrusions that we generically call "jets" here, often appearing in the form of nearly parallel or consecutive slender bright threads.
3. They all point away from disk center in the limbward field of view, and so appear to be more or less vertically oriented. None seems to sense the more horizontal orientation of the overlying chromospheric fibrils that are observed at the center of Hα.
4. The Ellerman bombs migrate, while flaring repetitively, along the pre-existing network, always away from the spot.
5. There are very fast variations in their fine structure during the repetitive flaring.
6. Some of the brighter threads display small-scale inverted-Y morphology.
7. Some Ellerman bombs are accompanied by dark Hα surges.

Together, these properties define the Ellerman bombs in this data set as photospheric events rooted in the network that produce eruptive jets reaching upward to considerable height, with fast temporal variations that suggest successive interaction of the newly arriving vertical field with the existing network field, most likely in the form of magnetic reconnection. Photospheric reconnection has been suggested theoretically (cf. Shibata et al. 1982; Yokoyama & Shibata 1995; Litvinenko 1999) but has not been established observationally. The present observations provide the clearest evidence to date.

In the rest of the paper, we detail the observations (Section 2) and the methods used for the selection and measurements of Ellerman bombs and other bright points (Section 3). In Section 4, we quantify the observed Ellerman bomb footpoint motions, extensions and retractions, their Doppler signatures, and their fast variations. We also compare Ellerman bomb properties with those of non-eruptive network bright points and display one of the two cases with a surge. We discuss the Ellerman bomb phenomenon in Section 5, including a brief comparison with previous studies, and conclude the paper in Section 6.

2. OBSERVATIONS AND DATA REDUCTION

Instrumentation. The data for this study were obtained with the CRISP (Scharmer et al. 2008) at the SST (Scharmer et al. 2003a) on La Palma. CRISP is a dual Fabry–Pérot interferometer allowing wavelength tuning within 50 ms. Its combination with the unprecedented angular resolution and image sequence quality attained by the SST's superb optics and site combined with sophisticated wavefront restoration yields data of outstanding spatial, temporal, and spectral resolution (e.g., Rouppe van der Voort et al. 2009; Ortiz et al. 2010). The SST real-time tip-tilt correction and adaptive-optics wavefront correction are described by Scharmer et al. (2003b). The post-detection numerical image restoration is described by van Noort et al. (2005).

Observations. The setup of CRISP starts with an optical chopper synchronizing the exposures by multiple cameras. A filterwheel contains appropriate prefilters; in this case, one was used that selects Hα with a passband of FWHM = 4.9 Å. A few percent of the light is branched off to a camera taking images in this wide band. These serve usually only for "multi-object" seeing monitoring in the numerical post-processing, but in this study they were also analyzed because of their fast cadence. The bulk of the light passes through two liquid crystals and a high-resolution and a low-resolution Fabry–Pérot etalon, and is then divided by a polarizing beam splitter between two cameras. The three CCD cameras are high-speed, low-noise Sarnov CAM1M100 ones with 1 K × 1 K chips. They ran synchronously at 35 frames per second with an exposure time of 17 ms. The image scale was 0.071 arcsec pixel^{-1}, well sampling the SST's Rayleigh diffraction limit of 0.17 arcsec at Hα. The field of view covered 67 × 67 arcsec^2. The CRISP transmission profile has FWHM = 6.6 pm at Hα.

An Hα sequence was acquired between 07:55 and 08:33 UT on 2008 June 11 during good to excellent seeing conditions. The target was AR 10998, containing a leading sunspot with a rudimentary penumbra and following plages. The sunspot appeared on 2008 June 8, kept growing until June 11, and had fully disintegrated by June 15. In these June 11 data, the region was located at viewing angle $\mu = 0.67$ toward the east limb. The field of view was centered on $(X, Y) \approx (-684, -152)$ with (X, Y) the standard solar coordinates in arcsec from apparent disk center with Y positive along the solar meridian toward the north pole, X positive westward.

The Hα profile was sequentially sampled at 23 wavelengths within the line, ranging between ±1.1 Å with respect to line center with 0.1 Å spacing. At each tuning position, a "multi-frame" burst of eight exposures was taken. The cadence between consecutive line scans was 6.2 s.

Another observing program was run before and after the Hα observations, targeting the same area but sampling the magnetically sensitive Fe I 6302 Å lines. It ran during 07:15–07:32 UT and 09:26–10:26 UT. The first run had CRISP sampling both the 6301.5 Å and 6302.5 Å lines as well as a continuum wavelength, at a scan cadence of 41 s. The later run sampled only the 6302.5 Å line plus a continuum wavelength at a scan cadence of 16 s. Simple Stokes-V/I magnetograms were constructed from the flat-fielded images at $\Delta\lambda = -48$ mÅ from line center, selected for high Stokes-V signal and large contrast, for inspection of the magnetic context prior to and after the Hα observations. One such magnetogram is shown in Figure 4.

Reduction. The post-processing to achieve further image restoration including precise co-alignment was done with the Multi-Object Multi-Frame Blind Deconvolution (MOMFBD) algorithm of van Noort et al. (2005). It includes tessellation of all images (i.e., at each tuning position within a line scan) into 64 × 64 pixel^2 subfields for individual restoration. The wide-

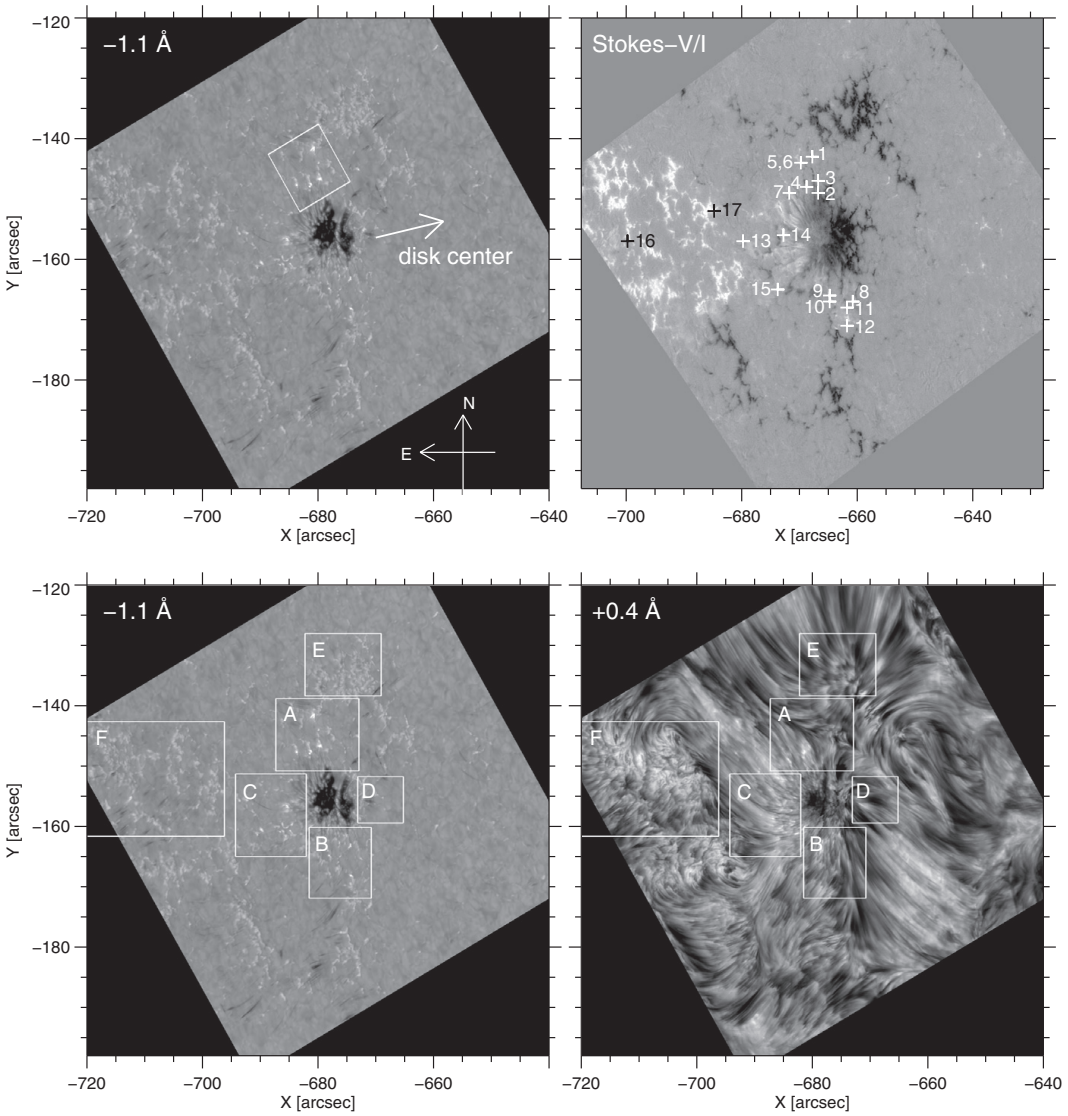

Figure 4. CRISP image samples for the full field of view. The standard solar (X, Y) coordinates have the origin at apparent disk center and the Y direction toward the solar poles with northward positive and the X direction with westward positive. The center of the field of view has viewing angle $\mu = 0.67$ toward the east limb; the direction toward disk center is indicated in the first panel. The field of view includes AR 10998. Upper left panel: H$\alpha-1.1$ Å blue-wing image taken at 08:01 UT. The white frame specifies the subfield that is shown in Figure 1 with clockwise rotation over 120°. The brightest feature in this subfield is Ellerman bomb EB-1, shown in detail in Figures 2 and 3. Upper right panel: a CRISP Fe I 6302 Å Stokes-V/I magnetogram taken two hours later, with corresponding shift in X due to solar rotation. The numbered plus signs define the locations of the 17 Ellerman bombs measured in Section 3. Lower left panel: the same H$\alpha-1.1$ Å blue-wing image overlaid with frames specifying the subregions selected for bright-point measurements in Section 3. Lower right panel: simultaneous H$\alpha+0.4$ Å image overlaid with the same subregion frames.

band data served both as multi-object representation and as an anchor for alignment of the narrow-band bursts per sequence. In this case the wide-band frames were also processed separately from the CRISP data to obtain a simultaneous sequence at a cadence of only 1 s, which serves below to analyze fast temporal evolution within Ellerman bomb EB-1 (Figure 3). More detail on MOMFBD reconstruction strategies for such data sets is given in van Noort & Rouppe van der Voort (2008).

Subsequently, the restored images were subjected to prefilter correction removing the transmission profile of the wide-band filter, to derotation which removes the time-varying image rotation that results from the alt-azimuth configuration of the

SST, and to destretching which removes remaining rubber-sheet distortions (small-scale translations and warping) by seeing. These are determined following Shine et al. (1994) through cross-correlation of running means over a few minutes of small subfields of the wide-band sequence and they are then applied to the narrow-band images.

Figure 4 shows two full-field samples, for the outer blue wing at $\Delta\lambda = -1.1$ Å from line center in the left-hand column and for the inner red wing at $\Delta\lambda = +0.4$ Å from line center in the lower right panel, respectively. Both are from the CRISP scan at 08:01 UT, a moment of very good seeing that yielded the largest image contrast of the 37 minute sequence. The upper right panel contains a corresponding magnetogram from the Fe I 6302 Å data taken two hours later. The various figure annotations are described below.

3. FEATURE SELECTION AND MEASUREMENT

3.1. Ellerman Bombs

Occurrence in the field of view. Inspection of the various Hα-wing animations shows the occurrence of many Ellerman bombs near the spot, in particular to the east where there was an extended plage of opposite polarity (upper panels of Figure 4). Note that the penumbra shows black-and-white bipolar difference between the east and west sides of the spot, but this results from the combination of slanted viewing and near-horizontal penumbral field configuration. The plage fields are primarily vertical; their black/white signature in the magnetogram in Figure 4 indeed specifies opposite polarity. Most Ellerman bombs appear fairly close to the spot.

Spectral variations. Figures 1 and 5 illustrate the spectral behavior of Hα over the target area. Figure 1 samples the small subfield outlined in Figure 4 at five wavelengths in the blue Hα wing. The wing images ($\Delta\lambda = -1.1$ Å, -0.8 Å) show a grayish background with somewhat brighter network. The photospheric contribution to this part of Hα originates in the deep photosphere, but in the blue wing the granular contrast is flattened as explained by Leenaarts et al. (2006b). The network contrast diminishes toward the limb, as explained in Paper I. The Ellerman bombs appear very bright. Figure 5, which samples Hα profiles for different pixel categories, shows that in Ellerman bombs the Hα wings reach nearly twice the intensity they have in quiet-Sun areas and extend well beyond our $\Delta\lambda = \pm 1.1$ Å sampling range—in accordance with Ellerman's (1917) remark that they extend 4–5 Å on either side.

At line center, all Ellerman bombs are hidden by overlapping chromospheric fibrils (or "mottles"; we use the term fibril generically for long slender filamentary structures). The second panel of Figure 1 shows the onset of this obscuration. At $\Delta\lambda = -0.8$ Å, only a few dark fibrils appear, as was also the case in the observations of Leenaarts et al. (2006b) at the same wavelength. These isolated dark fibrils are mostly chromospheric absorption features with large blueshift, probably the "Rapid Blue Excursions" that Rouppe van der Voort et al. (2009) identified as the on-disk counterpart of so-called spicules-II seen at the solar limb. Closer to line center, the chromospheric fibrils gain opacity and together form an opaque blanket obscuring any photospheric contribution underneath, including the upright jets of the Ellerman bombs. At $\Delta\lambda = -0.5$ Å, all brightest areas in Figure 1 still correspond to the underlying Ellerman bombs, although not 1:1 in shape, but at $\Delta\lambda = -0.2$ Å this is no longer true. Even the tallest Ellerman bomb in Figure 1, EB-1, is obscured at line center.

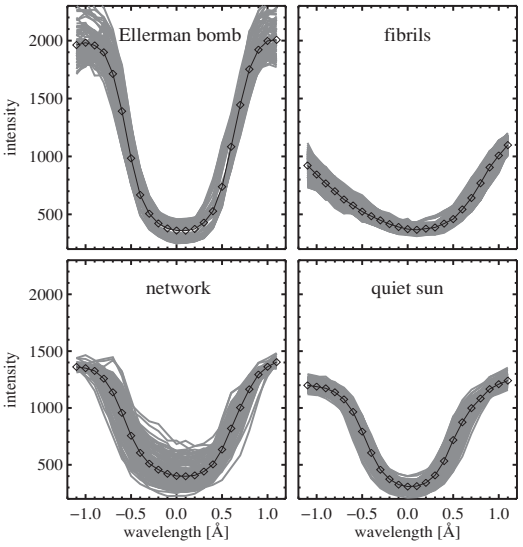

Figure 5. Characteristic Hα profiles collected from the CRISP scan taken at 08:01 UT. Each panel contains a number of per-pixel profiles for a specific pixel category. The solid curve is their mean, with the CRISP sampling wavelengths marked. The intensity scale (in arbitrary data units) is the same for the different categories. The samples were selected by first obtaining the average wing brightness $\langle I_{\rm wing}\rangle$ per pixel by summing the blue- and red-wing values at $\Delta\lambda = -1.1, -1.0, -0.9, +0.9, +1.0, +1.1$ Å. Clockwise from top left: Ellerman bombs, all 84 pixels with $\langle I_{\rm wing}\rangle > 1800$; fibrils, 314 pixels with $\langle I_{\rm wing}\rangle < 950$ in the eastern part of the field of view; quiet Sun, 250 pixels covering a small area in the region around $(X, Y) = (-665, -170)$ in Figure 4; network without Ellerman bombs, all 169 pixels with $1349 < \langle I_{\rm wing}\rangle < 1350$. Note that at the $\Delta\lambda = \pm 1.1$ Å sampling extremes the mean profile reaches only about 70% of the continuum intensity for a quiet-Sun average.

Correspondingly, the Hα cores in Figure 5 are as dark for the Ellerman bomb locations as they are for dark fibrils that are selected as such on the basis of dark outer wings. Obviously, the fibril obscuration determines this part of the Ellerman bomb profiles. Since Ellerman bombs always occur in emerging flux regions that necessarily possess rich fibril structure in the overlying Hα chromosphere, obscuration-free Ellerman bomb observation at Hα line center may inherently be impossible.

Selection. The animations suggest that the Ellerman bombs are relatively long-lived brightness entities, appearing repetitively while their feet migrate along the network. We decided to use the outer Hα wings as a measurement diagnostic by defining their sum and difference as $I_{\rm sum} \equiv (I_r + I_b)/2$ and $I_{\rm diff} \equiv (I_r - I_b)/(I_r + I_b)$, with I_b the spectrally averaged blue-wing intensity at $\Delta\lambda = -1.1, -1.0$, and -0.9 Å from line center and, likewise, I_r the averaged red-wing intensity at $\Delta\lambda = +1.1, +1.0$, and $+0.9$ Å from line center. The outer-wing averaging reduces noise from seeing variations. The wing summing and differencing removes, to first order, the effect of Dopplershift on $I_{\rm sum}$ and the effect of intensity change on $I_{\rm diff}$. We treat the wing difference as a Doppler signal below. This is a better choice for Ellerman bombs than measuring the profile-minimum shift or core bisector shift, which are set by the overlying fibrils. For emission features such as Ellerman bombs, positive $I_{\rm diff}$ implies redshift. Since the Ellerman bombs appear to extend upright, the measured redshifts imply downflows at the $\mu = 0.67$ viewing angle.

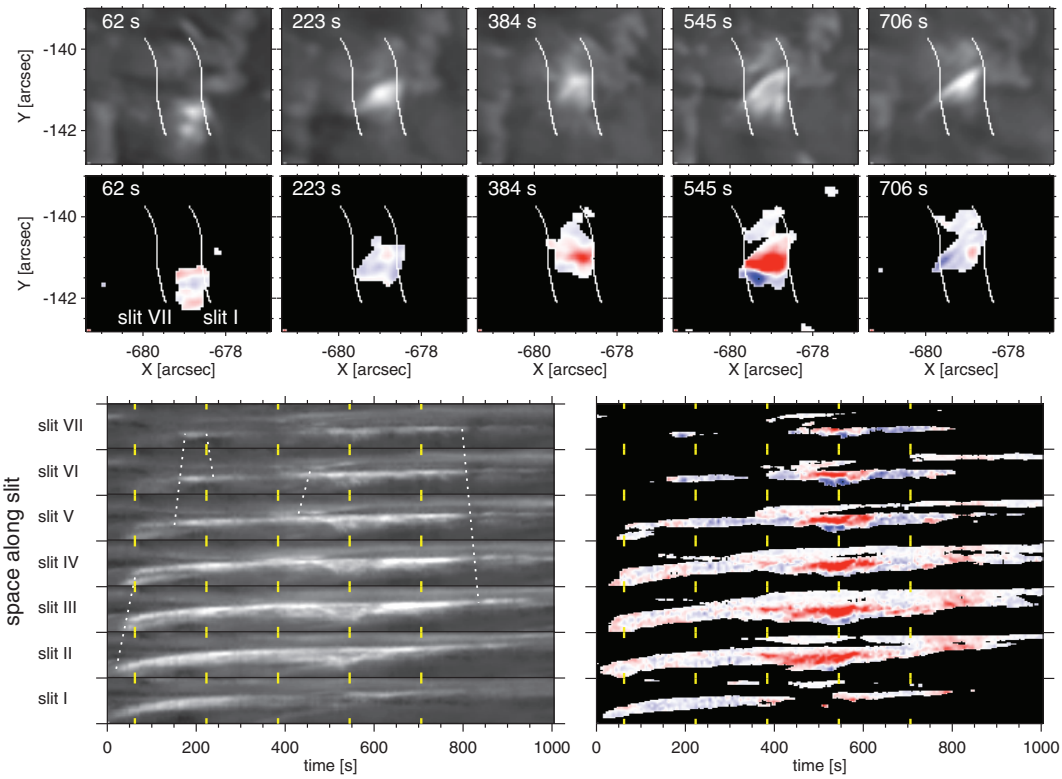

Figure 6. Upper part: wing-brightness sum (upper row) and difference ("Dopplergrams," lower row) images for Ellerman bomb EB-1. The wing-Dopplergram images are blue for apparent blueshift, red for redshift, and are thresholded at high wing-brightness intensity to avoid contamination with the Dopplershift signals of overlying dark fibrils. The numbers in each panel specify the elapsed time from the first appearance at 07:55 UT, as in Figure 2. The (X, Y) coordinates correspond to Figure 4; the limb is leftward. The two white curves specify the extremes of seven equidistant adjacent sampling "slits" with width 1 pixel. Slit I is set manually to track the footpoint location with time; the others are set parallel to that at intervals of 128 km in the limbward (vertical) direction. Lower part: corresponding multi-slit space–time evolution diagrams for EB-1, with the elapsed time from the first appearance plotted horizontally and the length along each sampling slit plotted vertically, respectively, for the wing-brightness sum (left) and difference (right). The yellow ticks are indicators of times of snapshots shown in the upper two rows, i.e., 62 s, 223 s, 384 s, 545 s, and 706 s. The dotted white lines in the first diagram illustrate ascents and descents of jet brightness features. For example, the longest dotted line at $t = 800$–840 s describes contraction of the jet measured as descent of a bright feature at its top. The Dopplershift coding in the right-hand diagram indicates a bi-directional jet with upward motion (blueshift) of its upper part and downward motion (redshift) of its lower part during $t = 500$–750 s.

(An animation of this figure is available in the online journal.)

We constructed $I_{\rm sum}$ wing-brightness and $I_{\rm diff}$ wing-Dopplergram images for the whole data sequence. We used the $I_{\rm sum}$ sequence to identify and select Ellerman bombs manually, using excess wing brightness, presence of a jet-like protrusion, and visibility above 240 s duration as criteria. Thus we selected 17 Ellerman bombs whose positions are indicated in the second panel of Figure 4. The first 15 lie in the periphery of the spot or the moat around it (recognizable from the outward moat flow across it in the animations). EB-16 and EB-17 lie at the edge of a plage. Overall, these Ellerman bombs seem to be located preferentially at the network and moat boundaries. We found no Ellerman bombs at the more quiescent west side of the spot.

Space–time slit diagrams. We have constructed what we call "multi-slit space–time diagrams" for all 17 Ellerman bombs to facilitate quantitative measurement of their apparent footpoint proper motion, the extension and retraction speeds of their jet-like protrusions, and the sign and magnitude of their Doppler signals. These measurements are non-trivial due to the motion that the Ellerman bombs display along the network while flaring up in a succession of jet-like or thread-like protrusions. Figure 6 shows such a diagram for EB-1.

The measurement procedure is as follows. First, the approximate jet direction (N, NE, E,. . .) is determined by eye. Second, a baseline spatial "slit" (called slit I) of 1 pixel width is defined manually such that it contains the bottom edge, or footpoint, of the protrusion and tracks its subsequent locations; this track is generally not straight. Third, six more slits II–VII are positioned by spacing them parallel to slit I, sharing the same bends, at every 128 km in the approximate jet direction. Slit VII is then the furthest from the footpoint, at 768 km from slit I. Together, these slits represent samplings of the jet along its apparent height that track its footpoint path. They enable the construction of space–time plots for the wing brightness $I_{\rm sum}$ and wing Dopplershift $I_{\rm diff}$. In the latter, we found it necessary to mask off all areas that have wing brightness below 1400

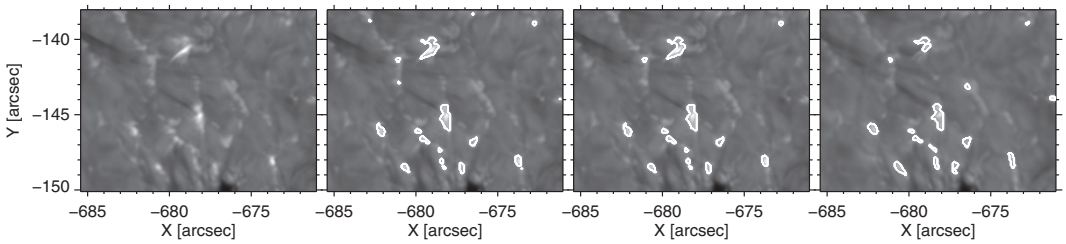

Figure 7. Automatic detection of network bright points using the wing-brightness images. First panel: Region A at 08:08 UT. The (X, Y) coordinates correspond to Figure 4. Second panel: areas over 3σ brighter than the average values are outlined with white contours. Third panel: result after removal of small bright points. Fourth panel: a similar map one minute later, illustrating good continuity.

Table 1
Ellerman Bomb Properties

EB	Jet Direction	Lifetime (s)	Footpoint Extent[a] (km)	Jet Extent[a,b] (km)	Footpoint Speed (km s^{-1})	Extension Speed[b] (km s^{-1})	Retraction Speed[b] (km s^{-1})	Blue/Red Signal at J:jet, F:footpoint
1	SE	1004	820	1180	1.23	5.5–9.8	5.9	J:blue, F:red
2	E	508	360	770	1.15	6.2	9.8	no
3	E	1302	390	690	1.13	6.2	5.6	J:blue
4	E	713	460	770	1.00	7.6	...	J:blue
5	E	260	280	1230	no	5.7	4.6–6.4	J:blue, F:red
6	E	266	280	1120	no	11.0	8.7	J:blue, F:red
7	E	359	490	870	1.60	6.4–8.3	6.9	J:red, F:blue
8	E	682	310	750	1.31	3.8–4.2	10.4	F: blue, then red
9	E	322	620	540	1.11	23.7	...	J:blue
10	E	651	510	850	1.44	7.2–8.3	11.9	J:blue, F:blue
11	E	428	690	670	0.85	18.5	...	J:red
12	NE	459	330	1050	0.29	...	8.5–15.1	F,J: red, then blue
13	N	279	900	720	no	6.4–11.9	6.4	J:blue, F:red
14	E	868	440	950	0.27	2.8–3.5	9.2	J:red, F:blue
15	E	589	410	800	no	2.9	...	no
16	SE	614	410	930	no	6.4–11.9	11.9	J: red, then blue
17	E	322	310	640	no	6.2	...	J:red, F:blue
Average	E	566	471	855	0.67	8.0	8.7	...[c]

Notes.
[a] The apparent footpoint measured on best-seeing images.
[b] If a jet is vertical, which they are roughly, the actual lengths and velocities are a factor of 1.5 larger.
[c] Too much spread to give a meaningful average.

(in the arbitrary data units also used in Figure 5) because otherwise, overlying chromospheric fibrils dominate the Doppler signature with their independent Dopplershifts. In addition, for these dark features the Dopplergram definition switches sign, causing extra confusion, as does their varying viewing angle with respect to the line of sight. By masking the dark fibrils off, the space–time Doppler signature is much better constrained to display Ellerman bomb properties only. Finally, using these multi-slit space–time diagrams we derived the proper-motion speed of all Ellerman bomb feet, the extension and retraction speeds of all jets, and the spatial occurrence distributions along all Ellerman bombs of their Doppler signatures. The results are given in Section 4 and Table 1.

3.2. Network Bright Points

In order to compare the characteristics between Ellerman bombs and normal network bright points (henceforth NBP), we also analyzed the latter in our data sequence. Like the Ellerman bombs, the NBPs are not distributed uniformly within the field of view but occur preferentially to the east of the spot (Figure 4). In order to compare NBP properties between different types of region, six subregions named A–F were chosen that are identified in the lower panels of Figure 4. Regions A, B, and C sample the moat flow around the spot on its north, east, and south sides. Region C contains the well-developed part of the penumbra, whereas Region D samples the penumbra-free west side of the spot. Region E samples the same-polarity plage to the north of the spot, whereas Region F samples the opposite-polarity plage to the east of the spot.

We applied a brightness threshold algorithm to identify NBPs for statistical analysis using the wing-brightness images. A similar algorithm was developed for the detection of umbral dots in Watanabe et al. (2009). Note that Ellerman bombs are also NBPs when categorized per brightness threshold, but the Ellerman bombs defined and selected above possess eruptive jets as well. The procedure consists of four steps illustrated in Figure 7.

1. *Identify NBPs in each image.* NBPs are defined as areas whose wing-sum brightness ($I_{\rm sum}$) is over 3σ brighter than the average of the pertinent subregion, with σ the standard deviation. For plage regions a threshold of 5σ is used instead. The latter selects only a few NBPs in plage that usually lie at the plage periphery. A lower threshold would select much of the plage as NBP, without individual

properties or measurable morphology. We then defined the position of each NBP as the peak location within the thresholded area.

2. *Remove too small NBPs.* Too small NBPs covering less than 5 pixels (0.18 arcsec in radius) are removed. Note that the diffraction limit is 0.17 arcsec.
3. *Track NBPs.* An NBP at a subsequent time step is considered to mark the continued manifestation of a prior NBP if they have spatial overlap. We accepted the cases in which such continuation skipped one or two time steps. When there is no overlap within three successive time steps, the NBP is considered to have disappeared.
4. *Remove the merging/splitting events.* The procedures described above include some merging or splitting events. We remove these events by selecting the longest-duration event and separate it from merging/splitting pieces. Thus, one of two merging or splitting pieces is kept for tracking while the other ends or starts at this time step.

For example in Region A, a total of 183 NBPs were detected in this manner. Seven of these were also selected as Ellerman bombs in Section 3.1.

4. RESULTS

4.1. Ellerman Bomb Properties

Our measurements of the 17 selected Ellerman bombs are given in Table 1. Their footpoints travel lengths along the network and their jet extents were measured on best-seeing images. The resulting jet extents and the jet extension and retraction speeds are apparent lengths and velocities. If the jets are vertical, which they roughly seem to be, the real values are larger by a factor $1/\mu = 1.5$. The mean apparent jet extent is close to 1 Mm, so the jets stick out well above the photosphere. The mean lifetime is about 10 minutes.

Footpoint motion. The wing-brightness distribution across slit II in the space–time diagrams such as the one for EB-1 in Figure 6 was used for the measurement of footpoint proper motion because this slit usually contains the brightest part of the bright point at the foot of an Ellerman bomb. When there is proper motion, the space–time diagram shows an inclined bright lane, as is the case in Figure 6. The inclination was then measured and converted into apparent speed. The direction of motion is always radially away from the spot. The average speed of footpoint motion of Ellerman bombs is 0.67 km s^{-1}.

Extension and retraction speed. We identified apparent jet extensions or retractions using the wing-brightness panels of the multi-slit space–time diagrams together with the corresponding movie. Some examples are marked in Figure 6 with white dotted lines. Their slope gives the extension/retraction speed by dividing the pertinent slit separation in units of their 128 km spacing by the travel time. The typical value is 5–10 km s^{-1}, without systematic difference between the extension and retraction speeds. Of course, the actual gas speed depends on the projection; for vertical jets, the measured apparent speeds should be multiplied by $1/\mu = 1.5$.

Dopplershift. We found interesting Dopplershift signatures in the wing-Dopplergram space–time charts in 15 cases out of 17 Ellerman bombs. EB-1 in Figure 6 starts with subtle blueshift and later displays simultaneous redshift at the footpoint NBP and blueshift near the jet top during 500 s–750 s. Three more cases show such combination of footpoint redshift with jet blueshift. The pattern suggests the presence of a bi-directional jet, with downflow at its bottom and upflow at its top. The blueshifts tend to last longer than the redshifts. In three cases we found the opposite pattern: downflow at the top and upflow at the bottom. Sometimes an Ellerman bomb alternates between the two patterns during its lifetime. In the two cases where the jet is clearly accompanied by a surge (EB-8 and EB-12, discussed below), the latter's Dopplershift obscures the underlying Ellerman bomb motion. In two cases (EB-2 and EB-15), we could not find Ellerman bomb associated Dopplershifts, probably due to interweaving upflow and downflow components or seeing perturbation.

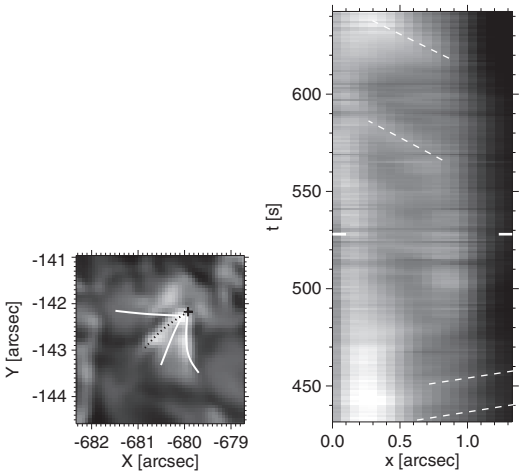

Figure 8. Left: measurement tracks through Ellerman bomb EB-1 in the wide-band data at 08:04 UT. The (X, Y) coordinates correspond to Figure 4. Right: time–space diagram along the black dotted track in the left-hand image, with the elapsed time from the first appearance plotted vertically. The 0 arcsec location is indicated in the right panel with a black plus sign. The slanted dotted lines specify apparent-speed estimations, while the white tick marks at $t \approx 530$ s indicate the time step at which sample data are shown in the right panel.

Fast variations. Figure 3 and the wide-band movie in the online material demonstrate that, at the 1 s cadence of the wide-band image sequence, very fast variations are observed. As residual high-frequency seeing effects might contaminate the sample of real fast variations, a low-pass filter with a cutoff of 50 km s^{-1} was applied to the wide-band data. In addition, only those variations that were visible in more than one subsequent frame were considered for the analysis described below, while residual seeing effects are typically only visible for one frame and furthermore random in nature.

A more detailed analysis of the fast variations was performed for EB-1. First, the cutout subfield frames were cross-correlated to remove EB-1's proper motion. Time–space diagrams were then extracted along paths that track in time either the jet top or single bright features inside the Ellerman bomb. The left-hand panel of Figure 8 shows the selected paths overlaid on a good quality EB-1 image. The right-hand panel shows part of the time–space diagram along the dashed path. The timeslices enable measurement of the apparent proper-motion speed for particular features that move along these paths, as well as the jet extension and retraction speed. Four such measurements have been overlaid as dashed lines in the right panel in Figure 8 to illustrate the procedure. The upper two concern downdraft features, both with an apparent speed around 18 km s^{-1},

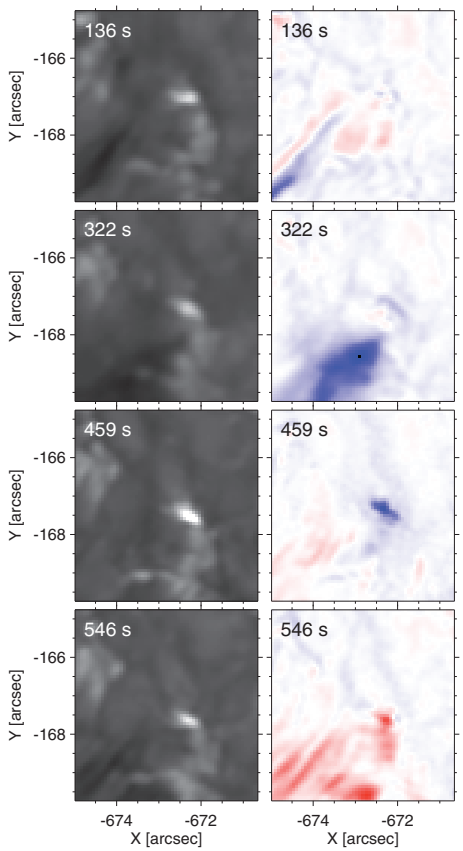

Figure 9. Temporal evolution of Ellerman bomb EB-8 in wing-brightness (left) and wing-Dopplergram images (right). The numbers in each panel specify the elapsed time from its first appearance. The (X, Y) coordinates correspond to Figure 4. The limb is to the left. This Ellerman bomb seems to initiate a dark extension to its southeast (lower left direction), with alternating Dopplershift signature (where blue color implies downflow for the absorption feature.)

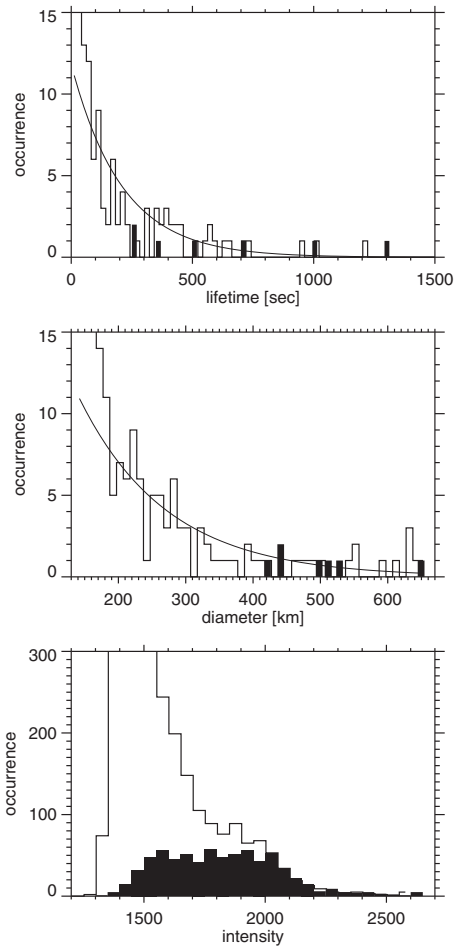

Figure 10. Histograms of bright-point lifetime, diameter, and brightness in Region A. The seven Ellerman bombs found in this region are entered as black bins. The curves in the upper two panels are fits with exponential decay functions $y = \text{const.} \times \exp(-x/C)$.

whereas the lower two are updrafts, with apparent speeds close to 59 km s^{-1}.

In this manner 11 displacement speed measurements were obtained for EB-1. The typical timescale for jet-like features to extend/retract is 25–40 s, but isolated brightness features can exist on timescales of 2–7 s. Six out of 11 cases display updrafts and the rest display downdrafts. The apparent updraft speeds range between 11 and 60 km s^{-1} with the majority at the higher values, while the apparent downdraft speed range between 7 and 18 km s^{-1}.

Surges. Figure 9 shows the case of EB-8 which displays special temporal evolution. First, the Ellerman bomb appears and seems to initiate surge activation on its southeast side. This surge appears repetitively during the observations, with alternating negative and positive $I_{\rm diff}$. Note that, since the surge is observed as an absorption feature in Hα, the Dopplershift sign is reversed with respect to the Ellerman bomb which is observed in emission, so that for the surge, positive wing difference $I_{\rm diff}$ implies upflow along the line of sight, i.e., blueshift although it is color-coded red in Figure 9. The surge exhibits strong positive $I_{\rm diff}$ corresponding to an upflow of $\approx$40 km s^{-1}(measured from the Hα line-center Doppler shift) at around 322 s after the appearance of EB-8. About 1 minute after the surge disappears, negative $I_{\rm diff}$ (downflow) appeared at the position of the Ellerman bomb, and 1 minute after that positive $I_{\rm diff}$ (upflow) replaced the negative $I_{\rm diff}$. Simultaneously, the surge location was also dominated by redshift.

EB-12 is similarly adjacent to an Hα surge on its south side, which also shows alternating positive and negative $I_{\rm diff}$.

4.2. Ellerman Bombs versus Normal NBPs

Figure 10 shows histograms of the lifetime, diameter, and wing brightness of NBPs in Region A. The seven NBPs that are also Ellerman bombs are entered as black bins. The diameter is calculated by assuming circular shape, converting its area into the corresponding circle diameter, and taking the average over

Table 2
NBP Properties

Region	Total Number of NBPs Detected	Characteristic Lifetime (s)	Characteristic Diameter (km)	Average Proper Speed (km s^{-1})	Occurrence Rate (arcsec^{-2} min^{-1})
A	183	222	273	0.88	0.028
B	141	232	214	0.75	0.030
C	206	240	255	0.83	0.033
D	89	173	225	0.59	0.039
E	41	111	205	...[a]	0.002
F	6	...[a]	...[a]	...[a]	0.001

Note. [a] Too few samples to calculate.

the NBP lifetime. The histogram for brightness contains values from every time step, making the number of samples large. The detection thresholds for the lifetime and diameter measurement were 6.2 s and 135 km, respectively. The brightness threshold is set by the NBP detection algorithm (Section 3.2).

As for other automated detection methods (Sobotka et al. 1997; Watanabe et al. 2009), these histograms show exponential decrease. We fit the first two histograms with functions $y \propto \exp(-x/C)$, with C the characteristic value. In the case of Region A, a characteristic lifetime of 222 s and characteristic diameter of 273 km were obtained. The only striking difference between Ellerman bombs and normal NBPs is in the brightness panel, Ellerman bombs being extraordinary bright in the Hα wings—commensurate with their definition—but with overlap during their startup and decay phases, which makes the presence of a jet a necessary discriminator between Ellerman bombs and the brightest NBPs. We conclude that, apart from their brightness, Ellerman bombs are just like non-eruptive NBPs.

Table 2 shows the average proper-motion speed and occurrence rate of the NBPs in the six subregions. The average proper-motion speed was determined from NBPs with a lifetime longer than 60 s by dividing the distance between the disappearance and appearance locations by its lifetime, and taking the average of those for each region. The occurrence rate is defined by the average NBP occurrence frequency within one square arcsec area per minute.

Table 2 suggests a subdivision into three types of regions. First, Regions A, B, and C can be characterized as moat flow regions in which NBPs are relatively long-lived and large, moving with the same speed as that of the moat flow. Second, the occurrence rate in Region D, covering the outside of a penumbra-free area, is highest, but the NBPs do not move much and their lifetimes are relatively short. The appearance of NBPs in this region follows the intergranular lane morphology. Third, Region E and F sampling plages contain only a few individual NBPs that fit our detection algorithm. These lie mostly at the plage peripheries. The other bright features within the plages are too crowded for our detection scheme so that we cannot measure their characteristic lifetimes and diameters, but they tend to be smaller and more static.

5. DISCUSSION

Ellerman bomb occurrence, type, mechanism. Most Ellerman bombs in our data appear on the east side of the spot that has a well-developed penumbra. They seem to take part in the moat flow that emanates from the penumbra in their fast proper motion along the network (see Vargas Domínguez et al. 2007, 2008 for evidence that moat flows require penumbrae). In particular, the repetitive brightening of jet threads and the jet direction (away from disk center in the limbward field of view) suggests that new flux with near-vertical orientation arrives at the network as driven by the moat flow, and reconnects with the pre-existing, also largely vertical, network fields. The brightenings start low and extend rapidly upward in jet-like flames, sometimes evolving into bi-directional jets. The flows at the location of Ellerman bombs alternately change sign and the jet lengths extend and retract repetitively. This behavior indicates reconnection that takes place again and again by encountering pre-existing magnetic field. The highly supersonic apparent feature speeds measured from the wide-band data suggest phase speed rather than material motion, reminiscent of the shear motion described by van Ballegooijen et al. (1998).

The recent literature discusses multiple types of Ellerman bombs. In particular, Pariat et al. (2004, 2007) and Watanabe et al. (2008) found evidence for undulating "serpentine" field topologies with Ellerman bombs formed at the dip of field lines (called "bald patches" in the French literature), where the fields are nearly antiparallel. The fact that Ellerman bombs are reported to occur only in emerging flux regions speaks for an antiparallel reconnection scenario. The repetitivity of the bright-thread appearance while the Ellerman bomb migrates along the network may indeed result from sea-serpent field topology, but located in the photosphere rather than extending to the chromosphere.

Since we have no simultaneous magnetogram data at similar angular resolution, we can only speculate about the magnetic topology of our Ellerman bombs. There may be opposite-polarity field emergence with direct or with separatrix/separator reconnection (cf. Parnell & Galsgaard 2004), or there may be component reconnection between unipolar fields that shear along each other in differential moat flows. In our case, we did observe considerable field topology changes at the east side of the spot during the two magnetogram sequences taken before and after the Hα sequence, but this gives only an indication that further field emergence may well have taken place during the Hα sequence. We think it most likely that the Ellerman bombs in our data require a field topology that produces near-vertical reconnection deep in the photosphere, and we suspect that the moat flow is a key operator. The strong differential moat flow combined with the presence of a nearby bipolar plage might suffice as condition to produce our type of Ellerman bomb.

Recently, Guglielmino et al. (2010) reported an SST plus *Hinode* observation of a flux emergence region exhibiting an event much like our Ellerman bombs and accompanied by an Hα surge. They attribute it, with the help of simulation examples, to reconnection due to interaction between emerging flux and the pre-existing chromospheric and coronal field. In contrast, in our Ellerman bombs the reconnective interaction seems to

be fully defined within the photosphere, although 2 of our 17 Ellerman bombs do have an accompanying surge.

Photospheric formation. All Ellerman bombs in our Hα images originate from intergranular lanes, i.e., from regular granulation in the deep photosphere that is sampled by the Hα wings apart from occasional Doppler-shifted absorption features (Leenaarts et al. 2006b; Rouppe van der Voort et al. 2009; Paper I). The reversed granulation at heights $h = 100$–200 km is seen in Hα only closer to line center in extremely quiet fibril-free regions. All our Ellerman bombs lie below the chromospheric fibril canopy. Hα is commonly thought to be chromospheric; for example, Georgoulis et al. (2002) described their Ellerman bombs as low-chromosphere features on the basis of their detection in filtergrams at $\Delta\lambda = -0.8$ Å from Hα line center which suggests that these were actually as photospheric as ours. Therefore, our observations strengthen the conclusion of Georgoulis et al. (2002) that Ellerman bombs are probably a signature of low-altitude reconnection.

Similarity to chromospheric anemone jets. All our Ellerman bombs have extended jets; in fact, the jet presence became a selection criterion after our initial animation inspections. Shibata et al. (2007) reported the existence of so-called chromospheric anemone jets seen in Ca II H with the *Hinode* Solar Optical Telescope. They have lengths of 2000–5000 km and apparent extension speeds of 10–20 km s^{-1}. They are found preferentially in mixed-polarity regions (Morita et al. 2010). In particular, in a sunspot moat, Morita et al. (2010) found nine such chromospheric anemone jets with lifetimes ranging between 30 and 320 s, in good agreement with our Ellerman bomb durations. Some of our Ellerman bombs also show the inverted "Y" shape characteristic of anemone jets, and also the apparent jet extension speeds are comparable. Morita et al. (2010) attributed the jet extension speed to the Alfvén velocity in the low chromosphere; we note that the Alfvén velocity in the photosphere (at field strength 1000 G and density 10^{17} cm^{-3}) is comparable. The major difference is that the Ellerman bomb jets tend to reach smaller heights. Nevertheless, we suggest that our type of Ellerman bombs and chromospheric anemone jets represent the same phenomenon, with the difference in Hα and Ca II H extent perhaps due to the difference in fibril visibility in the two diagnostics.

Ellerman bomb heating. Our data suggest strongly that our Ellerman bombs are caused by magnetic reconnection of strong near-vertical network fields with also near-vertical field that is probably moat-flow driven into the network. Undoubtedly there is sizable heating. There are attempts to model the bright Hα wings of Ellerman bombs by adding appropriate temperature humps to standard models in one-dimensional modeling or inversion (Socas-Navarro et al. 2006; Berlicki et al. 2010), but these are likely to underestimate the upward extent of the heating by trying to also reproduce the dark Hα core which in reality is caused by opaque chromospheric fibrils that are not taken into account. We suspect that exceedingly large thermal line width, as proposed by Matsumoto et al. (2008) and particular to the Balmer lines due to the small atomic mass of hydrogen, may be an important aspect. Hα line synthesis in numerical magnetohydrodynamic simulations including encounter or close-encounter reconnection is obviously desirable.

6. CONCLUSION

The imaging spectroscopy presented in this paper is far superior to any Hα observation of Ellerman bombs in the literature. It yielded unprecedented spatial and temporal resolution that we exploited to describe the structure and evolution of the 17 Ellerman bombs seen in the Hα wings. They are all rooted deeply in the magnetic network on the side of a sunspot with strong moat flow, and they all have upright jets that reach considerable height, although these jets remain shielded by overlying chromospheric fibrils at Hα line center.

Although multiple types of Ellerman bombs and corresponding field configurations are reported in the literature, the ones reported here all seem to be photospheric events that are most likely explained by successive reconnection of strong vertical network fields with incoming, also vertical, field that is driven into the network by the moat flow.

The Hα observations presented in this paper have one obvious shortcoming: there was no simultaneous polarimetry performed that would provide corresponding magnetograms at similar angular resolution. Such data are required to study the topology and evolution of the magnetic fields at and around Ellerman bomb sites to ascertain what happens magnetically, in particular to establish the presence and action of field emergence and cancellation and to chart the field polarity. Note that such mapping should be photospheric. Chromospheric magnetometry is currently a grail of solar spectropolarimetry, but for Ellerman bombs such as the ones discussed here it would diagnose the field of overlying fibrils, not the bombs or their triggering, and be irrelevant unless the Ellerman bomb sends off a measurable surge.

In 2010, the Oslo group obtained new SST/CRISP sequences that combine Hα and Ca 8542 line scans with Fe I 6302 spectropolarimetry of a sunspot in an emerging flux region yet closer to the limb. These data are well suited for further study, presently underway, of the Ellerman bomb phenomenon.

We thank our colleagues at the Kwasan and Hida Observatories and at Kyoto University and Oslo University for fruitful discussions. This research was supported by a Grant-in-Aid for JSPS Fellows, a Grant-in-Aid for the Global COE Program "The Next Generation of Physics, Spun from Universality and Emergence" of the Ministry of Education, Culture, Sports, Science and Technology (MEXT) of Japan, and by the Research Council of Norway through grants 177336/V30 and 191814/V30. The Swedish 1-m Solar Telescope is operated on the island of La Palma by the Institute for Solar Physics of the Royal Swedish Academy of Sciences in the Spanish Observatorio del Roque de los Muchachos of the Instituto de Astrofísica de Canarias. R.J.R. visited Japan as a guest of NAOJ at Mitaka and acknowledges hospitality at Kyoto University and Hida Observatory.

REFERENCES

Berlicki, A., Heinzel, P., & Avrett, E. H. 2010, Mem. Soc. Astron. Ital., 81, 646
de Wijn, A. G., Stenflo, J. O., Solanki, S. K., & Tsuneta, S. 2009, Space Sci. Rev., 144, 275
Ellerman, F. 1917, ApJ, 46, 298
Georgoulis, M. K., Rust, D. M., Bernasconi, P. N., & Schmieder, B. 2002, ApJ, 575, 506
Guglielmino, S. L., Bellot Rubio, L. R., Zuccarello, F., Aulanier, G., Vargas Domínguez, S., & Kamio, S. 2010, ApJ, 724, 1083
Hashimoto, Y., et al. 2010, PASJ, 62, 879
Isobe, H., Tripathi, D., & Archontis, V. 2007, ApJ, 657, L53
Leenaarts, J., Rutten, R. J., Carlsson, M., & Uitenbroek, H. 2006a, A&A, 452, L15
Leenaarts, J., Rutten, R. J., Sütterlin, P., Carlsson, M., & Uitenbroek, H. 2006b, A&A, 449, 1209
Litvinenko, Y. E. 1999, ApJ, 515, 435
Matsumoto, T., Kitai, R., Shibata, K., Otsuji, K., Naruse, T., Shiota, D., & Takasaki, H. 2008, PASJ, 60, 95

Morita, S., Shibata, K., Ueno, S., Ichimoto, K., Kitai, R., & Otsuji, K. 2010, PASJ, 62, 901
Ortiz, A., Bellot Rubio, L. R., & Rouppe van der Voort, L. 2010, ApJ, 713, 1282
Pariat, E., Aulanier, G., Schmieder, B., Georgoulis, M. K., Rust, D. M., & Bernasconi, P. N. 2004, ApJ, 614, 1099
Pariat, E., Schmieder, B., Berlicki, A., Deng, Y., Mein, N., López Ariste, A., & Wang, S. 2007, A&A, 473, 279
Parnell, C. E., & Galsgaard, K. 2004, A&A, 428, 595
Rouppe van der Voort, L., Leenaarts, J., de Pontieu, B., Carlsson, M., & Vissers, G. 2009, ApJ, 705, 272
Scharmer, G. B., Bjelksjo, K., Korhonen, T. K., Lindberg, B., & Petterson, B. 2003a, Proc. SPIE, 4853, 341
Scharmer, G. B., Dettori, P. M., Lofdahl, M. G., & Shand, M. 2003b, Proc. SPIE, 4853, 370
Scharmer, G. B., et al. 2008, ApJ, 689, L69
Shibata, K., Nishikawa, T., Kitai, R., & Suematsu, Y. 1982, Sol. Phys., 77, 121
Shibata, K., et al. 2007, Science, 318, 1591
Shine, R. A., Title, A. M., Tarbell, T. D., Smith, K., Frank, Z. A., & Scharmer, G. 1994, ApJ, 430, 413
Sobotka, M., Brandt, P. N., & Simon, G. W. 1997, A&A, 328, 682
Socas-Navarro, H., Martínez Pillet, V., Elmore, D., Pietarila, A., Lites, B. W., & Manso Sainz, R. 2006, Sol. Phys., 235, 75
van Ballegooijen, A. A., Nisenson, P., Noyes, R. W., Löfdahl, M. G., Stein, R. F., Nordlund, Å., & Krishnakumar, V. 1998, ApJ, 509, 435
van Noort, M. J., & Rouppe van der Voort, L. H. M. 2008, A&A, 489, 429
van Noort, M., Rouppe van der Voort, L., & Löfdahl, M. G. 2005, Sol. Phys., 228, 191
Vargas Domínguez, S., Bonet, J. A., Martínez Pillet, V., Katsukawa, Y., Kitakoshi, Y., & Rouppe van der Voort, L. 2007, ApJ, 660, L165
Vargas Domínguez, S., Rouppe van der Voort, L., Bonet, J. A., Martínez Pillet, V., Van Noort, M., & Katsukawa, Y. 2008, ApJ, 679, 900
Watanabe, H., Kitai, R., & Ichimoto, K. 2009, ApJ, 702, 1048
Watanabe, H., et al. 2008, ApJ, 684, 736
Yokoyama, T., & Shibata, K. 1995, Nature, 375, 42

II

Ellerman Bombs at High Resolution. II.
Triggering, Visibility, and Effect on the Upper Atmosphere
G. Vissers, L. Rouppe van der Voort and R. Rutten
Submitted to The Astrophysical Journal (2013)

III

Flocculent flows in the Chromospheric Canopy of a Sunspot
G. Vissers and L. Rouppe van der Voort
The Astrophysical Journal, Volume 750, 22 (2012)

The Astrophysical Journal, 750:22 (12pp), 2012 May 1 doi:10.1088/0004-637X/750/1/22

FLOCCULENT FLOWS IN THE CHROMOSPHERIC CANOPY OF A SUNSPOT

Gregal Vissers and Luc Rouppe van der Voort
Institute of Theoretical Astrophysics, University of Oslo, P.O. Box 1029 Blindern, N-0315 Oslo, Norway; g.j.m.vissers@astro.uio.no
Received 2011 December 23; accepted 2012 February 21; published 2012 April 12

ABSTRACT

High-quality imaging spectroscopy in the Hα line, obtained with the CRisp Imaging SpectroPolarimeter (CRISP) at the Swedish 1-m solar Telescope (SST) at La Palma and covering a small sunspot and its surroundings, is studied. They exhibit ubiquitous flows both along fibrils making up the chromospheric canopy away from the spot and in the superpenumbra. We term these flows "flocculent" to describe their intermittent character, that is, morphologically reminiscent of coronal rain. The flocculent flows are investigated further in order to determine their dynamic and morphological properties. For the measurement of their characteristic velocities, accelerations, and sizes, we employ a new versatile analysis tool, the CRisp SPectral EXplorer (CRISPEX), which we describe in detail. Absolute velocities on the order of 7.2–82.4 km s^{-1} are found, with an average value of 36.5 $\pm$ 5.9 km s^{-1} and slightly higher typical velocities for features moving toward the sunspot than away. These velocities are much higher than those determined from the shift of the line core, which shows patches around the sunspot with velocity enhancements of up to 10–15 km s^{-1} (both red- and blueshifted). Accelerations are determined for a subsample of features that show clear accelerating or decelerating behavior, yielding an average of 270 $\pm$ 63 m s^{-2} and 149 $\pm$ 63 m s^{-2} for the accelerating and decelerating features, respectively. Typical flocculent features measure 627 $\pm$ 44 km in length and 304 $\pm$ 30 km in width. On average, 68 features are detected per minute, with an average lifetime of 67.7 $\pm$ 8.8 s. The dynamics and phenomenology of the flocculent flows suggest they may be driven by a siphon flow, where the flocculence could arise from a density perturbation close to one of the footpoints or along the loop structure.

Key words: Sun: activity – Sun: atmosphere – Sun: chromosphere – sunspots

Online-only material: animation

1. INTRODUCTION

The advent of imaging spectroscopy at high-resolution solar telescopes using adaptive optics and image post-processing allows the study of solar phenomena at unprecedented spatial, temporal, and spectral resolution. In this paper, we analyze a high-quality set sampling the chromosphere above a small sunspot and its surroundings in the Hα line. The chromospheric canopy exhibits ubiquitous fast-moving small-scale features constituting flows both toward and away from the sunspot in the superpenumbra, as well as in fibrils anchored in plage only. We call these features and flows "flocculent"[1] to characterize their intrinsic intermittency.

Similar blob-like phenomena have recently been observed by Van Noort & Rouppe van der Voort (2006), Sánchez-Andrade Nuño et al. (2008), Wedemeyer-Böhm (2010), and Lin et al. (2012), and have been interpreted as a manifestation of propagating waves rather than actual mass motion. With spatial dimensions of 0.5–1 arcsec or less, the features observed are seen to propagate along the fibrillar canopy structure observed in Hα and Ca II 8542 Å, in some cases with additional periodic lateral displacement, at velocities close to (and in most cases well in excess of) the chromospheric sound speed.

The flocculent flows above the sunspot and in its superpenumbra that are reported on here are reminiscent of coronal rain as well as the inverse Evershed effect, and may constitute mass motions rather than waves. We therefore complete this introduction with brief reviews of the coronal rain phenomenon and the (inverse) Evershed effect.

[1] They are not the "flocculi" reported in the older solar literature, in reference to unresolved Ca II H & K network (e.g., Bray & Loughhead 1974).

Coronal rain. In coronal loops both (transient) siphon flows (e.g., Kjeldseth-Moe & Brekke 1998; Doyle et al. 2006; Tian et al. 2009) and "blobs" of cooled down plasma (the so-called *coronal rain*) precipitating along the legs of coronal loops (e.g., Schrijver 2001; Müller et al. 2005; De Groof et al. 2005; O'Shea et al. 2007) have been observed. Typical velocities for coronal rain range between a few tens to a few hundred km s^{-1} (Schrijver 2001; De Groof et al. 2005; O'Shea et al. 2007), which was corroborated through simulations by Müller et al. (2005). Recent studies by Antolin & Rouppe van der Voort (2012) and Antolin et al. (2012) have further expanded the statistics for both off-limb and on-disk cases, respectively, confirming earlier dynamics results. Catastrophic cooling is generally accepted as explanation of the coronal rain phenomenon. In this process, as advanced by Schrijver (2001), thermal non-equilibrium leads to condensation of plasma at the loop apex followed by a runaway cooling process, with subsequent downflow of one or more blobs along one or both loop legs. The siphon flow velocities in coronal loops are similar to the velocities found for coronal rain (cf. Kjeldseth-Moe & Brekke 1998; Doyle et al. 2006), but do not result in blobs falling down toward the photosphere.

(Inverse) Evershed effect. The inverse Evershed effect is a chromospheric inflow of plasma along superpenumbral fibrils toward the sunspot umbra, while the outflow observed in the photospheric penumbra is referred to as the (normal) Evershed effect. The latter was first discovered by Evershed (1909a) and has been extensively studied in the years since, leading to relatively well-established values for the outflow velocity of the order of a few km s^{-1} near the umbra–penumbra boundary increasing up to about 10 km s^{-1} at the outer penumbral edge. Though several models have been proposed in the past, thermal convective motions are nowadays most widely accepted as

the driving mechanism for the Evershed effect (cf. Spruit & Scharmer 2006; Heinemann et al. 2007; Rempel et al. 2009; Nordlund & Scharmer 2010; Scharmer et al. 2011).

The existence of the inverse Evershed effect was already suggested by Evershed (1909b) following his discovery of the photospheric outflow and more extensively studied by St. John (1913), who confirmed the earlier findings of Evershed that in the chromosphere the flow reverses sign with respect to the photosphere. Siphon flows are most often proposed as the mechanism behind the inverse Evershed effect (cf. Haugen 1969; Maltby 1975; Alissandrakis et al. 1988; Dere et al. 1990; Boerner & Kneer 1992; Kjeldseth-Moe et al. 1993; Montesinos & Thomas 1997), with only few alternatives, such as gravitationally driven in- and downflow (Beckers 1962) or some mechanism analogous to the moving flux tube model (Teriaca et al. 2008). A wide range in velocities is found, however. St. John (1913) found the inverse Evershed effect to propagate with about 3 km s^{-1} on average and similar velocities were obtained by Bones & Maltby (1978), while somewhat higher velocities were found by Haugen (1969), Dere et al. (1990), and Alissandrakis et al. (1988). However, measurements of single absorbing elements in the Hα spectra analyzed by Haugen (1969) resulted in velocities of up to 50 km s^{-1} and even higher velocities were obtained in filtergram studies by Beckers (1962) and Maltby (1975). This difference between spectroscopic and filtergram velocities was already pointed out before by Alissandrakis et al. (1988). The inverse Evershed effect has also been observed in the transition region, albeit at typically higher Doppler velocities on the order of a few tens of km s^{-1} obtained from spectral analyses (Alissandrakis et al. 1988; Dere et al. 1990; Kjeldseth-Moe et al. 1993; Teriaca et al. 2008), and it has not been as extensively studied as in the chromosphere.

In summary, the basic picture that arises from previous studies of the (inverse) Evershed effect is one of relatively slow penumbral outflow in the photosphere, a faster inflow in the superpenumbra at chromospheric levels, and an even faster inflow in the transition region.

In this paper we describe, measure, and interpret the flocculent flows in our data. The measurements on the data were done using a newly developed analysis tool, the CRisp SPectral EXplorer (CRISPEX, further details in the Appendix), that is primarily aimed at imaging spectroscopy data. The observational data are introduced in the following Section 2, after which the results of a statistical analysis of these flows are presented in Section 3. Section 4 offers a discussion of the results obtained in the light of similar and possibly related phenomena such as the inverse Evershed effect and coronal rain, after which conclusions are drawn in Section 5.

2. OBSERVATIONS, DATA REDUCTION, AND ANALYSIS METHODS

2.1. Observational Setup

The Hα data used in this study were obtained with the CRisp Imaging SpectroPolarimeter (CRISP; Scharmer et al. 2008), at the Swedish 1-m Solar Telescope (SST; Scharmer et al. 2003a) at La Palma (Spain). In the setup for these observations the light from the telescope is first guided through an optical chopper and a wavelength selection prefilter before entering the CRISP instrument (a dual Fabry–Pérot interferometer (FPI) system with a transmission FWHM at the Hα wavelength of 6.6 pm and wavelength tuning within a spectral line on the order of $\lesssim$50 ms). The chopper ensures synchronization of the exposures obtained and for the observations considered here, the Hα line was selected by using a prefilter centered on 6563.8 Å with an FWHM of 4.9 Å. After CRISP, the light beam is split by an orthogonally polarizing beam splitter onto two cameras. In addition, before entering the FPI but after the prefilter, a few percent of the light is redirected to a third camera, which serves as a wide-band anchor channel in the image post-processing. All three cameras are high-speed low-noise Sarnov CAM1M100 CCD cameras operating at a frame rate of 35 frames s^{-1} with an exposure time of 17 ms.

2.2. Data Acquisition and Reduction

The Hα sequence in question was acquired on 2008 June 11 between 7:55–8:32 UT. The data consist of a time series of profile scans sampling the Hα line at 23 wavelengths, ranging between $\pm$1.1 Å around line center at 0.1 Å spacing. At each wavelength a burst of eight exposures was taken, thus resulting in an overall cadence of 6.2 s per profile scan. The field of view covers an area of about 67 $\times$ 67 arcsec^2 and contains a small sunspot with a rudimentary penumbra (AR 10998), located at $(X, Y) \approx (-684,-152)$, corresponding to $\mu = 0.67$. Figure 1 shows samples of the observed region in Hα line center (left panel) and the blue wing (H$\alpha - 0.7$ Å, right panel). The pixel size is 0.071 arcsec pixel^{-1}, well below the SST's Rayleigh diffraction limit for Hα, which is 0.17 arcsec.

With the use of real-time tip-tilt correction and the adaptive optics system at the SST (Scharmer et al. 2003b), as well as the image post-processing technique Multi-Object Multi-Frame Blind Deconvolution (MOMFBD; Van Noort et al. 2005), the quality of observations can be greatly improved, the latter being employed in order to remove the remaining high-order seeing effects. To that end, all images (i.e., at each wavelength within the profile scan) were divided into 64 $\times$ 64 pixels^2 overlapping subfields to be processed as a single MOMFBD restoration. In that process, the wide-band exposures act as anchors that enable the precise alignment of the restored narrowband CRISP images. More information on the MOMFBD post-processing of similar data sets can be found in Van Noort & Rouppe van der Voort (2008).

After MOMFBD restoration, the data were further corrected for the transmission profile of the wide-band prefilter and for the effects of diurnal rotation of the image that result from the alt-azimuth design of the SST. Finally, the images are also de-stretched following Shine et al. (1994), which removes most of the remaining small-scale rubber-sheet seeing effects.

2.3. Flocculent Flows

Closer inspection of the image sequence in either wing of Hα shows the presence of flows along what, by comparison with the line center image, appears to constitute the chromospheric canopy (including as such the superpenumbral fibrils of the small sunspot). The flows are neither uniform nor continuous but rather flocculent, i.e., the flows are observed as dark condensations or blobs flowing along the chromospheric fibril structures.

Figure 2 (and in particular the animation of that figure) shows examples of flocculent features (arrows). Note that the features in the middle left panel are not visible in the rightmost panel and vice versa, i.e., the same features are not visible in both wings simultaneously. The apparent coincidence of the trajectories of these flocculent features with superpenumbral fibrils as well as the main flow direction are reminiscent of

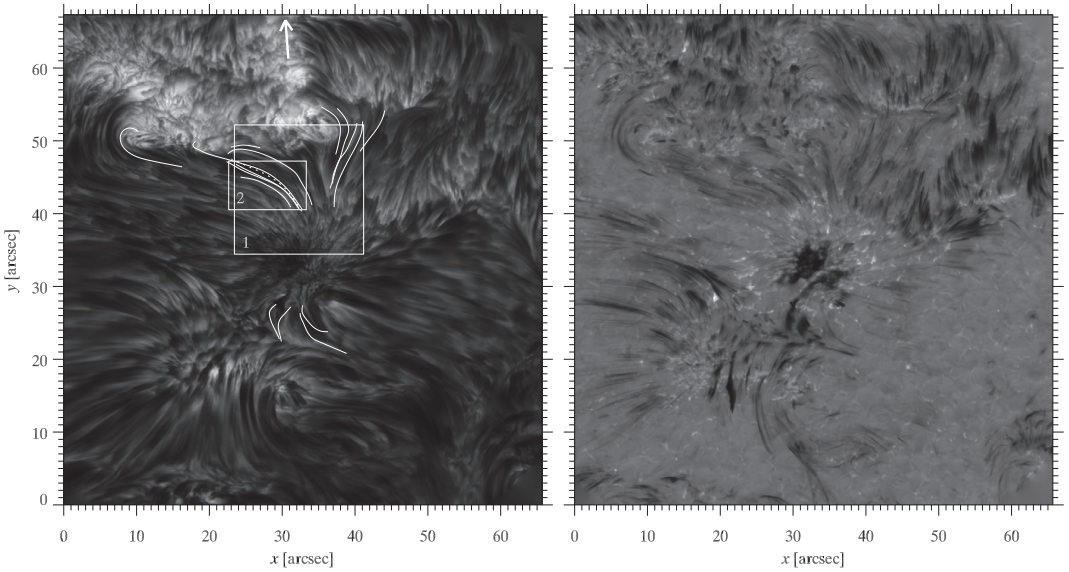

Figure 1. Sample images. Left: full field of view in Hα line center. The loop paths defined with CRISPEX along which space–time diagrams have been extracted are overlaid. The dashed path is discussed in detail in Section 3.1.1 and Figure 4. The numbered white boxes indicate regions of interest that are discussed further in Section 2.3 (cf. Figures 2 and 3, respectively). The arrow at the top of the panel indicates the direction of the limb and the line of sight (pointing away from the observer). Right: the same field of view in Hα -0.7 Å.

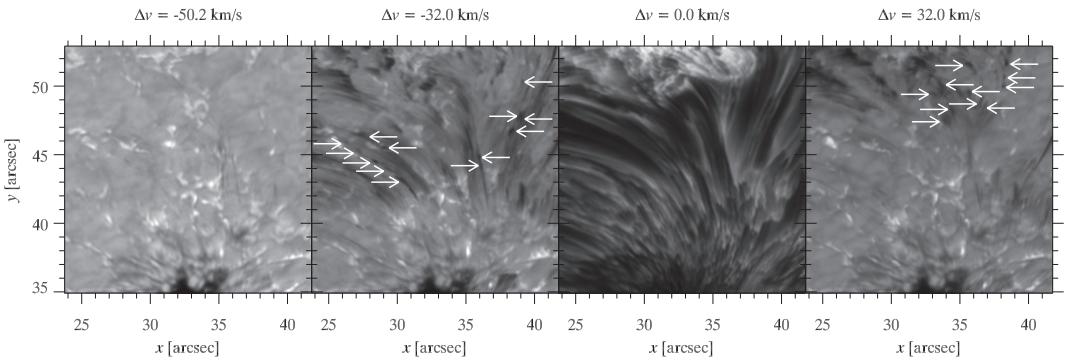

Figure 2. Cutout from Figure 1 of region of interest (ROI) 1 at different wavelengths: Hα -1.1 Å ($\Delta v = -50.2$ km s^{-1}, leftmost panel), Hα -0.7 Å ($\Delta v = -32.0$ km s^{-1}, middle left panel), Hα line center itself (middle right panel), and Hα+0.7 Å ($\Delta v = +32.0$ km s^{-1}, rightmost panel). The arrows indicate some examples of inflowing and outflowing features.

(An animation of this figure is available in the online journal.)

the properties of the inverse Evershed flow. It should be noted, however, that these flocculent flows occur more generally (i.e., also along fibrils that connect different network locations) and not necessarily only propagating toward the sunspot. Although some of these outward moving features can be found near the sunspot, they typically appear farther away from the sunspot, toward a downflow footpoint anchored in the network. The features occur typically in streams, either throughout the whole observing period or, what appears to be more common, in recurrent, shorter episodes of intermittent appearance.

Some fibrils remain dark in the wings of Hα throughout most of the time series or show slower dynamics than the flocculent flows. The right-hand panel of Figure 1 shows a number of these. In some cases the flocculent features and these constantly present dark fibril structures seem superimposed on each other, whereas in other cases also fibrils move down toward the sunspot, albeit at smaller velocities (cf. for instance the middle left panel of the online animation).

Figure 3 shows spectral properties of a typical flocculent feature. The bottom panel shows the feature in an intensity image in the wing of Hα at a shift of -0.7 Å (or equivalently, $\Delta v = -32.0$ km s^{-1}). During its visibility in the data sequence, the feature moves along an arched path from the left to the right through the field of view, curving down to the lower right of the subfield shown (toward the sunspot which lies just outside this subfield on the lower right side), with similar other features

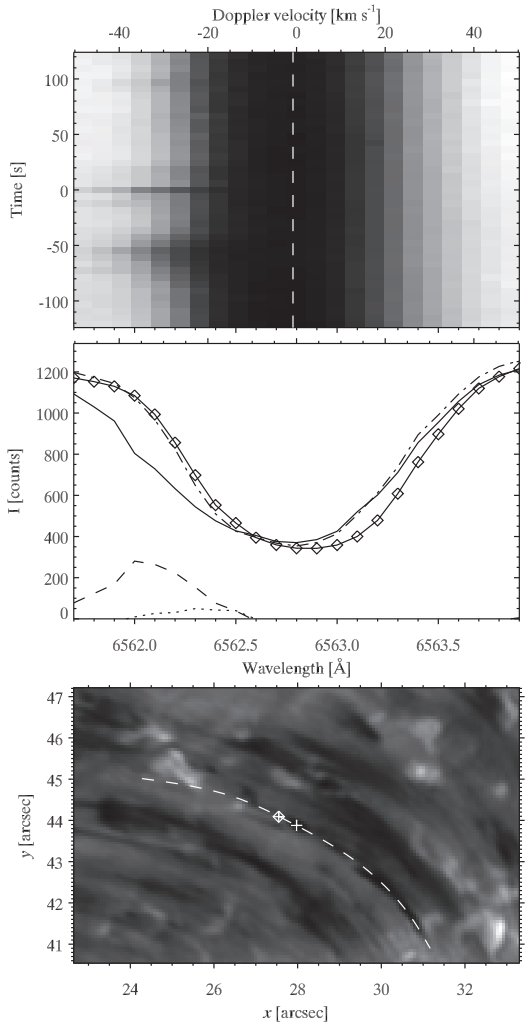

Figure 3. Spectral properties of a typical flocculent feature occurring in ROI 2. Top panel: spectrum–time diagram at the location marked with a white cross in the bottom panel. $t = 0$ is defined as the instant sampled by the middle and lower panels. Around $t = -50$ s another flocculent feature crossed that location. The white dashed line indicates the average line core shift over the displayed time range. Middle panel: spectral profile (solid line) and difference profile (the spectral profile subtracted from the field-of-view-averaged profile, dashed line) of the flocculent feature. A similar set of profiles (dash-dotted and dotted lines, respectively) is shown for the neighboring location, without a flocculent feature, specified by the cross-diamond in the bottom panel. In addition, the full field-of-view-averaged profile (solid curve with diamonds) is shown. Bottom panel: intensity image at Hα -0.7 Å, showing an example of a flocculent feature. The dashed curve specifies the path of the flocculent feature.

preceding it and features in adjacent fibril structures. The middle and upper panels of Figure 3 illustrate that the flocculent features are most clearly observed in the Hα wings. The flocculent flows are composed of features with typical Doppler shifts between 20–40 km s^{-1} in either the blue or red wing of Hα, depending on their propagation direction with respect to the observer. Note that the features appear to show up as a separate component to

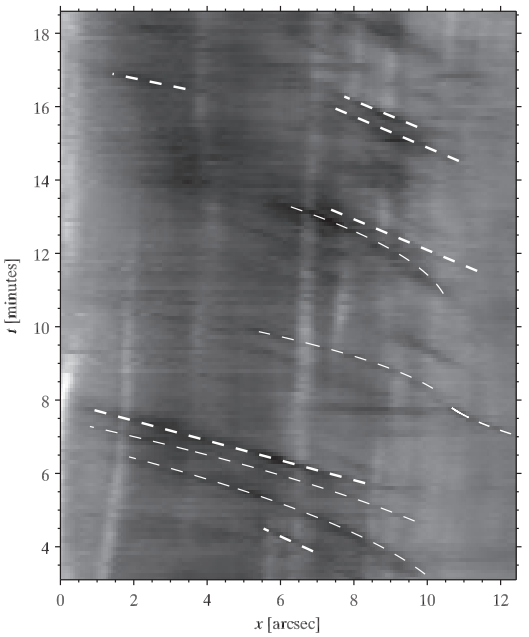

Figure 4. Part of the space–time diagram extracted along dashed track in Figure 1. The space–time diagram was extracted at H$\alpha - 0.7$ Å ($\Delta v = -32.0$ km s^{-1}). The dashed curves indicate measurements of the projected velocity and acceleration components and illustrate the method discussed in Section 2.3.

the local spectrum (the dashed line), as illustrated in the middle panel. In this particular case, where an inflow toward the sunspot is observed, a separate component appears to be superimposed upon an overall shift of the line core. Though the extent to which this separate component is visible in the spectrum may vary with location, time, and propagation direction with respect to the line of sight, it is a typical property of the flocculent flows.

2.4. Methods

2.4.1. Velocities and Accelerations

Using the path-drawing functionality in CRISPEX, flocculent features were manually traced along their visible trajectories and space–time diagrams were subsequently extracted along these paths. The left-hand panel of Figure 1 shows the final selection of the determined paths overlain on the Hα line center image, while Figure 4 shows such an extracted space–time diagram corresponding to the dashed track in the former figure. As the features appear as dark streaks in these diagrams, the determination of their projected velocities and accelerations is a relatively trivial task that was further simplified by using the CRISPEX auxiliary program TANAT.

The majority of the dark streaks in the extracted space–time diagrams are straight, and hence a single measurement suffices to obtain the projected velocity component in those cases. However, some features have curved space–time tracks; these are fitted with a parabola to three points along them, yielding estimates of the corresponding acceleration or deceleration. Dashed lines have been overlaid in Figure 4 to illustrate this procedure. A measure for the error in the projected velocities

and accelerations was determined by repeatedly measuring randomly selected dark streaks in each space–time diagram resulting in a measurement uncertainty of 4.0 km s^{-1} and 63 m s^{-2} for the velocity and acceleration, respectively.

The Doppler velocity of the separate component was obtained employing two methods, a determination of the first moment with respect to wavelength and a Gaussian fit, both to the difference profile (cf. the middle panel of Figure 3). In the first we followed Rouppe van der Voort et al. (2009, see also Equation (1) therein), where the first moment method was applied to Rapid Blue Excursions (RBEs). The integration is only performed over the range where $I_\lambda^{\rm avg} - I_\lambda$ is positive (i.e., the feature is in absorption). For the Gaussian fit method, the same constraint is enforced and only the spectral points over that same range are used in fitting a single Gaussian with the height, position, and width of the peak as the three parameters to be fitted. For both methods, an estimate of the error in each Doppler velocity determination was obtained by repeating the calculations with boundaries progressively shifted inward by one wavelength position at a time. The error for that particular Doppler velocity was then set to the standard deviation of those measurements, resulting in an average error of 0.7 km s^{-1} and 4.3 km s^{-1} for the first moment and Gaussian fit method, respectively.

While the separate component constitutes in large part the line-of-sight signal of a flocculent feature, it is typically superimposed on an overall shift of the line core, which may be indicative of a lower velocity flow at the same location. Both a Gaussian and a fourth-order polynomial were therefore fitted to the core of the line (typically the middle 11 wavelength positions) at each pixel and for each time step. Comparison of the resulting fits with the actual local line profile showed the fourth-order polynomial to be more robust in fitting the core of the Hα line than the Gaussian. Hence, the results from the polynomial fits were used to construct a Doppler map for each time step, where the offset between the local minimum in the line profile and that in the average line profile was converted to a Doppler shift velocity. This is also a habitual way in which velocities for the inverse Evershed effect have been obtained in spectroscopic studies.

2.4.2. Morphological Parameters

The flocculent features' lengths and widths were determined as follows. For each flocculent feature, the intensity profile along the spatial axis was extracted from the space–time diagram at the wavelength closest to its average Doppler velocity and subtracted from the field-of-view-averaged intensity at that wavelength. Next, a difference profile was determined by subtracting the average background intensity profile (i.e., the profile averaged over the time intervals in the space–time diagram where no flocculent features were measured) from the feature's intensity profile. The difference profile was subsequently lowered by the smallest of the two minima closest to the maximum representing the feature location, as not doing so typically resulted in an overestimation of the FWHM. Finally, a Gaussian fit to the resulting profile was performed, yielding an FWHM that was converted to a length. However, in order to ensure that only flocculent features (rather than the background) were measured, those measurements for which the feature FWHM was smaller than the FWHM resulting from a fit to the background profile (over the same spatial points) were rejected. This procedure was then repeated for each point along the velocity measurement, yielding a set of length measurements for each flocculent feature, the average of which was taken to be the length of the feature in question. A similar procedure was adopted to obtain feature widths, but using the intensity image instead, i.e., stepping along the traced path of the feature while it propagates and extracting the intensity profile perpendicular to (rather than along) the propagation direction.

Since the values of the fitted parameters are influenced by the number of points included in the Gaussian fit (i.e., the more points included, the larger the resulting FWHM typically is), both the length and width profile were fitted over three different ranges. Lengths were calculated by taking 11, 21, and 31 points into account, while the width profile was fitted with 5, 11, and 17 points, in both cases centered on the coordinates where the feature was measured. The FWHM resulting from the different fits for which the 1σ value is lowest and equal to or smaller than 1 pixel was then selected as the feature size, while the standard deviation between the three results was taken to be a measure of the uncertainty in the size determination. The average error for the lengths is 44 km, while that for the widths is 30 km.

3. RESULTS

3.1. Dynamics of the Flocculent Flows

3.1.1. Projected Velocities

In total, we obtained 259 velocity measurements of which 188 can be identified with features moving toward the spot, the remaining 71 features moving in the opposite direction. As pointed out before, the latter features are observed mostly toward the footpoints in the network, rather than closer to the sunspot, though still in structures that appear connected to the sunspot. Figure 5 shows in the upper panel a frequency histogram of the projected velocity determinations.

The distribution of all measurements peaks around 20 km s^{-1}, with a tail extending up to almost 80 km s^{-1}, resulting in an average velocity of 27.4 km s^{-1}. There is a significant difference between inflow (toward the sunspot) and outflow, yielding average velocities of 30.2 km s^{-1} and 20.0 km s^{-1}, respectively. The high-velocity tail of the distribution is dominated by features moving toward the sunspot, while the lower velocities are relatively more abundant for features moving in the opposite direction.

3.1.2. Doppler Velocities

As the Gaussian fit requires a minimum of three data points, this results in fewer successful Doppler velocity determinations than for the first moment method, reducing the total number of measurements by about 18%, compared to the reduction of about 9% with the first moment approach. Nevertheless, both the distributions of Doppler velocities are very similar regardless of the method, their averages falling within each other's measurement error as determined above. On the one hand, this validates the first moment approach, while showing on the other hand that the influence on the derived statistics of the reduced number of valid measurements for the Gaussian fit method is small.

The middle panel of Figure 5 shows the overall Doppler distribution, as well as that of the subsamples for features moving toward and away from the sunspot. The determined Doppler velocities range between −31.4 km s^{-1} and 36.6 km s^{-1}, with an average of −8.2 km s^{-1} (or −16.5 km s^{-1} and 14.6 km s^{-1} when considering the inflowing and outflowing subsamples, separately). The blueshift peak is dominated by features moving toward the sunspot, as expected from the orientation of the majority of the tracks shown in Figure 1 with respect to the slanted

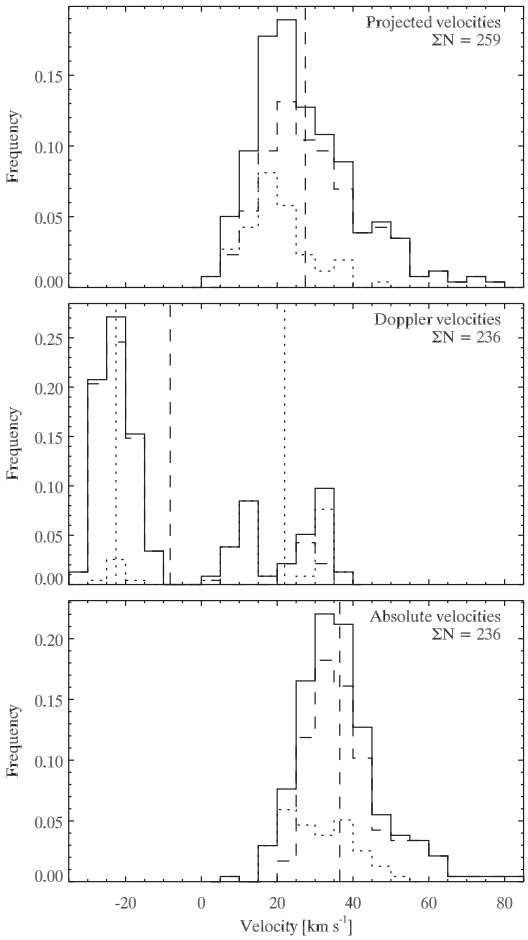

Figure 5. Velocity histograms of the flocculent features with a bin size of 5 km s^{-1}. Top panel: projected velocities obtained from measurement in the space–time diagrams. Middle panel: Doppler velocities. Bottom panel: absolute velocities obtained by combining the projected and Doppler velocities through vector addition. In each panel the solid distribution describes all measurements, the dashed one describes the subsample of features moving toward the sunspot, and the dotted one those moving away. The vertical dashed lines indicate the average velocity of all considered measurements, while the dotted lines in the middle panel show the average Doppler velocity of the positive and negative subsamples.

line of sight. Conversely, features that move away from the sunspot along these tracks are redshifted. The average Doppler shift for the blueshifted features is −22.6 km s^{-1}, with the average of the subsamples differing by less than about 0.3 km s^{-1} from the total average. The redshifted features show a double-peaked distribution, centered around 10 km s^{-1} and 35 km s^{-1}, respectively, and with an average of 21.9 km s^{-1}. As the contribution of the outflowing features is mostly to the lower of those two peaks, its average is correspondingly lower than that of the inflowing features that contribute almost exclusively to the higher velocity peak.

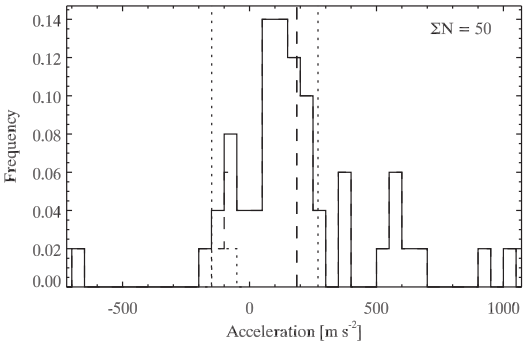

Figure 6. Histogram of the acceleration measurements. Solid line: all measurements. Dashed line: features moving toward the sunspot. Dotted line: features moving away from the sunspot. The vertical lines indicate the average over all measurements (dashed), as well as decelerations and accelerations (dotted). The bin size is 50 m s^{-2}.

3.1.3. Absolute Velocities

Combining the projected and Doppler component velocities produced the distributions in the bottom panel of Figure 5. Both the shapes of the distributions and range in velocities are similar to those in the upper panel. The absolute velocities found range between 7.2 and 82.4 km s^{-1}, with an average of 36.5 km s^{-1} when taking all measurements into account. Considering the inflow and outflow subsamples separately, the averages are 38.8 km s^{-1} and 30.3 km s^{-1}, respectively. Propagating the uncertainties determined for the projected and Doppler velocities to the absolute velocity, the average error in the absolute velocity was found to be 5.9 km s^{-1}.

3.1.4. Accelerations

Figure 6 shows the frequency histogram for the 50 acceleration measurements. Of these, 40 correspond to accelerations, whereas 10 are of decelerations (of which 8 are of features moving toward the sunspot and 2 of features moving in the opposite direction). The average acceleration (i.e., only including positive values) is 270 m s^{-2}, which lies close to the gravitational acceleration in the solar photosphere of 274 m s^{-2}. However, this coincidence is fortuitous since most values are much smaller; the average is boosted by the eight outliers with values in excess of 400 m s^{-2}. Note that the motion of the flocculent features is likely field-guided, so that only the component along the fibrillar path acts as effective gravity.

The average deceleration is much smaller (149 m s^{-2}), with an only slightly higher value of 162 m s^{-2} when considering the features moving toward the sunspot and a yet smaller value (96 m s^{-2}) for features moving toward the network.

3.1.5. Lifetimes and Occurrence Frequency

Lifetimes were determined using the start- and endpoints of each space–time feature track as in Figure 4. The right-hand panel of Figure 7 shows the resulting distribution. The 12.4 s lower cutoff results from requiring at least two samplings for a velocity measurement. The mean visibility lifetime is 67.7 ± 8.8 s, with no significant difference between in- and outward motion. Note that the lifetimes are rather lower limits, as the features become obscured by fibrils at line center when the Doppler velocity becomes small.

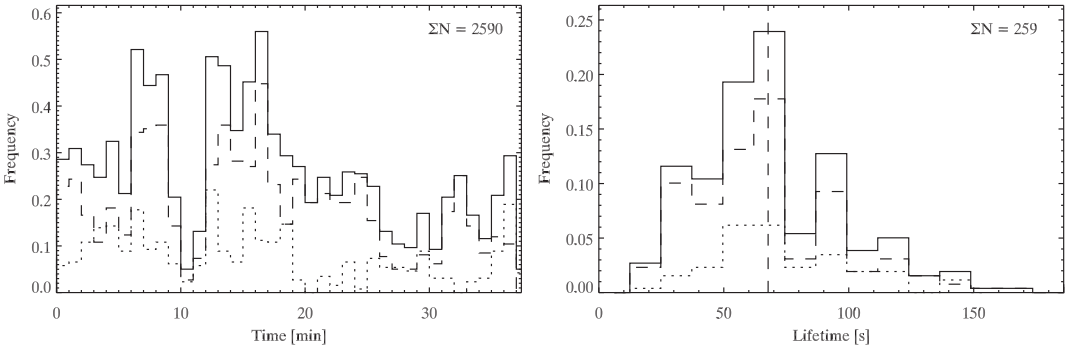

Figure 7. Occurrence frequency (left panel, 1 minute bins) and lifetimes (right panel, 12.4 s bins). Solid line: all measurements. Dashed line: features moving toward the sunspot. Dotted line: features moving away from the sunspot. The vertical dashed line in the right-hand panel indicates the average lifetime.

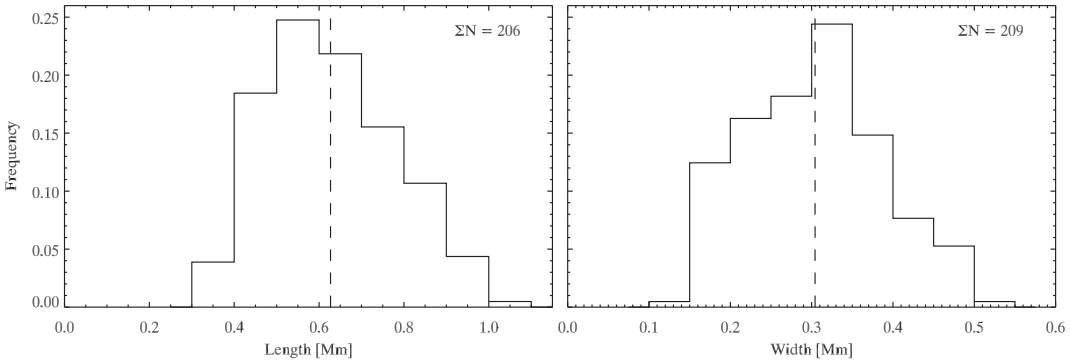

Figure 8. Size histograms showing flocculent feature lengths (left panel, bin size of 100 km) and widths (right panel, bin size of 50 km).

The occurrence frequency was derived by counting the number of measurements at each single time step, resulting in the histograms shown in the left-hand panel of Figure 7. On average 68 features can be observed each minute, with an average occurrence rate of 47 and 20 features minute^{-1} for the in- and outflow subsamples, respectively. The occurrence frequency appears to decrease somewhat during the second half of the observations, after a peak of 145 occurrences in one minute.

3.2. Shapes of Flocculent Features

Figure 8 shows the size distributions of the flocculent features. Out of 236 features with successfully determined Doppler velocities, lengths could be determined for 206 features, while 209 widths were obtained. The lower cutoff in both distributions is at the telescope diffraction limit. Upper cutoffs were visually set at 20 pixels (or about 1 Mm) for the lengths and at 10 pixels (equivalent to slightly over 500 km) for the widths. On average, the flocculent features measure 627 km in length and 304 km in width, but lengths range between 353 and 1005 km, while widths of 141–509 km are found.

We also determined eccentricities for those 186 features with both length and width measurements. In general, the features are largest in the propagation direction; only three features have a larger "width" than "length." On average, the eccentricity of the flocculent features is 0.83 ± 0.05, with the same value for the average for the larger prolate sample of 183 features, while the average for the oblate sample of the three features is much smaller (0.27 ± 0.05).

The morphology of the flocculent features changes only slightly as they progress along their trajectories. Some features appear to get stretched in length as they move toward the sunspot, while others appear to be compressed. Slightly more features are found to expand rather than shrink in length as they propagate.

3.3. Doppler Shift of the Line Core

Figure 9 shows the time-averaged result of the core Doppler shift measurements. The average values lie between about -5.7 km s^{-1} and 13.5 km s^{-1}, where the minus sign (and blue color) indicates motion toward the observer. The average Doppler velocity over the full field of view is 2.7 km s^{-1}, directed away from the observer.

There is a conspicuous asymmetry near the sunspot between blueshifted patches on the limb-ward side and redshifted ones on the disk-center side. These illustrate general inflow on the order of a few km s^{-1}, with slightly higher velocities of up to 10 km s^{-1} in the redshifted patches and up to -5 km s^{-1} in the blueshifted ones. The blueshifted limb-ward patches generally coincide well with the ends of the trajectories of the flocculent flows, as well as with the superpenumbral fibrils observed in Hα line center (cf. Figure 1). On the disk-center side such correlation

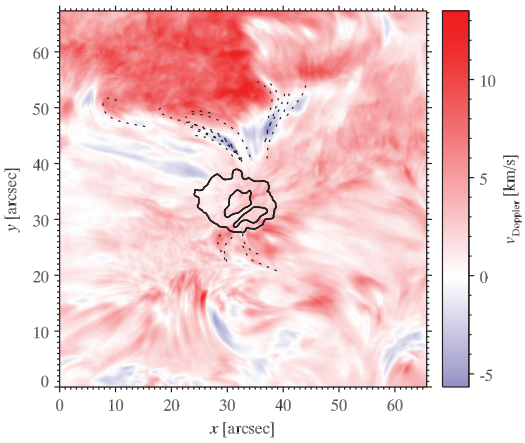

Figure 9. Time-averaged core Doppler shift map of the full field of view. Red: positive Doppler velocity (redshift). Blue: negative Doppler velocity (blueshift). Dotted: the same tracks as in Figure 1. Solid: contours for the umbra–penumbra boundary and the outer penumbra boundary at Hα − 1.1 Å.

is less strong. The temporal evolution of line core Doppler shift maps shows the blueshifted patches on the limb-ward side of the sunspot to be relatively stable, while the redshifted patches on the disk-center side are more variable, being replaced by blueshifts for several minutes at a time before returning to a redshift.

Space–time diagrams extracted from the Doppler map cube along the same flocculent flow trajectories show only occasionally enhancements that are co-spatial with the dark streaks observed in the space–time diagrams from the regular intensity data. In those cases for which corresponding enhancements are found, the related (absolute) line core Doppler shifts are typically on the order of 5–15 km s^{-1}. Also, the sign of the core Doppler shift correlates well with that of the flocculent feature Doppler velocity.

4. DISCUSSION

Our key finding is the presence of high-speed flows toward and away from the sunspot that are of intermittent, flocculent nature rather than continuous. They are observed in the Hα wings and appear to follow the fibrillar chromospheric structures seen in the Hα core. Their properties are summarized as follows.

1. We observe dark flocculent features with an average length of 627 ± 44 km and width of 304 ± 30 km propagating through the chromospheric canopy.
2. An average absolute velocity of 36.5 ± 5.9 km s^{-1} is found, but velocities in the range of 5–80 km s^{-1} are also measured. Features moving away from the sunspot propagate at a significantly lower average velocity of 30.3 km s^{-1}, against an average inflow at 38.8 km s^{-1}.
3. On average, flocculent features can be observed for 67.7 ± 8.8 s and typically 68 features are visible each minute. The actual lifetimes may be considerably larger, as the features typically (dis)appear in mid-flight or before reaching the photosphere as observed in the far wings.
4. Though practically co-spatial, the flocculent flows appear to be a phenomenon distinct from the "classical," lower-velocity inverse Evershed effect.

In this section we first discuss these flows with respect to the inverse Evershed effect (Section 4.1), coronal rain (Section 4.2), and then discuss the possible driving mechanism (Section 4.3).

4.1. Flocculent Flows and Inverse Evershed Effect

The general picture of the inflow in the chromospheric superpenumbra is confirmed by the results obtained in this study. Not only it is observed as an inflow at line-of-sight velocities of a few km s^{-1} (cf. Section 3.3), but also in the form of flocculent features moving at considerably higher velocities. Although we find slightly higher average values of up to 15 km s^{-1}, the line core Doppler shift velocities are similar to the inverse Evershed effect velocities obtained in earlier studies. St. John (1913) has already found inverse Evershed velocities on the order of about 3 km s^{-1} on average and similar velocities were obtained by Bones & Maltby (1978), who measured an average radial line-of-sight velocity of 1.8 km s^{-1} from Mg b$_1$ spectra. Dere et al. (1990) studied Hα ± 0.3 Å velocity maps and found velocities of 2.6 km s^{-1}, while Alissandrakis et al. (1988) obtained chromospheric line-of-sight velocities (averaged over the position angles considered) between +2 km s^{-1} (i.e., upflow) and −4 km s^{-1}, and Haugen (1969) found an average velocity vector peaking at the penumbral rim at 6.8 km s^{-1}. The velocities measured for the flocculent features are more on the order of the chromospheric inflow velocities as Maltby (1975) and Beckers (1962) found in their filtergram studies (velocities of 5–15 km s^{-1} and 40–50 km s^{-1}, respectively), but are also comparable to the velocities of some of the single absorbing elements measured in the spectroscopic study by Haugen (1969), who found velocities ranging between −35 and +50 km s^{-1} (where positive values indicated downflows).

We suggest nevertheless that most of the older studies, hampered by much lower spatial resolution than reached here and considering their morphological description of the inflows, concern the more gentle flow patterns that we observe as patches of enhanced line core Doppler shift seen in Figure 9. The flocculent features described here are in fact not observable at line center where they seem to be obscured by overlying fibrils (cf. Figure 2). The flow channels of the inverse Evershed effect and the flocculent flows appear to be distinct and are thus not the same flows.

4.2. Flocculent Flows and Coronal Rain

Morphologically, the flocculent flows are reminiscent of coronal rain. Recent work by Antolin & Rouppe van der Voort (2012) and in particular Antolin et al. (2012) shows this is not only the case qualitatively but also quantitatively. Both studies consider similar Hα imaging spectroscopy data obtained with CRISP as for this study. Antolin & Rouppe van der Voort (2012) suggest that the coronal rain phenomenon might be a common one, with single condensations attaining average absolute velocities on the order of 70 km s^{-1} and typical sizes of 0.74 Mm in length and 0.31 Mm in width. Similar dynamics and morphological quantities have been found by Antolin et al. (2012) for on-disk cases of coronal rain, including also in the currently considered data set. As these similarities may lead to difficulties in distinguishing both phenomena, as well as being indicative of a possibly related driving mechanism, we discuss this phenomenon in more depth.

Typical velocities for the coronal phenomenon are on the order of a few tens to a few hundred km s^{-1}, as for instance found by Schrijver (2001; studying quiescent coronal

loops) and O'Shea et al. (2007), who found Doppler shifts of 50–100 km s^{-1} and velocities of at least up to 100 km s^{-1} from He I and O IV data obtained with the Coronal Diagnostics Spectrometer on the *Solar and Heliospheric Observatory*. Müller et al. (2005) and De Groof et al. (2005) obtained velocities in a similar range (30–120 km s^{-1}) from observations, although the simulations of Müller et al. (2005) yielded typical velocities of about 50 km s^{-1}, while also indicating that subsequently downflowing blobs may travel at increasingly higher velocities of up to 230 km s^{-1} due to evacuation of the loop by preceding condensations.

The flocculent features observed in this study are somewhat smaller than those found by Antolin & Rouppe van der Voort (2012) and Antolin et al. (2012), however mostly so in length, and move at much lower average velocities than coronal rain. The lower velocities may result from the flocculent flow channels being much shorter than coronal loops, as the traced trajectories range between 3 and 14 Mm. Müller et al. (2003) reported on simulations of 10 Mm coronal loops, but found propagation velocities on the order of only a few km s^{-1} for the condensations that formed.

A further, important difference is that flocculent features appear to constitute a footpoint-to-footpoint, rather than apex-to-footpoint, flow. Even though no flocculent feature could be traced all the way from one footpoint to the other in this data set, the (re)appearance of the features close to the fibril apices moving at considerable velocities would argue against them forming through catastrophic cooling alone. In that respect, the higher flocculent flow velocities compared to the velocities from Müller et al. (2003) can be understood, as coronal rain accelerates from zero velocity as it starts precipitating.

Yet, even though the exact mechanism causing coronal rain may not be applicable to the flocculent flow phenomenon, a similar morphology may be nonetheless indicative of a thermal non-equilibrium process leading to the observed condensations. Comparison with the results obtained by Antolin & Rouppe van der Voort (2012) shows yet another striking similarity between both phenomena: in a majority of the flocculent flow cases adjacent fibrils display blobs propagating in the same direction at the same time, which may point at co-evolution of the conditions in neighboring fibrils.

4.3. Driving Mechanism

Distinguishing wave phenomena from actual mass flows is a recurring challenge, as what is observed as flocculent features may actually be gas compressed by propagating wave fronts, their velocities reflecting the phase speed of the waves, rather than actual mass motion. Indeed, similar features that have been observed before by Van Noort & Rouppe van der Voort (2006), who studied Hα line center data (i.e., no further spectral information), were explained as MHD waves. The qualitative morphology and behavior of the "moving features in loops" is practically identical to the flocculent flows described here and the differences with the projected velocities they report (40–120 km s^{-1}) may well be attributed to projection effects. With typical sizes of up to 275 km, the features they analyzed are notably smaller, however. Also, they report on bright blobs at line center, whereas the flocculent flows can only be seen in the wings of Hα, despite the viewing angles being comparable for both data sets. This may, however, be due to an inherent difference in fibril topology or by a different orientation of those fibrils to the line of sight. A more recent study by Lin et al. (2012), covering in part the same data sets, expands on the earlier results by Van Noort & Rouppe van der Voort (2006) by including CRISP data. They show that the bright blob-like features typically have small Doppler shifts ($\pm$5–10 km s^{-1}), last for up to about 150 s, and slightly increase in length as they propagate.

Features with similar morphology and behavior have also been found in other studies, albeit propagating at lower velocities. For instance, Sánchez-Andrade Nuño et al. (2008) found chromospheric magnetoacoustic waves in Hα observations. These waves manifest themselves mainly as (trains of) blobs with average dimensions as small as 725 km (1 arcsec) in length and 360 km (0.5 arcsec) in width, propagating at phase velocities between 12 and 42 km s^{-1}. Both the sizes and the phenomenology are similar to what we observe for the flocculent flows. However, in contrast to those (but in common with some of the features described by Van Noort & Rouppe van der Voort 2006), the blobs observed by Sánchez-Andrade Nuño et al. show displacement perpendicular to their propagation direction. In a more recent study of Ca II 8542 Å data obtained with SST/CRISP, Wedemeyer-Böhm (2010) reported on (among other things) bright blobs propagating at projected velocities of 4–8 km s^{-1} along neighboring fibrils that he explained as a wave manifestation.

Considering this scenario further, we note that typical chromospheric sound speeds are on the order of 10–15 km s^{-1} (e.g., Alissandrakis et al. 1988; Tsiropoula 2000; Sánchez-Andrade Nuño et al. 2008; Lin et al. 2012), while Alfvén speeds may range between 175 and 600 km s^{-1} for magnetic field strengths between 30 and 100 G (cf. Sánchez-Andrade Nuño et al. 2008, and references therein) and a reasonable chromospheric density of 2×10^{-13} g cm^{-3} (cf. Tsiropoula 2000 and references therein). Although subsonic flocculent features have been found, most exceed the chromospheric sound speed by far and hence the flocculent flows cannot be attributed exclusively to acoustic waves. A magnetoacoustic wave scenario may allow for much higher velocities (even comparable to flocculent flow velocities), as for instance shown by Giovanelli (1975), who measured phase velocities on the order of 70 km s^{-1} in Hα observations of quiet chromosphere and a sunspot. Assuming typical chromospheric number densities and a magnetic field strength of 10 G, these velocities could be reconciled with an Alfvén wave scenario. However, one thus needs to assume rather low field strengths (i.e., below 6 G) in order to obtain an Alfvén velocity as low as the average flocculent flow velocity of 36 km s^{-1}. In addition, the high Doppler velocities of the flocculent features in combination with the changes in the Doppler component velocities as the features propagate along their curved paths would seem to argue for actual mass motion rather than waves.

An alternative driving mechanism could be found in the siphon flow model. Siphon flows have been suggested before in the context of the inverse Evershed effect (cf. Haugen 1969; Maltby 1975; Alissandrakis et al. 1988; Dere et al. 1990; Boerner & Kneer 1992; Kjeldseth-Moe et al. 1993; Montesinos & Thomas 1997). In this model, a flow is driven by a gas pressure inequality between the footpoints of a magnetic flux tube, which in turn is caused by a difference in magnetic field concentration (and hence strength) at the respective footpoints. A higher magnetic field strength at one footpoint will result in lower gas pressure at that same footpoint and vice versa. As the magnetic field strength of a sunspot will be larger than in the surrounding plage, a flow directed toward the sunspot would naturally occur in this model. Analytical solutions predict both sub- and supersonic flows, depending on the parameters

of the loop structure; however, supersonic flows in the critical solution (i.e., where the flow has been accelerated from sub- to supersonic) will always return to a subsonic state through the formation of a shock (cf. Cargill & Priest 1980; Thomas 1988). Since the flocculent flows appear to be footpoint-to-footpoint flows, the siphon flow model may offer a viable way to explain them. For most cases a supersonic flow would be required, at the very least for that part of the fibrils where the flocculent features are visible.

A number of problems arise, however. The siphon flow model may explain the general characteristic of an inward flow toward the sunspot, but it does not explain why flocculent features could be formed. Although shocks will occur in the transition from supersonic to subsonic flows and have been observed to a larger or smaller degree of confidence (cf. Degenhardt et al. 1993; Uitenbroek et al. 2006; Bethge et al. 2012), there is no evidence that these shocks cause propagating condensations and would rather show up as brightenings due to material compression and the consequent rise in temperature. A few cases of decelerating flocculent features were found in this study, but the return to subcritical velocities through a shock was not evident from the data. However, as Bethge et al. (2012) already pointed out for their case, these shocks could be occurring at lower altitudes that are not sampled by the Hα line. Alternatively, the shocks could be obscured from view by overlying fibrils, in a similar way to flocculent features closer to Hα line center. Also, we observe flows toward the plage, i.e., in the direction opposite to what the siphon flow model predicts. Although in most cases these features are seen close to the plage (footpoints) only and could thus be propagating in fibrils that are actually not connected to the sunspot (allowing possibly low enough field strength for oppositely directed flows), this does not hold true for all cases. Nonetheless, as suggested by Cargill & Priest (1980), an oppositely directed flow may occur in a fibril with an established siphon flow as a result of a change in pressure difference. Evidence for the existence of such a counterflow has for instance been provided by Guglielmino & Zuccarello (2011) in a recent study of a pore and its surroundings.

Although considering much larger scales, recent simulations described by Zacharias et al. (2011) may also offer a possible driving mechanism. The simulations they present show the emergence of a blob-like feature from the transition region, resulting from the buildup of pressure (in turn caused by a heating event at one footpoint) propelling the feature further through the corona along a magnetic loop structure before falling down again. The feature described has much larger dimensions than typical flocculent features or coronal rain and only occurred once during a 1 hr simulation run. A similar heating mechanism might nevertheless work on smaller scales too, producing blobs of smaller sizes propagating through the chromosphere and/or transition region at possibly shorter time intervals.

5. CONCLUDING REMARKS

In this paper, we have analyzed flocculent flows occurring along the chromospheric canopy as observed at high spatial, temporal, and spectral resolution in Hα data obtained with the CRISP instrument at the Swedish 1-m Solar Telescope. Although we have been able to obtain statistical properties of a considerable sample of flocculent features, we can at this point merely speculate about the mechanism driving the flocculent flows. The results obtained, both qualitatively and quantitatively, seem to argue against a purely wave-related phenomenon. Rather, the flocculent features are more likely to occur as part of an already present (supersonic) siphon flow, which could develop its flocculence as a result of, for instance, recurring heating events leading to the formation of condensations (in analogy to the larger scale phenomenon described by Zacharias et al. 2011), or waves interacting with the flow-carrying fibrils, causing the condensations to form as the fibril is pushed out of thermal equilibrium. In either case, these condensations would subsequently be carried by the siphon flow at supersonic velocities (where they are observed) before being decelerating through a shock to subsonic velocities upon reaching the photosphere.

Given that this phenomenon appears to be ubiquitous and not solely related to the superpenumbra, a study of multiple data sets (including also more quiet regions) and with different diagnostics would not be out of place. In addition, where observations may constrain the properties of the flocculent features as well as the necessary environmental conditions for them to occur, simulations would be very helpful in further uncovering their driving mechanism.

The authors thank Patrick Antolin for many useful discussions and are indebted to Rob Rutten for numerous helpful suggestions regarding the manuscript. G.V. in addition thanks Luc Rouppe van der Voort, Patrick Antolin, Bart de Pontieu, Sven Wedemeyer-Böhm, Mats Carlsson, Jorrit Leenaarts, Eamon Scullion, and Jaime de la Cruz Rodriguez for their invaluable input to improve and extend CRISPEX. G.V. has been supported by a Marie Curie Early Stage Research Training Fellowship of the European Community's 6th Framework Programme (MEST-CT-2005-020395): The USO-SP International School for Solar Physics. The Swedish 1-m Solar Telescope is operated on the island of La Palma by the Institute for Solar Physics of the Royal Swedish Academy of Sciences in the Spanish Observatorio del Roque de los Muchachos of the Instituto de Astrofísica de Canarias.

APPENDIX

ANALYSIS TOOLS: INTRODUCING CRISPEX AND TANAT

Sophisticated instruments such as the CRISP instrument at the SST deliver large data sets that are often formatted as multidimensional data cubes. These are nontrivial to browse and analyze, and require therefore a tool with which one may quickly explore the data obtained for interesting features and which, preferably at the same time, allows for more in-depth analysis of the data set of interest. A widget based tool, programmed in the Interactive Data Language (IDL), was developed with that goal in mind and driven by the particular challenges faced as a result of the extensive observational possibilities offered by CRISP. The CRisp SPectral EXplorer (CRISPEX)[2] can currently handle the following.

1. single spectral scans;
2. simple three-dimensional temporal cubes (i.e., a time series of intensity images);
3. spectrotemporal cubes (i.e., cubes with both spectral and temporal information); and
4. Stokes data cubes (i.e., spectrotemporal cubes including also multiple Stokes parameters).

[2] Both the actual distribution and more detailed descriptions of the functionality and options of CRISPEX and its auxiliary routines can be found at http://folk.uio.no/gregal/crispex.

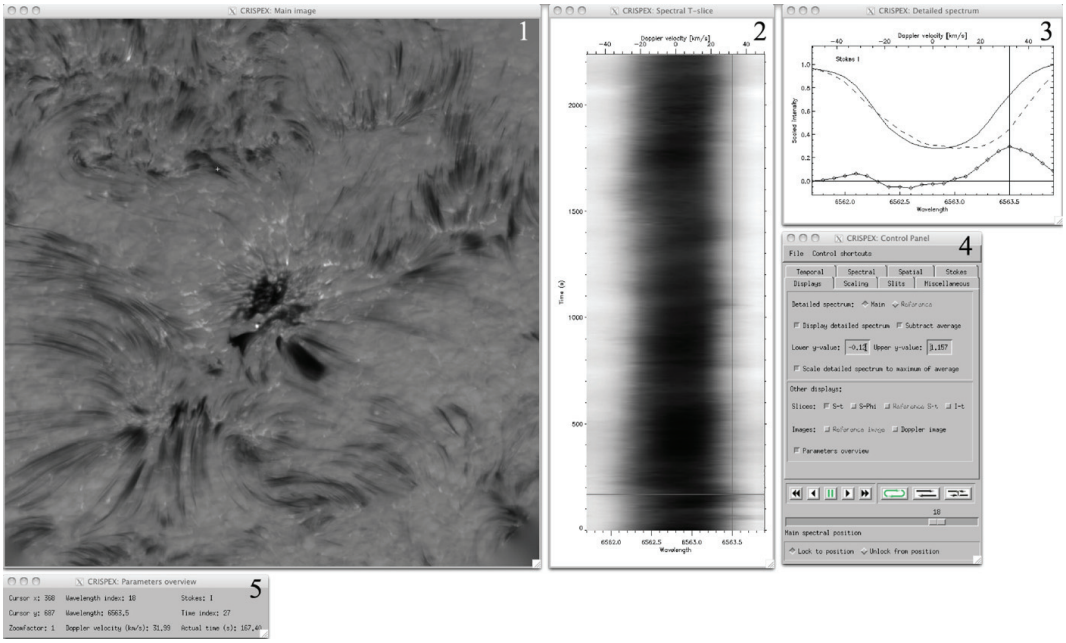

Figure 10. Default layout of windows loaded by CRISPEX, showing clockwise from the top left: (1) the intensity image, (2) the spectrum–time diagram, (3) the local spectrum, (4) the control panel, and (5) the parameters overview window.

As the typical size of CRISP data cubes exceeds the available random access memory on regular laptop or desktop computers, the data are read in to an associated variable and hence CRISPEX need neither read nor keep a full data cube in memory, thereby enabling quick browsing in the spatial, temporal, and spectral domain. This swiftness comes at a cost, however. In order to have full spectral browsing functionality, a spectral data cube (which is nothing more than a reordered image data cube) must be supplied as well, thus requiring double the amount of disk space for one data set.

Though originally designed and intended to handle CRISP data, CRISPEX can cope with any (observational or synthetic) data, provided it has been formatted in a certain way. Indeed, the tool has already been successfully used in several studies based on CRISP data (Rouppe van der Voort et al. 2009; Wedemeyer-Böhm & Rouppe van der Voort 2009; Antolin et al. 2010; Watanabe et al. 2011; Lin et al. 2012), as well as *Hinode*/SOT data (Antolin & Verwichte 2011).

A.1. Visualization and Analysis Options

Depending on the input data, different visualization and browsing options are available to the user. One can simultaneously:

1. play forward and backward in time;
2. step through a spectral profile;
3. switch between Stokes parameters;
4. blink between image frames, stepping both in temporal and spectral dimension.

Data feedback is given to the user through multiple screens of which Figure 10 shows an example. Following CRISP's capability to run multiple line programs (i.e., observing programs where time series in more than one spectral line are obtained), CRISPEX can display two data sets at a time. Such reference data (e.g., a reference magnetogram) need not have the same spectral dimension, but are currently only constrained to having the same spatial dimensions and either consist of a single frame or the same amount of temporal frames as the main data cube. Additionally, CRISPEX allows for simple image and spectrum saving (with the option to include or exclude overlays, such as the cursor or drawn paths), which can be used for simple movie production.

CRISPEX also offers a number of analysis options, but one of its first and most developed features is the extraction of space–time diagrams along user-defined (curved) paths. These paths can (as they are in this study), but need not necessarily, be manually defined. One may also supply a file with detections to extract space–time diagrams along, as was done by Rouppe van der Voort et al. (2009) in their spectral analysis of on-disk counterparts of type II spicules. Space–time diagrams can be extracted and saved for a single wavelength position or for a given spectral range (which may be the entire spectral scan) as well as for a restricted temporal range. Another analysis option is given by the spectral slit functionality, which extracts the spectrum for each pixel along a line centered on the cursor. The slit can be adjusted both in length and in rotation angle, thereby allowing the coverage of practically any feature of interest. In particular, for those cases where a profile scan is available, the in-program Doppler image functionality may be of use to browse the Doppler image constructed from the subtraction of the red from the blue wing. Though this feature may slow down the overall playback, depending on the memory available on the machine used, one escapes the need to produce a separate Doppler cube. Lastly, the functionality to display intensity–time

diagrams may be particularly useful when cubes do not consist of profile scans but rather of different spectral diagnostics. This functionality could be used to show, for example, subsequent detection of a phenomenon in different diagnostics of multiple *SDO*/AIA channels.

A.2. Auxiliary Programs

Although the CRISPEX distribution comes with several auxiliary routines, one program in particular deserves some further introduction, since it offers important analysis options complementary to those in CRISPEX. The Timeslice ANAlysis Tool (TANAT) facilitates the analysis of space–time diagrams extracted with CRISPEX, as it enables the determination of projected velocities and accelerations of features from these diagrams. Such measurements can subsequently be saved to a file, with the option to add a (custom) flag for each measurement as it is saved, and adding by default a unique identifying number which enables the correct overlay of saved measurements on the corresponding space–time diagram. In addition, different visualization options allow switching between or combination of space–time diagrams for different positions within the spectral line observed, thereby enabling—for instance—the comparison of a feature's signal (or lack thereof) in the red and blue wings of a spectral line.

REFERENCES

Alissandrakis, C. E., Dialetis, D., Mein, P., Schmieder, B., & Simon, G. 1988, A&A, 201, 339
Antolin, P., & Rouppe van der Voort, L. 2012, ApJ, 745, 152
Antolin, P., Shibata, K., & Vissers, G. 2010, ApJ, 716, 154
Antolin, P., & Verwichte, E. 2011, ApJ, 736, 121
Antolin, P., Vissers, G., & Rouppe van der Voort, L. 2012, Sol. Phys., in press (arXiv:1203.2077)
Beckers, J. M. 1962, Aust. J. Phys., 15, 327
Bethge, C., Beck, C., Peter, H., & Lagg, A. 2012, A&A, 537, A130
Boerner, P., & Kneer, F. 1992, A&A, 259, 307
Bones, J., & Maltby, P. 1978, Sol. Phys., 57, 65
Bray, R. J., & Loughhead, R. E. (ed.) 1974, The Solar Chromosphere (London: Chapman and Hall)
Cargill, P. J., & Priest, E. R. 1980, Sol. Phys., 65, 251
Degenhardt, D., Solanki, S. K., Montesinos, B., & Thomas, J. H. 1993, A&A, 279, L29
De Groof, A., Bastiaensen, C., Müller, D. A. N., Berghmans, D., & Poedts, S. 2005, A&A, 443, 319
Dere, K. P., Schmieder, B., & Alissandrakis, C. E. 1990, A&A, 233, 207
Doyle, J. G., Taroyan, Y., Ishak, B., Madjarska, M. S., & Bradshaw, S. J. 2006, A&A, 452, 1075
Evershed, J. 1909a, MNRAS, 69, 454
Evershed, J. 1909b, Observatory, 32, 291
Giovanelli, R. 1975, Sol. Phys., 44, 299
Guglielmino, S. L., & Zuccarello, F. 2011, ApJ, 743, L9
Haugen, E. 1969, Sol. Phys., 9, 88
Heinemann, T., Nordlund, Å., Scharmer, G. B., & Spruit, H. C. 2007, ApJ, 669, 1390
Kjeldseth-Moe, O., & Brekke, P. 1998, Sol. Phys., 182, 73
Kjeldseth-Moe, O., Brynildsen, N., Brekke, P., Maltby, P., & Brueckner, G. E. 1993, Sol. Phys., 145, 257
Lin, Y., Engvold, O., & Rouppe van der Voort, L. 2012, ApJ, 747, 129
Maltby, P. 1975, Sol. Phys., 43, 91
Montesinos, B., & Thomas, J. H. 1997, Nature, 390, 485
Müller, D. A. N., De Groof, A., Hansteen, V. H., & Peter, H. 2005, A&A, 436, 1067
Müller, D. A. N., Hansteen, V. H., & Peter, H. 2003, A&A, 411, 605
Nordlund, Å., & Scharmer, G. B. 2010, in Magnetic Coupling between the Interior and Atmosphere of the Sun, ed. S. S. Hasan & R. J. Rutten (Berlin: Springer), 243
O'Shea, E., Banerjee, D., & Doyle, J. G. 2007, A&A, 475, L25
Rempel, M., Schüssler, M., & Knölker, M. 2009, ApJ, 691, 640
Rouppe van der Voort, L., Leenaarts, J., de Pontieu, B., Carlsson, M., & Vissers, G. 2009, ApJ, 705, 272
Sánchez-Andrade Nuño, B., Bello González, N., Blanco Rodríguez, J., Kneer, F., & Puschmann, K. G. 2008, A&A, 486, 577
Scharmer, G. B., Bjelksjo, K., Korhonen, T. K., Lindberg, B., & Petterson, B. 2003a, Proc. SPIE, 4853, 341
Scharmer, G. B., Dettori, P. M., Lofdahl, M. G., & Shand, M. 2003b, Proc. SPIE, 4853, 370
Scharmer, G. B., Henriques, V. M. J., Kiselman, D., & de la Cruz Rodríguez, J. 2011, Science, 333, 316
Scharmer, G. B., Narayan, G., Hillberg, T., et al. 2008, ApJ, 689, L69
Schrijver, C. J. 2001, Sol. Phys., 198, 325
Shine, R. A., Title, A. M., Tarbell, T. D., et al. 1994, ApJ, 430, 413
Spruit, H. C., & Scharmer, G. B. 2006, A&A, 447, 343
St. John, C. E. 1913, ApJ, 37, 322
Teriaca, L., Curdt, W., & Solanki, S. K. 2008, A&A, 491, L5
Thomas, J. H. 1988, ApJ, 333, 407
Tian, H., Marsch, E., Curdt, W., & He, J. 2009, ApJ, 704, 883
Tsiropoula, G. 2000, A&A, 357, 735
Uitenbroek, H., Balasubramaniam, K. S., & Tritschler, A. 2006, ApJ, 645, 776
Van Noort, M., Rouppe van der Voort, L., & Löfdahl, M. G. 2005, Sol. Phys., 228, 191
Van Noort, M. J., & Rouppe van der Voort, L. H. M. 2006, ApJ, 648, L67
Van Noort, M. J., & Rouppe van der Voort, L. H. M. 2008, A&A, 489, 429
Watanabe, H., Vissers, G., Kitai, R., Rouppe van der Voort, L., & Rutten, R. J. 2011, ApJ, 736, 71
Wedemeyer-Böhm, S. 2010, Mem. Soc. Astron. Ital., 81, 693
Wedemeyer-Böhm, S., & Rouppe van der Voort, L. 2009, A&A, 507, L9
Zacharias, P., Peter, H., & Bingert, S. 2011, A&A, 532, A112

IV

On-disc coronal rain
P. Antolin, G. Vissers and L. Rouppe van der Voort
Solar Physics, Volume 280, pp. 457–474 (2012)